Medical Image Processing Lab
Ecole Polytechnique Fédérale de Lausanne

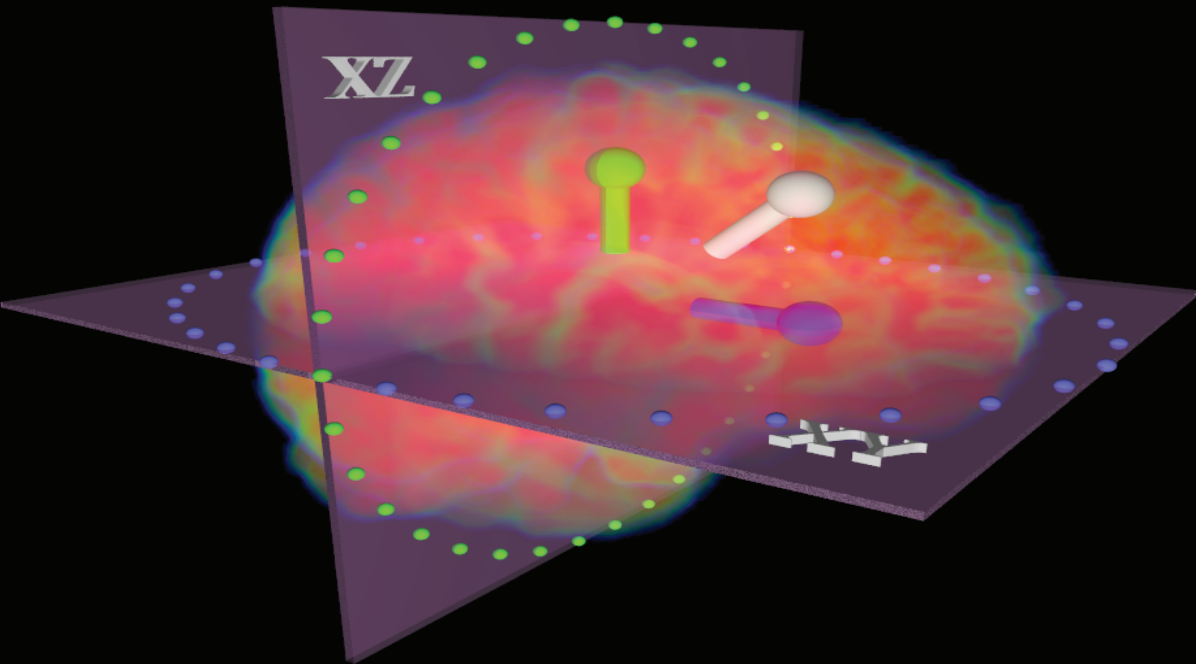

Analytic Sensing: Sparse Source Recovery from Boundary Measurements using an Extension of Prony's Method for the Poisson Equation

Djano Kandaswamy

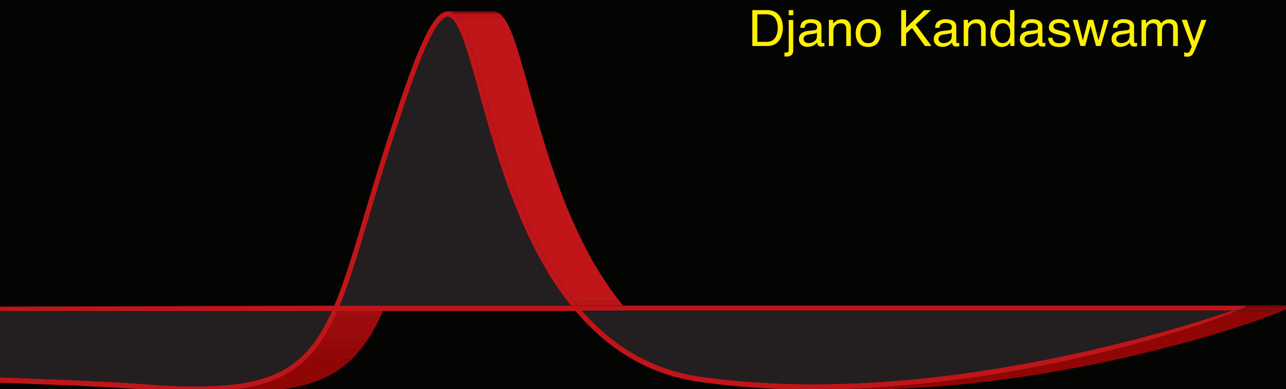

Sparse source recovery from boundary measurements using an extension of Prony's method for the Poisson equation

Djano Kandaswamy

Thèse N° 5085 (May 2011)

Thèse présentée à la faculté des sciences et techniques de l'ingénieur
pour l'obtention du grade de docteur ès sciences
et acceptée sur proposition du jury

Prof. Roger Hersch, *président*
Prof. Dimitri Van De Ville, *directeur de thèse*
Prof. Thierry Blu, *co-directeur*
Dr. Maureen Clerc, *rapporteur*
Prof. Christoph Michel, *rapporteur*
Prof. Martin Vetterli, *rapporteur*

École polytechnique fédérale de Lausanne—2011

Cover design by <To be done>
Printing and binding by Repro-EPFL
Typeset with LaTeX

Available at **http://miplab.epfl.ch/**

Abstract

Electroencephalography (EEG) is a key modality to monitor brain activity with high temporal resolution. EEG makes use of an array of electrodes to measure the electrical potential on the scalp. While most traditional EEG analyses have looked at EEG rhythms in different frequency bands, another important application of EEG is source imaging; i.e., map back the measured scalp potential to the underlying source distribution. However, source localization is an ill-posed problem. Most approaches consider a grid of neurobiologically relevant dipoles with fixed positions and directions of their moments, which makes for many more unknown intensities than the number of measures. To make the solution unique, one needs to add regularization strategies such as smoothness or sparsity. The alternative, which is the approach that we will follow in this work, is to impose a sparse and parametric source model with few unknown parameters, but which include both dipole positions and moments thus rendering the problem solution highly non-linear.

The proposed method, for which we coin the term "analytic sensing", is based on two main working principles. First, based on the divergence theorem, the sensing principle relates the boundary potential to a volumetric information about the sources. This principle makes use of a mathematical test function ("analytic sensor") that needs to be a homogeneous solution of the Poisson equation, which is the governing equation of the quasi-static electromagnetic setting. The analytic sensor can be defined for different geometries and conductivity profiles of the domain of interest. We derive closed-form expressions for 3D multi-layer spherical models that are often used as a head model in EEG.

Recent advances in signal processing known as "annihilation filter" or "finite rate of innovation", have extended Prony's method to recover sparse sources in a robust way, typically a stream of Diracs. We propose to apply the annihilation principle by imposing a particular choice of multiple analytic sensors; i.e., the virtual measurements obtained with these functions can be annihilated by a filter that allows us to recover the dipoles' positions in a non-iterative way. The dipoles' moments can subsequently be retrieved by solving a linear system of equations.

While the application of the sensing principle is intrinsically 2D or 3D, the annihilation principle gives only access to the orthographic projection of the source distribution. Two approaches have been developed. First, using coordinate transformations, one can obtain multiple projections of the sources and recombine them to reconstruct the full 3D information. Second, using a second set of analytic sensors, it is possible to retrieve the missing coordinate by solving another linear system of equations.

Successful application of the method requires careful implementation of both principles. For the sensing principle, we project the boundary measurements on a set of spherical harmonics with proper regularization to cover parts of the boundary that are not measured. We also show how the annihilation step can be implemented to be robust to noise and numerically stable. We demonstrate the precision and robustness of the method by both experimental results and theoretical Cramèr-Rao bounds. Finally, we show effective source localization for real-world experimental EEG data; i.e., we identify the underlying sources for several time instants of a visual evoked potential.

Keywords: inverse problems, EEG source imaging, Poisson equation, non-iterative reconstruction, analytic functions, spherical head model

Résumé

L'électroencéphalographie (EEG) est une méthode essentielle pour surveiller l'activité cérébrale avec une haute résolution temporelle. L'EEG mesure les potentiels électriques au niveau du cuir chevelu à l'aide d'un réseau d'électrodes. Alors que les méthodes classiques classifient le signal EEG à partir de l'analyse des bandes de fréquence en présence, une autre application de l'EEG concerne la localisation de source ; à savoir, retrouver la distribution de sources qui sont à l'origine des potentiels mesurés à la surface du crne. Toutefois, la localisation de sources est un problème notoirement mal conditionné. La plupart des approches considèrent une grille de dipôles pertinents du point de vue neuro-biologique avec une position et une orientation fixées, ce qui conduit à un problème ayant bien plus d'inconnues que de mesures. Pour déterminer une solution unique, il est nécessaire de recourir à des stratégies de régularisation, insistant sur la parcimonie ou l'aspect lisse de la solution. Une alternative à la régularisation, faisant l'objet de ce travail, est d'imposer un modèle de source parcimonieux et paramétrique caractérisé par peu d'inconnues, mais qui inclut à la fois les positions et les orientations des dipôles, rendant la solution du problème fortement non-linéaire.

La méthode proposée, que nous avons intitulée "analytic sensing", repose sur deux fondements. Premièrement, en se basant sur le théorème de Green-Ostrogradski, le potentiel de surface est lié à une distribution volumique des sources. Cette méthode fait appel à une fonction test ("un détecteur analytique") qui doit être une solution homogène à l'équation de Poisson régissant les champs électromagnétiques quasi-stationnaires. Le détecteur analytique peut être défini pour diverses géométrie et distributions de conductivité. Nous dérivons des expressions analytiques pour les modèles 3D multi-couches qui sont souvent utilisés en EEG. Deuxièmement, de récentes découvertes en traitement du signal, "annihilation filter" ou "finite rate of innovation", ont permis d'étendre la méthode de Prony pour retrouver, de manière robuste, des sources parcimonieuses, typiquement modélisées comme des impulsions spatiales. Nous proposons d'appliquer le principe d'annihilation en imposant un choix particulier de plusieurs détecteurs analytiques. Les mesures obtenues avec ces fonctions peuvent être annihilées par un filtre qui permet de retrouver la position des dipôles de faqn non itérative. Les orientations des dipôles peuvent ensuite être obtenues en résolvant un système d'équations linéaires. Pour la localisation volumique, le principe d'annihilation ne donne accès qu'à deux des coordonnées de la distribution des sources. Pour localiser les sources dans la troisième dimension, deux approches ont été proposées. Par l'intermédiaire de changements de coordonnées, différentes projections des sources permettent, une fois recombinées, de reconstruire l'information tridimensionnelle complète. Alternativement, en utilisant un deuxième jeu de détecteurs analytiques, la coordonnée manquante peut être définie comme la solution d'un nouveau système d'équations linéaires.

L'application de la méthode, pour être fructueuse, nécessite une implémentation soignée des deux principes. Pour la représentation continue du potentiel électrique, nous avons projeté les mesures de surface sur un ensemble d'harmoniques sphériques, utilisant une régularisation afin d'extrapoler acceptablement les zones non mesurées. Nous avons également montré comment l'étape d'annihilation peut être implémentée de manière à être robuste au bruit et numériquement stable. Nous démontrons la robustesse et la précision de la méthode tant par des résultats expérimentaux et par le calcul théorique des bornes de Cramér-Rao. Enfin, nous démontrons une localisation effective de sources avec des données EEG réelles, coïncidant avec une méthode de référence.

Mots-clés : problème inverse, image de source EEG, équation de Poisson, reconstruction non itérative, fonctions analytiques, modèle de tête sphérique

To my family

Acknowledgement

During my stay at the Medical Image Processing Lab (MIPLab), I encountered several people without whom this manuscript would not have been possible. I hereby explicitly thank

- **Dimitri Van De Ville**
  Without Dimitri, MIPLab's director and my thesis supervisor, this project could never have been completed. He flawlessly navigated through the administrative pitfalls to obtain any funding needed. Moreover, I would like to thank him for his support, specifically, sharing his scientific knowhow, proof-reading papers and obtaining real EEG data.

- **Thierry Blu**
  Thierry, now a professor at the Chinese University of Hong Kong (CUHK) and my thesis co-supervisor, shared part of his tremendous mathematical knowledge which allowed for an in-depth understanding of the inverse EEG problem. He showed me that mathematics for the sake of mathematics is useless, but rather mathematics should be used to find elegant solutions to real-life problems. Throughout this thesis I could benefit from his ideas to elegantly solve many of the encountered problems. I also want to thank him and his wife, Sybil Chan, for the hospitality during the three months spent in Hong Kong ("Tai Po Market rules!").

- **Juliane Britz**
  Juliane, a member of the Functional Brain Mapping Lab, supplied us with high-quality EEG data on which I tested our reconstruction method. She helped me with the application to real data. We had many fruitful discussions

(read skype sessions) which allowed me to analyze the real data with analytic sensing.

- **Denis Brunet** and **Laurent Spinelli**
  Denis, a member of the Functional Brain Mapping Lab and creator of Cartool, explained to us how to use the SMAC head model and how to import the files used by Cartool in MatLab. Moreover, he gave us the MRI volume corresponding to the SMAC model. All of this made the visualizations in chapter 7 possible. Also we thank Laurent for his kind assistance with my questions on the SMAC head model.

Also in research, you need funding to get the job done. In the early days, the project "analytic sensing" kicked off mainly based on enthusiasm. Various people, associated to various labs, helped to bridge the financial gap. In particular we thank **Michael Unser**, head of the Biomedical Imaging Group (BIG) at EPFL and **François Lazeyras** affiliated to the CIBM at the HuGe. We obtained a grant from the **Swiss National Science Foundation** (**SNSF**), which allowed us to pursue our research to its completion. We would like to thank the SNSF for its financial support. **Thierry Blu** has been implicated in the project from the very beginning, and we thought it useful to keep this collaboration after his move to Hong Kong. This was made possible thanks to grants by the **Sino-Swiss** and the **CUHK Microsoft** which financed our stays in Hong Kong.

I am also very grateful to the members of my thesis jury, **Dr. Maureen Clerc**, **Prof. Christoph Michel** and **Prof. Martin Vetterli**, for having accepted to read and comment the present work.

Last but not least, I would like to thank my family (my father, **Kala**, my mother, **Flippy** and my brother **Aroen**), my girlfriend (**Sylvie**) for putting up with me during these last two months and all those who make my stay in Switzerland enjoyable.

Contents

Chapter 1

Problem Setting

1.1 Introduction

1.2 Background

Wolfgang Gullich, famous for his one arm one finger pull-up and a legend among rock climbers, stated “The brain is the most important muscle for climbing”. In saying that, Wolfgang made one mistake, the brain isn’t a muscle but an organ, the most important organ in the central nervous system of the human body for it enables reasoning, perception, movement, sight, all crucial for complex tasks such as climbing.

The brain consists of roughly ten billion interacting nerve cells, called neurons, structured in what is known as the brain’s anatomy. These neurons are organized in different regions that can be designated according to their function. For example, a specific region in the brain is responsible for motor function, while other regions are involved in high-level cognitive processing. Next to specialized regions there is also aggregation which requires communication of information between brain regions.

The brain is nested in the skull and scalp, which act as protective layers. Moreover, it floats in the ventricular system which is drained with the cerebrospinal fluid (CSF). The CSF, together with blood, provides essential substances for the metabolism of the brain. Concerning tissue types, the actual brain tissues can be

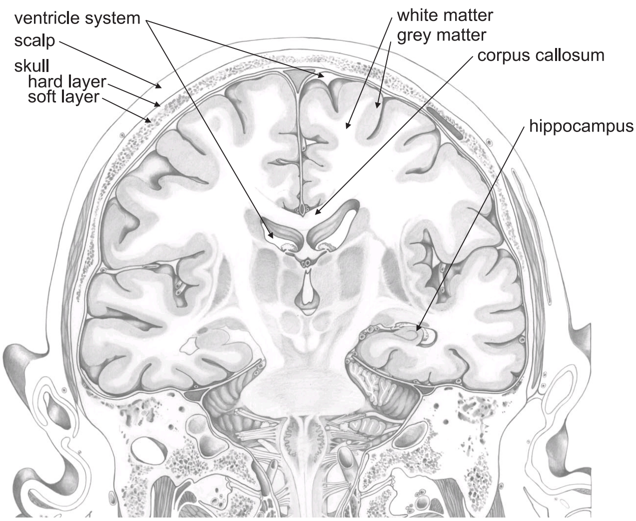

Figure 1.1: A coronal slice of the human head with some important structures indicated (this figure has been adopted from [1]).

divided in three parts: white matter, gray matter and the ventricles (see figure 1.1).

The white matter mainly consists of connections from and to different parts of the gray matter. For example, an important connection contained in the white matter is the *corpus callosum* which connects the right and left hemisphere (see figure 1.1). The actual brain activity is generated in the gray matter. The gray matter at the edge of the brain has a folded structure. The outer layer is also called the cortex or cortical gray matter. In the gray matter many structures can be identified according to their function in the processing of information. An example of such a structure is the hippocampus, which is related to the short term memory. The hippocampus has very complicated folded structure. Specific types of epilepsy are related to this structure. The nerve cells in the gray matter are generators of the electrochemical activity of the brain.

Neurons or nerve cells are the building blocks of the human central nervous system. The brain consists of about 10^{10} of such neurons. The neuron's task is to process signals coming from other neurons and transmit signals to other neurons (or tissue such as muscles or organs). The shape and size of the neurons vary but all neurons possess the same anatomical subdivision. Neurons consist of 3 parts, the dendrites, the cell body or soma and the axon as depicted in figure 1.2 The

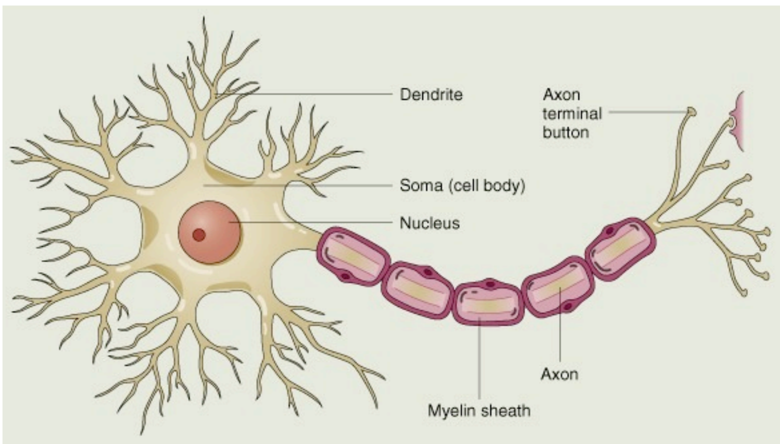

Figure 1.2: A nerve cell, also called a neuron, and its anatomical structure. This picture has been taken from http://www.indiatalkies.com/2011/02/nerve-cell-grow-cells-contact.html.

dendrites, which includes all the branches, are specialized in receiving inputs from other nerve cells. The soma or cell body contains the nucleus of the neuron. It processes the incoming electrical signals and decides if a signal has to be transmitted to the axon. In that case the neuron generates a potential, called an action potential, which propagates through the axon. Via the axon, impulses are sent to other neurons. These potentials received by the surrounding neurons are called postsynaptic potentials. For a more in depth overview on the anatomy and physiology of the neuron we refer to [2, 3, 4].

The amplitude of such an action potential is rather large (70-110mV) but it has a small time course (0.3ms). Moreover, a synchronous firing of action potentials is very unlikely, which makes these action potentials unmeasurable by the EEG. The postsynaptic potentials on the other hand have a rather small amplitude (0.1-10mV), but a larger time course, 10-20ms. The postsynaptic potentials are the generators of the extracellular potential field. Since their time course is larger they allow for the measurements of summed activity of neighbouring neurons [1, 5]. In such, we need a more or less regular arrangement of neurons that are more or less synchronously active. The spatial properties of the neurons must be such that they amplify each others' extracellular potential fields.

Pyramidal neuron cells are a special type of neurons which consist of a large dendrite branch that is oriented orthogonally to the surface of the gray matter. Neighboring pyramidal cells are organized so that the axes of their dendrite trees are parallel and normal to the cortical surface. The spatial configuration is such that if they fire synchronously, then they amplify each others' extracellular potential fields. The synchronous electrical activity of such neighboring pyramidal cells generates an electrical signal that is measurable with the electroencephalogram (EEG).

The electroencephalogram is the measure of the electrical activity generated by the brain on the scalp. The human EEG recording was done by Hans Berger, a German neurologist, back in 1924. Berger discovered that the measured EEG in wake and sleeping state differ. More precisely, using the EEG he discovered the alpha wave also known as Berger's wave. This wave is an electric waveform (with characteristic frequency 8-12Hz) which originates from the occipital lobe during wakeful relaxation with closed eyes [6]. Nowadays, the EEG is mainly used to measure such brainwaves; e.g., beta (>14Hz) and delta rhythms(<4Hz). While the analysis of such rhythms will probably never tell us what a person is thinking, it can help us know if a person is thinking [7].

Another application of the EEG is to determine the sources responsible for the measured EEG. This is an ill-posed problem in the sense of unicity [8]. However, in some cases the measured EEG stems from a well-localized electrically active zone, e.g., partial epileptic seizures stem from such focal zones also called the epileptic onset zones. Evoked potentials (EPs) are the potential differences generated on the scalp that are triggered by a physical stimulus. These stimuli can be of visual, auditory or somatosensory nature. The characteristic waveform of such an EP is often generated by well-localized zones in the cortex. Such focal zones are adequately modeled by dipoles. If we use this a priori information; i.e., the generating source distribution is a superposition of dipoles, then the solution of the inverse EEG problem is unique [9]. In such cases it is useful to determine the generating source distribution. Reconstructing the sources responsible for the measured scalp potential is commonly called source localization or source analysis.

1.3 Formal Problem Description

The quasi-static approximation of Maxwell's equations combined with the conservation law $\nabla \cdot \mathbf{J} = 0$, with $\mathbf{J}$ the current density, relate a source distribution, ρ, to the generated potential, V, if all fields and currents behave as if they were stationary at each instance in time. Moreover, it shown in [10] that these quasi-static conditions hold in EEG. Consequently the governing equation that relates the source distribution to the measured EEG in the conductor model, Ω, is:

$$-\operatorname{div}(\sigma \nabla V) = \rho, \quad \text{within } \Omega, \tag{1.1}$$

where σ is the conductivity profile of Ω and Ω is the conductor model that represents the head (often called head model). In the case of isotropic conductivities the conductivity is a position dependent scalar. For example, a homogeneous unit sphere implies that $\sigma(x, y, z) = \text{constant}$ for $x^2 + y^2 + z^2 \leq 1$ whereas a 3-sphere conductor model has a piecewise constant conductivity, as depicted in figures 1.3(b) and 1.4(b). For anisotropic conductivities the conductivity can be written as a position dependent second order tensor. On top of equation (1.1) we have a boundary condition which states that no electric current can flow from Ω in the outside air (it would be unpleasant getting an electric shock each time you caress someone on the head). This boundary condition is called the homogeneous Neumann boundary condition and reads:

$$\nabla V \cdot \mathbf{e}_\Omega = 0, \quad \text{on } \partial\Omega, \tag{1.2}$$

where $\mathbf{e}_\Omega$ is the outward normal to the conductor model's surface, $\partial\Omega$.

As mentioned before, neighboring pyramidal cells are generators of a measurable EEG. Such a *patch* of pyramidal cells is adequately modeled by a current dipole [11, 12]. Therefore, the generating source distribution ρ is usually modeled by a superposition of M current dipoles:

$$\rho = \sum_{m=1}^{M} \mathbf{p}_m \cdot \nabla \delta (\mathbf{x} - \mathbf{x_m}), \tag{1.3}$$

where $\mathbf{p}_m = [p_{x_m}\ p_{y_m}\ p_{z_m}]^T$ and $\mathbf{x}_m = [x_m\ y_m\ z_m]^T$ represent the m^{th} dipole's moment and location. A dipole's moment determines its strength, also called intensity, $||\mathbf{p}_m||$ and orientation whereas its location determines where current is injected and subtracted. Naturally the dipoles' locations should all lie in the brain because there are no current sources outside the brain. Figures 1.3(a) and 1.4(a) depict the potential generated by such dipoles on the boundary of a homogeneous sphere and on the boundary of a 3-sphere model. The inverse EEG problem $\mathcal{P}$ at hand is the following:

$\mathcal{P}$: Knowing $V\big|_{\partial\Omega}$, find ρ in (1.3), such that (1.1) and (1.2) are satisfied.

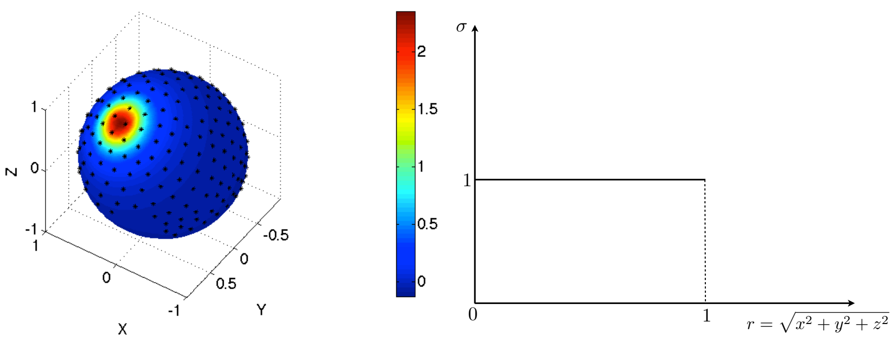

(a) (b)

Figure 1.3: 1.3(a) depicts the boundary potential generated by a dipole located at $\mathbf{x}_1 = [0.2, 0.4, 0.6]$ with a radial unit moment, $\mathbf{p}_1 = \frac{\mathbf{x}_1}{||\mathbf{x}_1||}$.1.3(b) The conductivity profile corresponding to a homogeneous sphere in which the generating dipole lies.

1.4 Overview of existing methods

The fundamental problem of reconstructing the sources responsible for a measured EEG is the ambiguity (also known as ill-posedness) of the inverse EEG problem, i.e.,

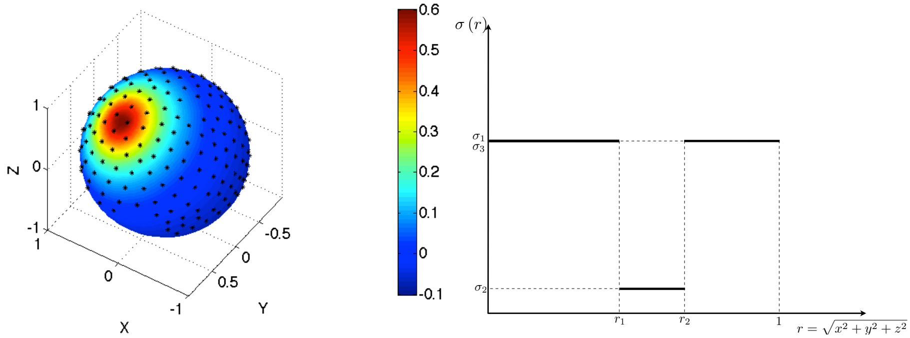

(a) (b)

Figure 1.4: 1.4(a) The boundary potential generated by a dipole located at $\mathbf{x}_1 = [0.2, 0.4, 0.6]$ with a radial unit moment, $\mathbf{p}_1 = \frac{\mathbf{x}_1}{||\mathbf{x}_1||}$.1.4(b) The conductivity profile corresponding to a 3-sphere conductor model in which the generating dipole lies.

multiple source distributions can generate the same boundary potential [13]. For example, if we measure no potential difference at the electrode sites then $\rho(\mathbf{x}) = 0$ is a plausible source distribution, but $\rho(\mathbf{x}) = -\operatorname{div}\left(\sigma\nabla(1 - ||\mathbf{x}||^2)^2\right)$ generates the same boundary potential because for any point on the surface, $\mathbf{x}_{\partial\Omega}$, we have $||\mathbf{x}_{\partial\Omega}|| = 1$. In order to suppress this ambiguity and as a consequence render the inverse EEG problem well-posed the source distribution is parameterized, as in (1.3). Only by introducing a priori assumptions (e.g., a limited number of dipoles M to be localized) can the problem $\mathcal{P}$ be solved. These a priori assumptions are crucial since they have a big impact on the proposed solution. This section is basically a brief overview of the most used a prioris and is largely based on [14].

Generally speaking, there are underdetermined and overdetermined inverse models. Underdetermined models do not make a strong a priori assumption on the number, M, of generating dipoles. They assume that M is much bigger than Q, where Q is the number of measurements on the boundary. Overdetermined models, on the contrary, make strong assumptions on the number of generating dipoles and assume that M is much smaller than Q.

1.4.1 Underdetermined source models

In many applications the exact number of generating dipoles unknown. In such, these underdetermined models, also called distributed models, have received increased attention. These distributed models use biological constraints, i.e., M current dipoles are placed on a grid in the brain where a possible current dipole might reside. These locations are called solution points. Note, the positions of the solution points are fixed, as a consequence the equations describing the inverse solution are linear, meaning that a matrix, called the lead field matrix, can be constructed that linearly relates the measured data to the estimated parameters $\mathbf{p}_m$. Since each solution point is considered as a possible location for a current dipole, there is no a priori assumption on the number of dipoles responsible for the measured EEG (provided that the ensemble of solution points is sufficiently large). When using such distributed models, $\mathcal{P}$ is reduced to finding the moments $\mathbf{p}_m$ of the solution points such that the ensemble of solution points explains the measured boundary potential. Since the solution points greatly outnumber the boundary measurements, the corresponding inverse problem is highly underdetermined, i.e., the solution points' moments are not uniquely determined by the boundary measurements.

The underdetermined nature of these distributed models necessitate more priori assumptions to identify the optimal or most likely solution. The different distributed models proposed in the literature differ in their choice of these extra assumptions. Some are purely mathematical, e.g., when looking for the solution with minimum ℓ_1-norm, some incorporate physiological knowledge and others incorporate findings from other imaging modalities such as magnetic resonance imaging (MRI). Note that, these assumptions are only valid if source distributions fulfilling these assumptions are more likely to occur than other source distributions.

Minimum norm

The most widespread a priori used to solve such underdetermined linear systems is the minimum ℓ_2-norm [15], i.e., the solution, $\hat{\mathbf{p}}$, that is assumed to be the most likely is the one with minimum overall intensity:

$$\hat{\mathbf{p}} = \underset{\mathbf{p}_1 \cdots \mathbf{p}_M}{\operatorname{argmin}} \sum_{m=1}^{M} ||\mathbf{p}_m||_{\ell_2}^2 \quad \text{subject to} \quad ||V - \sum_{m=1}^{M} V\left(\mathbf{p}_m\right)||_{\ell_2} = 0$$

where V is the measured potential and $V(\mathbf{p}_m)$ is the potential generated by the m^{th} solution point with moment $\mathbf{p}_m$. The obtained solution is unique, i.e., no other combination of found parameters $\mathbf{p}_m$ can fit the data exactly whilst having a minimal overall intensity. The minimum ℓ_2-norm solution favors sources close to the boundary, $\partial\Omega$, because such superficial sources require a lower intensity to generate a high potential difference at the surface. As a consequence, deeper sources with high intensity are incorrectly projected closer to the surface. For completeness, we mention that lately the solution with minimum ℓ_1-norm has been receiving a lot of attention [16]. The minimum ℓ_1-norm solution favors "sparse" solutions, i.e., the measured boundary potential is explained with a minimal number of solution points. In other words, the intensities of the solution points that do not contribute much to the boundary measurements are set to zero, or close to zero.

Weighted minimum norm

In order to suppress the tendency to favor superficial sources of the minimum ℓ_2-norm solution, different weighting strategies have been proposed. The most likely solution $\hat{\mathbf{p}}$ is then given by the minimization of regularization term whilst constraining the solution to reconstruct the measured potential. One such weighting, and probably the easiest, is based on the norm of the columns of the lead field matrix $\mathbf{L}$ [17]

$$\hat{\mathbf{p}} = \underset{\mathbf{p}_1\cdots\mathbf{p}_M}{\operatorname{argmin}} ||\mathbf{L}\mathbf{p}||_C \quad \text{subject to} \quad ||V - \sum_{m=1}^{M} V(\mathbf{p}_m)||_{\ell_2} = 0$$

with $||.||_C$ some viable norm that does not favor superficial sources. Another widely used technique is the Focal Underdetermined System Solution (FOCUSS) algorithm which iteratively changes the weighting matrix according to the solution estimated in a previous step, leading to a non-linear solution [18]. In [19] physical constraints are imposed such that the radial components disappear when approaching the surface of the brain. The resulting method is called radially weighted minimum norm (RWMN) solution. Bear in mind that these different weighting strategies are based on purely mathematical operations without any physiological justification for the choice of the weighting.

Laplacian weighted minimum norm

The Laplacian weighted minimum norm solution, which is implemented in the LORETA-software [20], chooses a solution with a spatially smooth distribution by minimizing the Laplacian, a measure of spatial roughness, of the intensities of the solution points. The optimal solution $\hat{\mathbf{p}}$ is then given by

$$\hat{\mathbf{p}} = \underset{\mathbf{p}_1 \cdots \mathbf{p}_M}{\operatorname{argmin}} \, || \sum_{m=1}^{M} \Delta V\left(\mathbf{p}_m\right) ||_{\ell_2} \quad \text{subject to} \quad ||V - \sum_{m=1}^{M} V\left(\mathbf{p}_m\right) ||_{\ell_2} = 0.$$

The physiological interpretation of these smoothing constraints is that the activity in neighboring neurons is correlated. This assumption is generally accepted. However, it has been criticized that the distance between solution points and the limited spatial resolution of EEG recordings lead to a spatial scale where such correlations are no longer valid [21, 22]. Indeed, functionally very distinct areas can be anatomically very close. The LORETA algorithm does not explicitly take into account such anatomical distinctions and hence the spatial smoothing constraint as physiological justification should be taken with caution. As a consequence, the LORETA algorithm yields often blurred or rather over-smoother solutions [23, 24].

Local autoregressive average

Local autoregressive average, also called LAURA, incorporates physical constraints in the minimum norm solution, i.e., according to Maxwell's equations the strength of the potential field falls off or regresses as $\frac{1}{r^2}$, with r the distance to the current source. LAURA implements this constraint as a local autoregressive average with coefficients depending on the distances between the solution points [25, 26]. Thus, the moment of a solution point depends on two contributions, one fixed by physical constraints and one to be determined from the measured data. This method could take into account anatomical details by varying the regression coefficients. Furthermore, dependencies between the dipole moments can be taken into account [26].

EPIFOCUS

EPIFOCUS is an algorithm that has been developed for the analysis of focal epileptic activity (hence the name EPIFOCUS) where a single dominant current source with a certain spacial extent is a valid a priori [27, 28, 29]. The spatial extent is derived from the measured EEG by projecting the measured EEG on each solution point. The result can be interpreted as the probability of finding a single source at each solution point. Both simulations and analyses of real data show a remarkable robustness against noise of EPIFOCUS. However, this method is likely to fail if several sources are simultaneously active.

Beamformer Approaches

Beamformer approaches adopted from radar and sonar signal processing have been applied to magneto encephalogram (MEG) and EEG. These approaches estimate the activity of one brain area by minimizing the interference with other possible simultaneous active areas (e.g., given by the solution points). A spatial filter is constructed that blocks the contributions of all sources, which are considered as background noise, other than the solution point of interest. A well-known method is synthetic aperture magnetometry (SAM) [30]. Beamformer approaches can be interpreted as a source scanning procedure that can estimate source changes over time of any voxel [31, 32]. The main drawback of beamformer approaches is the potentially erroneous estimation of radial current dipoles (current dipoles with a radial moment), which unfortunately are often the generating current sources in EEG, e.g., the focal epileptic onset zone is mostly modeled by a radial current dipole.

Bayesian Approaches

Bayesian approaches use statistical techniques to incorporate a priori information. The dipoles' parameters ($\mathbf{p}_m$ and $\mathbf{x}_m$) are obtained by optimizing a likelihood function which yields linear or non-linear estimators [33]. The non-linear estimators are most promising because they allow a more detailed description of a priori information, e.g., information on the neural current [34], the sparse activity pattern of epileptic onset zones [35] and spatial and temporal constraints on the sources [36].

1.4.2 Overdetermined source models

Overdetermined source models assume that the measured EEG can adequately be explained by a small number of current dipoles (overdetermined models are also called dipolar or multiple-dipole models). To guarantee a unique solution the number of estimated parameters ($6 \times M$) must be smaller than the number of boundary measurements. These dipoles are found by computing the generated boundary potential and comparing the obtained potential map with the measured EEG. The optimal locations $\mathbf{x}_m$ and moments $\mathbf{p}_m$ minimize the squared error between the generated potential map and the measured EEG:

$$\underset{\mathbf{x}_1 \cdots \mathbf{x}_M, \mathbf{p}_1 \cdots \mathbf{p}_M}{\operatorname{argmin}} ||V - \sum_{m=1}^{M} V\left(\mathbf{x}_m, \mathbf{p}_m\right)||_{\ell_2},$$

with $V\left(\mathbf{x}_m, \mathbf{p}_m\right)$ the potential generated by a dipole located at $\mathbf{x}_m$ with moment $\mathbf{p}_m$. Note that, the only the grid's nodes are considered as viable locations for the dipoles. However, such approaches have two big drawbacks:

(1) An exhaustive scanning through the whole solution space with any possible location and moment of the estimated dipoles is almost impossible since the solution space is too big.

(2) Non-linear optimization methods based on directed search algorithms, such as the steepest descend algorithm, are often used to search through the solution space [37]. However, such non-linear optimization methods are prone to local minima, i.e., the algorithm may falsely accept a certain location because moving in any direction increases the squared error [38]. This problem is even more pronounced if the measured data is noisy, which is, in practice, always the case.

In order to increase the number of dipoles that can be fitted, temporal information can be incorporated in the dipole fitting procedure [39]. The resulting spatiotemporal multiple source analysis technique (as implemented in the BESA software) fixes the dipoles positions over a given time interval and uses the data over the entire time interval to perform a least squares fit. As a result only the dipoles' moment vary over the considered time interval. In such, it is crucial to assume the correct number of dipoles. Generally two approaches are proposed [40]. In a first approach, the entire time window is analyzed and and new sources are added as the explained variance increases considerably, e.g., the method called "multiple signal classification" (MUSIC) uses this approach [41]. In the second approach, the time interval is analyzed sequentially and new dipoles are added for each time instant at which unexplained activity remains, such methods are explored and tested in [42].

Another interesting approach uses a ubiquitous tool in electromagnetism, known as the reciprocity gap concept [43]. This tool is essentially an application of Green's theorem, which provides a way to transform a scalar product between the source distribution and a function with vanishing Laplacian into a boundary integral. It has been shown that the application of this tool to powers of $x + iy$ leads to an algorithm that solves the localization problem [44, 9]. Unfortunately, the practical efficiency of their approach to multi-pole sources retrieval is severely hindered by the numerical instability of higher degree monomials.

Recently, an interesting mathematical approach has been proposed in 2D. Based on the analytical expression of the potential induced by multiple dipoles in a disc with uniform conductivity, one can fit their trace on the boundary measures by a so-called best-meromorphic approximation, which contains the information of the dipoles' positions [45, 46]. However, the method is only exact in specific cases and also relies on the circular form of the boundary. Since the method is intrinsically 2D, its extension to 3D is iterative and becomes more difficult with an increasing number of dipoles [47].

1.4.3 Sparse signal models

Recently, in the signal processing community, a novel approach, called "finite rate of innovation (FRI)" has been proposed [48, 49]. This method makes ingenuously use of Prony's method [50] to reconstruct a stream of Diracs. Prony observed in 1795 that a sum of complex exponentials can be nullified (or annihilated) by a filter whose coefficients are found as the roots of an "annihilating" polynomial. The FRI framework relates a stream of Diracs to a sum of complex exponentials via which a stream of Diracs can be reconstructed. The source of inspiration for our approach is the FRI approach.

1.5 Main Contributions of this Thesis

In this thesis we attempt to devise a parametric estimation of the underlying dipolar source model, $\rho = \sum_{m=1}^{M} \mathbf{p}_m \cdot \nabla\delta\left(\mathbf{x} - \mathbf{x_m}\right)$, responsible for the measured boundary potentials. The main contributions fall under the following three headings:

(1) **Theory** The developed framework, coined "analytic sensing", solves the inverse problem $\mathcal{P}$ using a multi-dipole source model. Starting from the governing equations (1.1) and (1.2), we identify test functions, ψ_{a_n}, such that the inner product $\langle \psi_{a_n}, \rho \rangle$, called generalized samples, can be computed knowing only $V\big|_{\partial\Omega}$. If the test functions are harmonic then this concept is known as the "reciprocity gap concept". However, we use test functions that are not analytic outside the domain of interest, i.e., unlike the polynomials considered in [44, 9]. Next, we adapt a FRI strategy [48, 49] and provide an algorithm that based on a set of such generalized samples can reconstruct the dipoles' parameters exactly in the absence of noise.

(2) **Computational Efficient Algorithms** Most of the existing multi-dipole models require the optimization of several non-linear parameters, which is done by scanning through the solution space which is usually very big. Our approach leads to an analytical solution of the inverse problem $\mathcal{P}$. In such no iterative process is needed to reconstruct $\mathbf{x}_m$ and $\mathbf{p}_m$. Moreover, the estimation of the non-linear parameters ($\mathbf{x}_m$) and linear parameters ($\mathbf{p}_m$) is decoupled.

(3) **Applications** First we applied our algorithm in an ideal setup and compared the obtained localization error with the theoretical minimal error (given by the Cramér-Rao bounds). Second, we demonstrate the potential of our algorithm on realistic data (we analyzed an averaged visual evoked potential obtained from a healthy subject). We show that our algorithm may be potentially fruitful in the field of optics where the generating model is often given by Helmholtz's equation (the test function ψ_{a_n} can be adapted to accommodate this generating model). Other possible but unexplored applications of our method are crack detection [43, 51], basically any problem governed by Helmholtz's equation.

1.6 Outline of thesis

The goal of this work is to solve the inverse EEG problem. In this chapter, chapter 1, we showed that the inverse EEG problem is an ill-posed problem because the measured EEG does not uniquely determine the underlying source distribution. To render the problem well-posed we introduced an a priori on the source distribution; i.e., we assumed that the source distribution can be written as a sum of dipoles, which renders the problem well-posed. Then, we gave an overview of the already existing methods to solve this well-posed inverse problem (e.g., LAURA, MUSIC, etc).

In chapter 2, we consider a simplified setting; i.e., a 2D homogeneous setting. We show that we can obtain measures, called "generalized measures", of the unknown source distribution knowing the generated boundary potential. This involves applying Green's theorem in combination with a well-chosen analytic function, termed an "analytic sensor". Next, we adapt Prony's method and derive an algorithm to reconstruct the locations of the generating dipoles; i.e., we construct a filter that relates the generalized measures to a polynomial whose roots are the locations of the source distributions. On the other hand, the moments depend linearly on the generalized samples and are hence deduced directly from those once the dipoles' locations are known.

In chapter 3, we extend the framework shown in chapter 2 to a 3D setting. We observe that the computation of these measures can readily be adopted to 3D. Next, we show that applying the reconstruction algorithm described in chapter 2 yields orthographic projections of the dipolar sources. A priori, we do not know which projections stem from the same dipole. We adapt "Tomasi and Kanade's rank principle" to establish the proper correspondence from which we can easily reconstruct the full 3D information.

In chapter 4 we give a comprehensive overview of what has been developed in chapters 2 and 3. Moreover, a flowchart is given of the reconstruction process thus far. Next, we have a look at what loose ends need to be tied together to obtain a functional reconstruction algorithm; e.g., we should be able to cope with non-homogeneous conductor models.

In chapter 5 we extend our reconstruction algorithm to cope with non-homogeneous conductor models. This requires solving Poisson's equation, which we show is possible analytically if we assume that the conductivity varies radially. An often used head model is the 3-sphere head model. In this case the conductivity not only varies radially but is a piecewise constant. We explicitly construct analytic sensors for such 3-sphere head models.

In chapter 6 we tie together the last loose ends. We assumed that we know the potential in a continuous way on the boundary. In reality, we only have a finite number of boundary measurements. In order to compute the generalized measures we need a continuous representation of the boundary potential. We develop an approximation of the boundary potential using the boundary measurements. We use spherical harmonics in combination with some regularization, which ensures a good approximation. Since the reconstruction algorithm is a non-linear estimation technique and the generalized samples are forcefully noisy (due to the approximation error) we have to compensate for the presence of noise. For this we adapt an iterative denoising scheme known as Cadzow's iterative denoising algorithm.

In chapter 7 we characterize our reconstruction algorithm in terms of performance. First, we construct theoretical lower bounds on the localization error in the presence of noise. Second, we study its behavior in the presence of noise by comparing the obtained localization errors to the theoretical smallest error. We show to what extent the proposed framework can be spatially selective enabling us to reconstruct the entire source distribution dipole per dipole. We show the feasibility of our method in a real EEG setting by treating a visual evoked response potential.

Finally, in chapter 8, we conclude with a small wrap-up (e.g.,"What have we solved?", "Why is it worth considering our method?"), a discussion ("Is the inverse EEG problem truly solved?" or on a more philosophical note"Occam's razor versus distributed models") and an outlook ("Are there other applications out there?").

Chapter 2

Analytic Sensing: Homogeneous 2D Case

This chapter is based on the article "*Analytic Sensing: Noniterative Retrieval of Point Sources from Boundary Measurements*, *SIAM Journal on Scientific Computing*, *vol 31:(4) pp. 3179-3194, 2009.*

2.1 Summary

Before considering the 3D setting of the EEG problem, we consider a homogeneous 2D setting in this chapter. In chapters 3 and 5 we extend our approach to a 3D inhomogeneous setup.

We use Green's divergence theorem to obtain test functions that yield a measure on the source distribution knowing only the generated boundary potential. We identify a suitable class of analytic test functions that allow for a non-linear estimation technique to reconstruct the locations and moments, in a non-iterative way, from the computed measures. We demonstrate the effectiveness of the obtained estimation technique by comparing the obtained reconstruction errors with the theoretical smallest reconstruction errors.

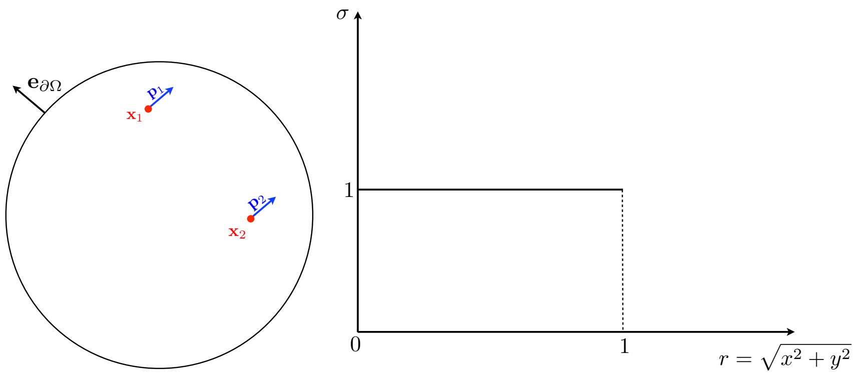

(a) (b)

Figure 2.1: Figures 2.1(a) and 2.1(b) depict a homogeneous 2D conductor model, i.e., a homogeneous unit circle and its corresponding conductivity profile, $\sigma(r)$. Moreover, we plotted 2 dipoles in the circle, the red dots represent the dipoles' locations, $\mathbf{x}_m = [x_m y_m]^{\mathrm{T}}$, and the blue arrows represent the dipoles' moments, $\mathbf{p}_m = [p_{x_m} p_{y_m}]^{\mathrm{T}}$.

2.2 Motivation

Our goal is to develop a method to reconstruct the generating dipole source distribution ρ from the measured boundary potential $V\big|_{\partial\Omega}$. We develop an analytical technique that is able to reconstruct the location and moment parameters of the underlying source distribution.

As a first step we construct measures, called generalized samples, of ρ knowing only $V\big|_{\partial\Omega}$. These measures should be independent of the nature of ρ; i.e., we should be able to compute these generalized samples for all types of sources, not just point sources. Second, these generalized samples should encode information on the conductor profile and sources in such a way that it will allow for a non-iterative retrieval of $\mathbf{x}_m$ and $\mathbf{p}_m$. We will see that such generalized samples are obtained by applying Green's theorem on the boundary potential with a well-chosen test function, ψ, which is called an analytic sensor.

The construction of such analytic sensors requires solving Poisson's differential equation, $\operatorname{div} \sigma \nabla \psi = 0$, which is non-trivial in the case of non-homogeneous conductor models. In this chapter, we assume that $\sigma = \text{Constant}$ and hence we only consider homogeneous conductor models here (as depicted in figure 2.1). In such, any Ω-analytic function yields such a generalized measure. We will opt for logarithmic functions of $z = x + iy$, in particular $\psi = \ln(z - a)$, since these allow for a direct reconstruction algorithm.

2.3 Sensing Principle

We want to obtain (or rather construct) a measure on ρ knowing only the generated boundary potential $V\big|_{\partial\Omega}$. This measure should be independent from the nature of the generating source. Then, we can try to reconstruct the generating source from the constructed measures taking into account all the prior knowledge available, e.g., the parametric form of the ρ. The Sensing Principle shows us how to construct such measures.

If we consider "test" functions ψ such that

$$\operatorname{div}(\sigma \nabla \psi) = 0, \quad \text{within } \Omega, \tag{2.1}$$

then we can sense the manifestation of any source distribution ρ in Ω. When σ is constant in Ω, this reduces to the functions whose Laplacian vanishes in Ω, a large subset of which are Ω-analytic functions (functions that are analytic in Ω). The fundamental observation is that if V is known on the boundary $\partial\Omega$, then we can exactly calculate the scalar products $\langle \psi, \rho \rangle = \int_\Omega \psi(\mathbf{x})\rho(\mathbf{x})\,\mathrm{d}^2\mathbf{x}$ for such test functions, as shown by the following theorem.

Theorem 1 (2D Sensing Principle)**.** *Let V be the quasi-static potential induced by some source distribution, ρ, according to (1.1) and (1.2). Moreover, suppose that we know V on the boundary $\partial\Omega$. Then, if we choose ψ according to (2.1), the scalar product $\langle \psi, \rho \rangle$ can be expressed as a line integral according to:*

$$\langle \psi, \rho \rangle = -\int_{\partial\Omega} \sigma V \nabla \psi \cdot \mathbf{e}_\Omega \,\mathrm{d}s. \tag{2.2}$$

The scalar products $\langle \psi, \rho \rangle$ can be seen as "generalized" samples of the unknown distribution ρ.

Proof. We have the following identity:

$$\psi \operatorname{div}(\sigma \nabla V) - V \operatorname{div}(\sigma \nabla \psi) = \operatorname{div}\big(\sigma \psi \nabla V - \sigma V \nabla \psi\big)$$

If we choose ψ to be a test function that satisfies (2.1) then, by applying (1.1), this identity becomes:

$$\psi \rho = \operatorname{div}\big(\sigma \psi \nabla V - \sigma V \nabla \psi\big).$$

Integrating both sides over Ω and applying Green's divergence theorem yields

$$\langle \psi, \rho \rangle = \int_{\partial\Omega} (\sigma \psi \nabla V - \sigma V \nabla \psi) \cdot \mathbf{e}_\Omega \, \mathrm{d}s.$$

The boundary condition (1.2) further simplifies the Left-Hand Side (LHS) to (2.2) which proves the theorem. □

Note that, equation (2.2), which we coined "2-D Sensing Principle", is valid for any source distribution, not just dipolar source distributions such as (1.3). It is potentially fruitful to describe ρ through of a large collection of measurements $\langle \psi, \rho \rangle$. For instance, if we could compute these scalar products for any $\psi \in \mathcal{D}(\Omega)$ (the set of infinitely differentiable functions in Ω), then the generalized samples $\langle \psi, \rho \rangle$ would represent ρ completely and uniquely in the sense of distributions.

Unfortunately, the test functions are here restricted to those that satisfy $\operatorname{div}(\sigma \nabla \psi) = 0$. These functions form a much more constrained class that is unable to characterize the full generality of source fields; an issue that is a direct consequence of the ill-posedness of the inverse EEG problem. Note that, a priori, we can choose any test function that satisfies (2.1). These test functions form the link between the boundary measurements on $\partial\Omega$ and the generalized samples $\langle \psi, \rho \rangle$.

2.3.1 Homogeneous medium

In this chapter, we only consider in detail the case where σ is constant in Ω. Nevertheless, it is possible to accommodate for varying σ as explained in chapter 5. Such a homogenous 2D conductor model is depicted in figure 2.1.

Thanks to the homogeneity hypothesis, the set of test functions satisfying (2.1) is made of Ω-harmonic functions, a large subset of which are functions that are analytic in Ω, e.g., polynomials in $z = x + iy$, which were used [44, 9]. We will opt for rational functions of z that do not have any poles in Ω and coin the term "analytic sensor" for such functions and hence call our approach "analytic sensing".

Corollary 1. *Let ψ be an analytic sensor. If we use the analytic formalism, then we can compute the associated generalized sample, $\mu = \langle \psi, \rho \rangle$, as follows:*

$$\mu = i\sigma \int_{\partial\Omega} V(x, y)\psi'(z) \, \mathrm{d}z, \tag{2.3}$$

Proof. If ψ is an analytic function, i.e., a differentiable function of $z = x + iy$, then $\nabla\psi = \psi'(z)[1, i]^{\mathrm{T}}$. Moreover, $\mathbf{e}_\Omega \, \mathrm{d}s = [\,\mathrm{d}y, -\mathrm{d}x]^{\mathrm{T}}$ which implies that $\nabla\psi \cdot \mathbf{e}_\Omega \, \mathrm{d}s = -i\psi'(z)\,\mathrm{d}z$. By application of Theorem 2.2 this proves (2.3). □

2.3.2 Choice of the test-functions

Now that the problem is well-formulated and well-posed, i.e., we want to estimate the sources locations and moments from a set of such generalized measures $\langle \psi, \rho \rangle$, we need to choose the sensors in a way that the corresponding generalized samples allow us to determine algorithmically the positions and the intensities of the sources. For that purpose, we choose the following family of analytic test functions:

$$\psi_{a_n}(z) = \ln(z - a_n), \quad a_n \notin \Omega. \tag{2.4}$$

Moreover, we will further restrict our choice of a_n to the form $a_n = \alpha_n e^{in\theta}$, where $n \in \{0, \cdots, N-1\}$.for some $N > 2M$ and $\theta \in \,]0, 2\pi[$. The radius $|\alpha_n|$ is chosen such that $\alpha_n \notin \Omega$. Note that, since the radii may vary we can choose a_n such that it follows the $\partial\Omega$, this setup is depicted in the figure 2.2. Note that the angle θ is completely arbitrary; in particular, we do not need $N\theta$ to be equal to 2π. Actually, $N\theta$ could even be close to 0 meaning that the poles of the analytic sensors would all be located in the neighborhood of α_0.

Another very interesting characteristic of these analytic sensors is that they are "localized", and this all the more as their poles are closer to $\partial\Omega$, as depicted in figure 2.3. This means that it is conceivable to compute a good approximation of the integral in (2.3) only with values of the potential that are close to the pole, a, of the sensor, ψ_a.

2.3.3 A note on missing data

In practice, V is not continuously known on the boundary $\partial\Omega$; i.e., we measure $V(\mathbf{x}_n), n \in \{0, \cdots, N-1\}$ where $\mathbf{x}_n \in \partial\Omega$. Hence, we need an interpolation/approximation method to reconstruct the continuous-domain representation

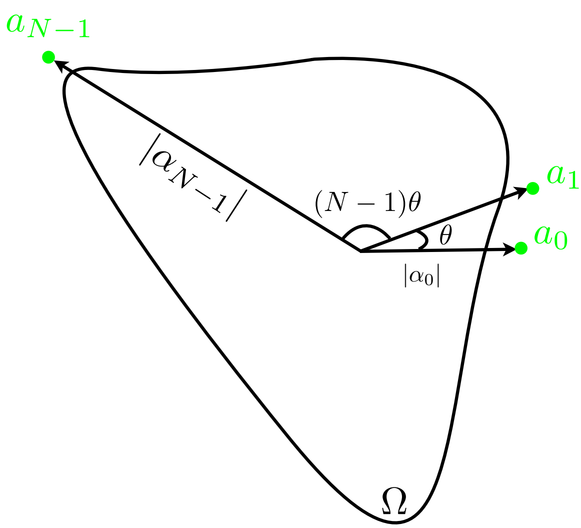

Figure 2.2: The poles, $a_0 \cdots a_{N-1}$, and their placement outside of Ω. For each pole there is a corresponding analytic sensor $\psi_{a_n}(z) = \ln(z - a_n)$.

of $V\big|_{\partial\Omega}$. In order to give an insight of what actually happens, we consider the simplified case where $\partial\Omega$ is a circle with radius 1 and where V is measured at the N uniform angles $\theta_n = 2n\pi/N$ for $n = \{0, \cdots, N-1\}$. With limited ambiguity, we denote by $V(\theta)$ the measure of the electric potential at angle θ and by $\tilde{V}(\theta)$ its interpolated version. More specifically, we assume $N = 2K + 1$ to be odd and develop V and $\tilde{V}$ in Fourier series:

$$V(\theta) = \sum_{m \in \mathbb{Z}} c_m e^{im\theta}, \qquad \text{and} \quad \tilde{V}(\theta) = \sum_{m=-K}^{K} \tilde{c}_m e^{im\theta}. \tag{2.5}$$

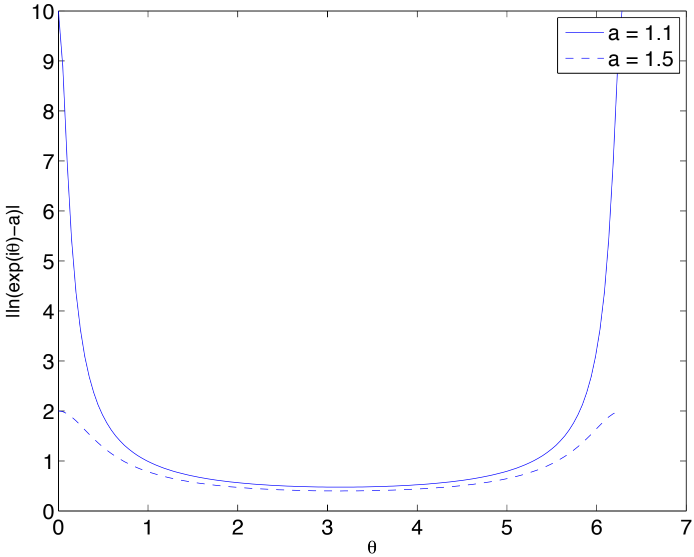

Figure 2.3: The magnitude, $||\nabla\psi_{a_n}||$, of the gradient of such an analytic sensor for the singularities $a = 1.1$ and $a = 1.5$ on the unit disc $\mathcal{S}$. We see that ψ_{a_n} is well-localized around a_n and more so if a_n is close to $\mathcal{S}$.

The coefficients $\tilde{c}_m$ are obtained by solving a linear system of equations that expresses the constraints of the measurements $\tilde{V}(\theta_n) = V(\theta_n)$, $n = \{0, \cdots, N-1\}$:

$$V(\theta_n) = \sum_{m=-K}^{K} \tilde{c}_m e^{im\theta_n}. \tag{2.6}$$

Thanks to our specific choices, these coefficients can be expressed directly using a Discrete Fourier Transform (DFT) of the measurements

$$\tilde{c}_m = \frac{1}{N} \sum_{n=-K}^{K} V(\theta_n) e^{-im\theta_n} = \sum_{n\in\mathbb{Z}} c_{m+Nn}, \tag{2.7}$$

by replacing $V(\theta_n)$ with its Fourier expansion (2.5). The last identity implies that

$$\sum_{m=-K}^{K} |\tilde{c}_m - c_m| \leq \sum_{|m|>K} |c_m| \tag{2.8}$$

and in particular $|\tilde{V}(\theta) - V(\theta)| \leq 2\sum_{|m|>K} |c_m|$: not so surprisingly, the interpolation error is bounded by (twice) the ℓ^1 norm of the "truncated" Fourier coefficients.

We now consider the generalized measures $\mu_n = \langle \psi_{a_n}, \rho \rangle$ with N analytic sensors located at $a_n = a_0 e^{i\theta_n}$. Using the Fourier representation (2.5) of $V(\theta)$ in (2.3), we have that

$$\begin{aligned} \mu_n &= i\sigma \int_{\partial\Omega} V(\theta)\psi'_{a_n}(z)\,\mathrm{dz} \\ &= i\sigma \sum_{m\in\mathbb{Z}} c_m \int_{\Omega} \psi'_{a_n}(z)\, e^{im\theta}\mathrm{dz} \\ &= i\sigma \sum_{m\in\mathbb{Z}} c_{-m} \int_{\Omega} \frac{\psi'_{a_n}(z)}{z^m}\mathrm{dz}. \end{aligned} \tag{2.9}$$

Knowing that ψ_{a_n} is analytic in Ω and using Cauchy's theorem we can deduce:

$$\begin{aligned} \mu_n &= -2\pi\sigma \sum_{m=1}^{\infty} c_{-m} \frac{\psi_{a_n}^{(m)}(0)}{(m-1)!} \\ &= 2\pi\sigma \sum_{m=1}^{\infty} \frac{m c_{-m}}{a_n^m}. \end{aligned} \tag{2.10}$$

and finally

$$e^{i\theta_n}\mu_n = \sum_{m=-\infty}^{-1} -2\pi\sigma \frac{m c_m}{a_0^{-m}} e^{im\theta_n}. \tag{2.11}$$

Similarly, if we replace $V(\theta)$ by its interpolation $\tilde{V}(\theta)$ in (2.3) and denote by $\tilde{\mu}_n$ the approximated generalized measure, we get

$$e^{i\theta_n}\tilde{\mu}_n = \sum_{m=-K}^{-1} -2\pi\sigma \frac{m\tilde{c}_m}{a_0^{-m}} e^{im\theta_n}. \tag{2.12}$$

First, we can bound the error between the actual, computable, generalized measures $\tilde{\mu}_n$ and the inaccessible ones μ_n:

$$|\tilde{\mu}_n - \mu_n| \leq \max_{m\geq 1} \frac{2\pi\sigma m}{|a_0|^m} \underbrace{\left(\sum_{m=-K}^{-1} |\tilde{c}_m - c_m| + \sum_{m<-K} |c_m| \right)}_{\leq 2\sum_{|m|>K} |c_m|}. \tag{2.13}$$

The computation error on the generalized measures is thus directly controlled by the ℓ^1 norm of the *out-of-band Fourier coefficients*, which is typically small when the function $V(\theta)$ is smooth.

Second, by bringing together (2.12) and (2.6), we conclude that the discrete sequence $e^{i\theta_n}\tilde{\mu}_n$ is a *filtered* version of $V(\theta_n)$, because the DFT coefficients of each sequence are equal, up to a multiplication by

$$H_{a_0}(m) = \begin{cases} -2\pi\sigma m a_0^{-m} & \text{for } -K \leq m < 0, \\ 0 & \text{for } m \geq 0 \text{ or } m < -K. \end{cases} \tag{2.14}$$

The magnitude response $|H_{a_n}(m)|$ is shown in Fig. 2.4 for different values of $|a_0|$. It is maximum for $m \approx -1/\ln|a_0|$. The filtering appears as a combination of a (flipped) Hilbert transform and band-pass filtering. The bandwidth of the filter increases as the pole's position approaches the boundary. This behavior indicates that $|a_0|$ should be chosen with respect to the noise characteristics of the measurements.

2.3.4 A note on non-homogeneous medium

In the case of a non-homogeneous medium, we only need to assume that σ is constant in the domain, Ω_0,where the sources lie. In that case, we may still choose $\psi|_{\Omega_0}$ to be of the form $\ln(z-a)$. Then, ψ can be propagated into $\Omega\backslash\Omega_0$ in such a way as to satisfy $\mathrm{div}(\sigma\nabla\psi) = 0$ using numerical techniques such as finite element methods or boundary element methods (for domains with piecewise constant σ). The propagation of the test functions up to the boundary $\partial\Omega$ implicitly encodes the information of the forward model in more complex configurations. Consequently, the generalized samples also take into account the presence of the non-homogeneous medium. The localization method as presented in the following section, however, remains identical. Within the context of EEG, one well-known head model is the

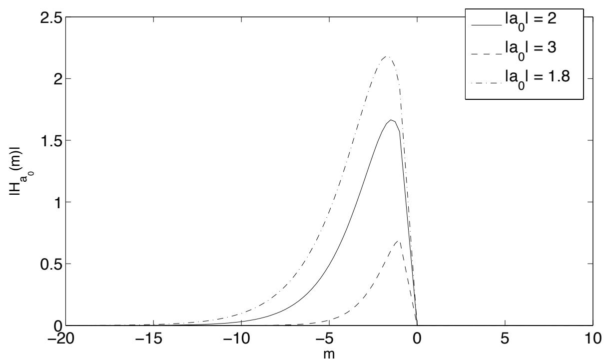

Figure 2.4: Magnitude of the frequency response of $H_{a_0}(m)$ that is the equivalent filter that links the boundary measures to the generalized measures. Different magnitudes of the pole a_0 are shown.

multi-layer sphere [52]. The conductivity is homogeneous in each spherical layer and the dipolar sources are assumed to be in the "gray matter" compartment. In chapter 5 we show explicitly (and analytically) how to adapt the analytic sensors to cope with such a multi-layer spherical conductor model.

2.4 The annihilating principle solution to the reconstruction problem

From now on we shall identify $\mathbf{x}_m$ with the complex plane, hence $\mathbf{x}_m \Leftrightarrow z_m = x_m + iy_m$. Now, we define the polynomial, $R(X)$, whose roots are the positions of the pointwise sources:

$$R(X) = \prod_{m=1}^{M} (X - z_m) = \sum_{k=0}^{M} r_k X^k. \tag{2.15}$$

Using (2.4) and the fact that $a_n = \alpha_n e^{in\theta}$, the following relationship exists between R and the generalized samples $\mu_n = \langle \psi_{a_n}, \rho \rangle$:

$$\mu_n = \sum_{m=1}^{M} c_m \psi'_{a_n}(z_m) = \frac{\sum_{m=0}^{M-1} c'_m e^{imn\theta}}{R(a_n)}, \tag{2.16}$$

where c'_m are complex-valued coefficients that do not depend on n nor θ. We now see that the generalized samples satisfy an "annihilating" equation.

Lemma 1. *Consider the FIR digital filter, $h = \{h_k\}_{k\in\mathbb{Z}}$, which has its zeros at $e^{ik\theta}$ for $k = 0, 1, \ldots, M-1$. It is characterized by the transfer function*

$$H(z) = \sum_{k\in\mathbb{Z}} h_k z^{-k} = \prod_{k=0}^{M-1} \left(1 - e^{ik\theta} z^{-1}\right).$$

Then, the filter h annihilates the sequence $u = \{u_n\}_{n=0,\ldots,N-1}$ whose coefficients are defined by $u_n = R(a_n)\mu_n$; i.e.,

$$(h * u)_n = 0, \quad \textit{for all } n \in \{M, \cdots, N-1\}. \tag{2.17}$$

Proof. Given an integer m in $\{0, M-1\}$, consider the discrete convolution of the sequence $\{e^{imn\theta}\}_{n\in\{0,N-1\}}$ with h. For an output index $n \in \{M, N-1\}$, its n^{th} element is given by the summation:

$$\sum_{k=0}^{M} h_k e^{im(n-k)\theta} = e^{imn\theta} H\left(e^{im\theta}\right) = 0.$$

On the other hand, by (2.16) we have $u_n = \sum_{m=0}^{M-1} c'_m e^{imn\theta}$ for $n \in \{0, N-1\}$. We can thus write, using the linearity of the discrete convolution, that

$$\sum_{k=0}^{M} h_k u_{n-k} = 0$$

for any output index $n \in \{M, N-1\}$, which proves our *claim.* $\square$

Theorem 2. *The coefficients r_k of the polynomial $R(X)$ defined by (2.15) satisfy the following linear system of equations:*

$$\begin{aligned} \sum_{k=0}^{M} A_{n,k} r_k = 0, \quad \textit{for } n \in \{M, N-1\} \\ \textit{where } A_{n,k} = \sum_{n'=0}^{N-1} h_{n-n'}\, a_{n'}^k \mu_{n'} \end{aligned} \tag{2.18}$$

In matrix form, this system can be expressed as $\mathbf{A}\mathrm{R} = \mathbf{0}$*, if we define the matrix* $\mathbf{A}$ *by* $[\mathbf{A}]_{n,k} = A_{n,k}$ *for* $n \in \{M, N-1\}$ *and* $k \in \{0, M\}$*, and the vector* $\mathrm{R} = [r_0, r_1, \ldots, r_M]^{\mathrm{T}}$*. Note that we have* $r_M = 1$*.*

Proof. By combining Lemma 1 and (2.15), we deduce the following:

$$\begin{aligned} 0 = \{h * u\}_n &= \sum_{n'=0}^{N-1} h_{n-n'} R\left(a_{n'}\right) \mu_{n'} \\ &= \sum_{n'=0}^{N-1} h_{n-n'} \sum_{k=0}^{M} r_k a_{n'}^k \mu_{n'} \\ &= \sum_{k=0}^{M} r_k \underbrace{\sum_{n'=0}^{N-1} h_{n-n'} a_{n'}^k \mu_{n'}}_{A_{n,k}} \end{aligned}$$

for all $n \in \{M, N-1\}$, which proves the theorem. □

Thus, combining Corollary 2.3 with Thm. 2 yields a non-iterative algorithm for localizing the dipolar sources given the generated boundary potential. That is, we first obtain the generalized measurements $\mu_n = \langle \psi_{a_n}, \rho \rangle$ from the observed boundary measurements, $V\big|_{\partial\Omega}$; then, by computing the polynomial, $R(X)$, according to (2.18) we are able to find the positions z_m by taking its roots. Once the positions of the point sources are known, we need to determine their moments, $\mathbf{p}_m$. The generalized samples μ_n depend linearly on the moments $\mathbf{p}_m$ as is clear from (2.16). Hence, determining the moments boils down to solving the following linear system of equations:

$$\sum_{m=1}^{M} \frac{\mathbf{p}_{m_x} + j\mathbf{p}_{m_y}}{z_m - a_n} = \mu_n, \quad n \in \{0, N-1\}.$$

Figure 2.5 schematizes the complete reconstruction algorithm.

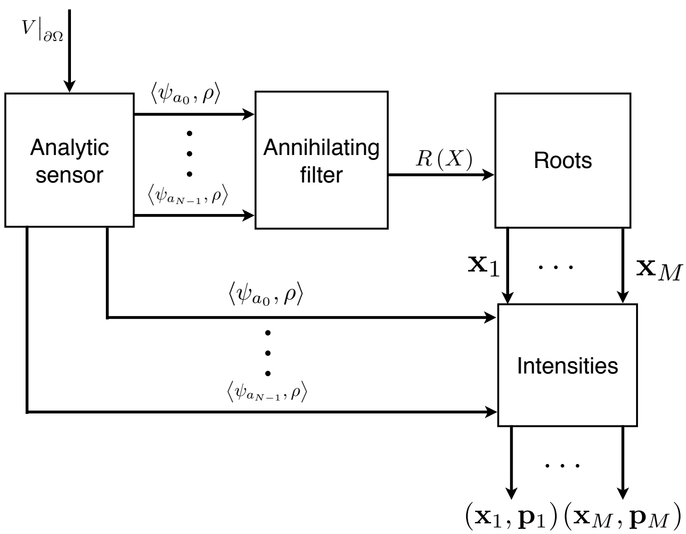

Figure 2.5: A flow-chart of the proposed algorithm to determine the positions of the point sources and their corresponding intensities.

The linear system in (2.18) with the additional constraint $r_M = 1$ make up $N - M$ equations in total. On the other hand, there are M unknown polynomial coefficients r_k, $k \in \{0, M-1\}$. Consequently, we do not need more than $N = 2M$ generalized measures μ_n to retrieve the coefficients r_k. Note that when considering the complete problem, the amplitudes c_m and source positions z_m make precisely $2M$ (complex) unknowns for $2M$ (complex) nonlinear equations (2.16). For the noiseless case and for M distinct source positions, it may be argued that $\text{rank}(\mathbf{A}) = M$ in general and therefore we find exactly and uniquely the M positions as the roots of the polynomial $R(X)$.

2.4.1 Implementation notes

The structure of $\mathbf{A}$ can be simplified by performing the following factorization:

$$\mathbf{A} = \mathbf{H}\boldsymbol{\mu}\mathbf{a}, \tag{2.19}$$

where, $\mathbf{H}$ is an $(N-M)\times N$ Toeplitz matrix representing the discrete filter h, $\boldsymbol{\mu}$ is a diagonal $N \times N$ matrix with μ_n, for $n \in \{0, N-1\}$, on the diagonal and $\mathbf{a}$ is a $N \times (M+1)$ Vandermonde matrix. More explicitly, the matrices $\mathbf{H}$, $\boldsymbol{\mu}$ and $\mathbf{a}$ read as follows:

$$\mathbf{H} = \begin{bmatrix} h_M & \cdots & h_0 & 0 & \cdots & 0 \\ 0 & h_M & \cdots & h_0 & \cdots & 0 \\ \vdots & \ddots & \ddots & \cdots & \ddots & \vdots \\ 0 & \cdots & 0 & h_M & \cdots & h_0 \end{bmatrix},$$

$$\boldsymbol{\mu} = \begin{bmatrix} \mu_0 & & 0 \\ & \ddots & \\ 0 & & \mu_{N-1} \end{bmatrix}$$

and

$$\mathbf{a} = \begin{bmatrix} a_0^0 & \cdots & a_0^M \\ \vdots & \ddots & \vdots \\ a_{N-1}^0 & \cdots & a_{N-1}^M \end{bmatrix}.$$

Since $\mathbf{H}$ is a convolution matrix, it is in general not unitary, even if it usually has maximal rank, and this may be detrimental to the computation of the polynomial $R(X)$ when the generalized measurements are not known with high enough accuracy. However, we observe that if we perform a singular value decomposition of $\mathbf{H}$ according to $\mathbf{H} = \mathbf{U}\mathbf{S}\mathbf{H}_0$, where $\mathbf{U}$ is an $(N-M)\times(N-M)$ unitary matrix, $\mathbf{S}$ is an $(N-M)\times(N-M)$ diagonal matrix and $\mathbf{H}_0$ is an $(N-M)\times N$ matrix satisfying $\mathbf{H}_0\mathbf{H}_0^\dagger = \mathbf{Id}$ then

$$\mathbf{A}\mathrm{R} = \mathbf{H}\boldsymbol{\mu}\mathbf{a}\mathrm{R} = 0 \quad \Leftrightarrow \quad \mathbf{A}_0\mathrm{R} = \mathbf{H}_0\boldsymbol{\mu}\mathbf{a}\mathrm{R} = 0 \tag{2.20}$$

whenever $\mathbf{H}$ has maximal rank; i.e., whenever $\mathbf{S}$ is non-singular. The Right-Hand Side (RHS) linear system of equations is actually much better conditioned and this is the one that we will consider for practical implementations.

2.4.2 Noise issues

The algorithm of the previous section assumes perfect data, but a practical situation has to cope with noise that inevitably corrupts measured data. Let us assume, for now, that the noise is an additive Gaussian noise. To compensate for the influence of noise, we made some minor adjustments to the method described above.

In the presence of noise, the generalized measures are distorted in such a way that the decomposition of $\mathbf{A}_0$, as stated ideally in (2.20), becomes

$$\mathbf{A}_0 = \mathbf{H}_0 \left(\boldsymbol{\mu} + \mathbf{b}\right) \mathbf{a},$$

where $\mathbf{b}$ is a diagonal matrix representing the additive noise that we assume to have zero mean. As a consequence, on the average we have the following:

$$E\{||\mathbf{A}_0 \mathrm{R}||^2\} = ||\mathbf{H}_0 \boldsymbol{\mu} \mathbf{a} \mathrm{R}||^2 + E\{||\mathbf{H}_0 \mathbf{b} \mathbf{a} \mathrm{R}||^2\}. \tag{2.21}$$

Given that the localization parameters are obtained by finding any non-trivial vector R of length $M+1$, such that $\mathbf{H}_0 \boldsymbol{\mu} \mathbf{a} \mathrm{R} = 0$, we see from the above expression that, in order to avoid a systematic bias due to the noise, it is advisable to solve the following minimization problem:

$$\min_{\mathrm{R} \in \mathbb{C}^{M+1}} ||\mathbf{A}_0 \mathrm{R}||^2 \quad \text{subject to} \quad E\{||\mathbf{H}_0 \mathbf{b} \mathbf{a} \mathrm{R}||^2\} = \text{Constant}. \tag{2.22}$$

This way, we actually minimize an expression that is close to $||\mathbf{H}_0 \boldsymbol{\mu} \mathbf{a} \mathrm{R}\|^2$, which would be the one that is set to zero in the noiseless annihilation problem. In order to perform the optimization (2.22), we need to set a hypothesis on the covariance matrix of the noise. If we assume this covariance to be $\sigma^2 \mathbf{Id}$ (white noise hypothesis), we have

$$\begin{aligned} E\{||\mathbf{H}_0 \mathbf{b} \mathbf{a} \mathrm{R}||^2\} &= E\{\mathrm{R}^\dagger \mathbf{a}^\dagger \mathbf{b}^\dagger \mathbf{H}_0^\dagger \mathbf{H}_0 \mathbf{b} \mathbf{a} \mathrm{R}\} \\ &= \sigma^2 \mathrm{R}^\dagger \mathbf{a}^\dagger \mathrm{diag}\{\mathbf{H}_0^\dagger \mathbf{H}_0\} \mathbf{a} \mathrm{R}, \end{aligned} \tag{2.23}$$

The variance σ^2 is completely determined by the Signal-to-Noise Ratio (SNR) of the generalized measures. Of course, in the absence of noise, (2.22) yields the exact position parameters.

2.4.3 Accuracy of the retrieval

To evaluate the performance of the proposed algorithm in the presence of noise, we compute the Cramér-Rao lower bounds (CRLBs) for the setting with the additive white Gaussian noise hypothesis [53]. Given noisy generalized measures, these bounds establish the minimal covariance matrix of any *unbiased* estimate of the position and intensity parameters.

The signal model describing the noisy generalized samples, $g(\mathbf{x}; a_n)$, is the following:

$$g(\boldsymbol{\theta}; a_n) = f(\boldsymbol{\theta}; a_n) + v_n + iw_n, \tag{2.24}$$

where we have defined

$$\begin{array}{c} f(\boldsymbol{\theta}; a_n) = \mu_n \quad \text{and} \quad \boldsymbol{\theta} = [\mathrm{Re}(\mathbf{z}), \mathrm{Im}(\mathbf{z}), \mathrm{Re}(\mathbf{c}), \mathrm{Im}(\mathbf{c})]^{\mathrm{T}} \\ \text{with } \mathbf{z} = [z_1, z_2, \ldots, z_M] \quad \text{and} \quad \mathbf{c} = [c_1, c_2, \ldots, c_M]. \end{array}$$

Moreover, v_n and w_n are independent normally distributed random variables with expected value 0 and variance σ^2.

In order to compute these lower bounds, we determine the Fisher information matrix, $\mathbf{J} = [J_{k,l}]_{k,l \in \{1 \cdots 2M\}}$, corresponding to (2.24), which reads as follows:

$$\mathbf{J} = \frac{1}{\sigma^2} \sum_{n=0}^{N-1} \left[\begin{array}{c} \nabla_{\boldsymbol{\theta}} \mathrm{Re}(f(\boldsymbol{\theta}; a_n)) \\ \nabla_{\boldsymbol{\theta}} \mathrm{Im}(f(\boldsymbol{\theta}; a_n)) \end{array} \right] \left[\begin{array}{c} \nabla_{\boldsymbol{\theta}} \mathrm{Re}(f(\boldsymbol{\theta}; a_n)) \\ \nabla_{\boldsymbol{\theta}} \mathrm{Im}(f(\boldsymbol{\theta}; a_n)) \end{array} \right]^{\mathrm{T}} \tag{2.25}$$

The Cramér-Rao bounds are the diagonal elements of $\mathbf{J}^{-1}$.

2.5 Results

2.5.1 Simulation

We performed simulations using radial unit dipoles. The localization is the most important aspect in many applications. Hence, when simulating, we only consider the estimation of the position parameters.

We compared the obtained localization errors with the theoretical lower bounds that we computed using (2.25) in function of the signal-to-noise ratio (SNR=$10 \log \frac{\sum_n \mu_n^2}{\sum_n |v_n + iw_n|^2}$). Figures 2.6, 2.7(a), 2.7(b) depict the setting, sample estimations and corresponding lower bounds.

We see that up to a certain SNR (around 15 dB) the algorithm performs well;i.e., it reaches the theoretical Cramér-Rao lower bound. We can thus say that the

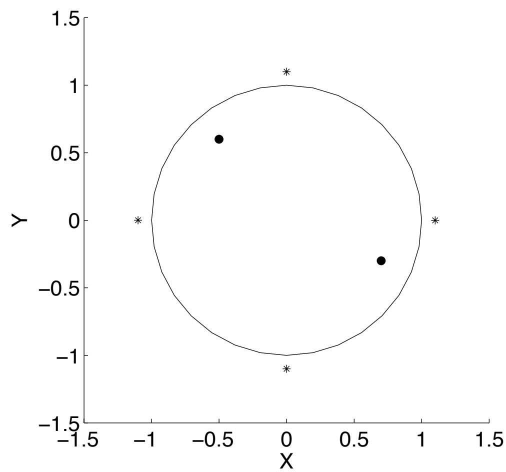

Figure 2.6: The source configuration with 2 point sources located at $(x_1, y_1) = (0.7, -0.3)$ and $(x_2, y_2) = (-0.5, 0.6)$. Moreover, the singularities of the analytic sensors, located at $1.1e^{in\frac{\pi}{2}}$ for $n \in \{0 \cdots 3\}$, are indicated as well.

Cramér-Rao bounds provide a good estimation of the performance of the localization. Further increasing the amount of noise increases the bound and the experimental estimation errors.

The number of analytic sensors is another parameter that influences the theoretical and the experimental errors. Figures 2.8(a) and 2.8(b) show the lower bounds for estimating x_i and y_i using 50 analytic sensors. Compared to Figs. 2.7(a) and 2.7(b), we note that the bounds are narrower and that the sample estimations are closer to the true values of the estimated parameters for lower SNRs.

Another factor that influences the theoretical minimal and experimental errors is the position of the dipole. Figures 2.9(a) and 2.9(b) show the sum of the Cramér-Rao bounds, plotted as a grey-scale intensity in the resulting image, when shifting a dipole through a unit-disk using a squared grid.

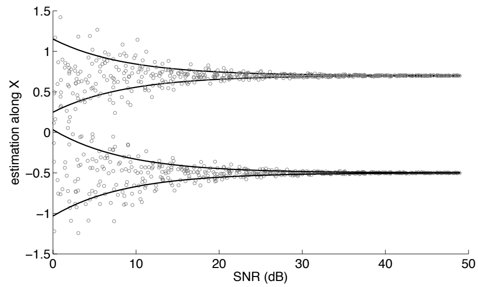

(a)

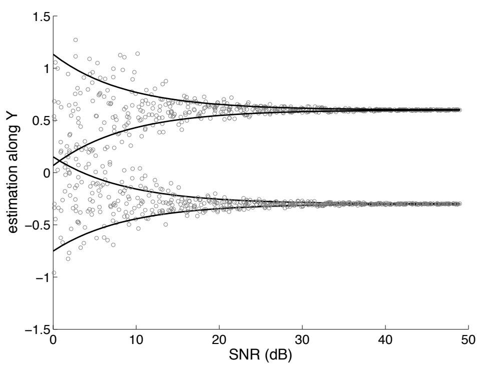

(b)

Figure 2.7: Figures 2.7(a) and 2.7(b) depict the lower bounds of any unbiased estimator (solid line) and some sample estimations (grey circles) obtained through our technique for respectively x_i and y_i with $i \in \{1, 2\}$. Moreover, we used the following 4 analytic sensors: $\psi_{a_n} = \ln\left(z - 1.1e^{i\frac{\pi}{2}n}\right)$, with $n \in \{0 \dots 3\}$.

Figure 2.9(a) clearly depicts the local influence of the analytic sensors. That is, the closer the dipole is located to a pole, a_n, the smaller the localization errors are. Thus, the analytic sensors properly sense the dipole's influence when the source and

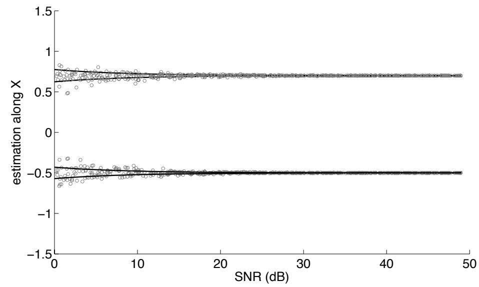

(a)

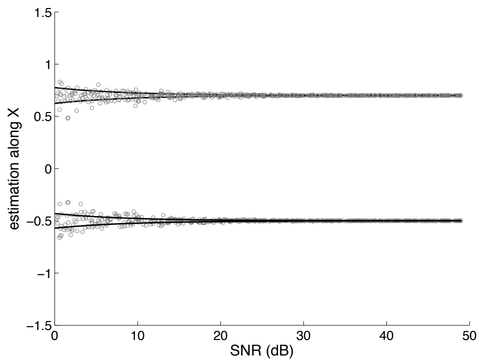

(b)

Figure 2.8: Figures 2.8(a) and 2.8(b) depict the lower bounds of any unbiased estimator (solid line) and some sample estimations (grey circles) obtained through our technique for respectively x_i and y_i with $i \in \{1, 2\}$ using the following 50 analytic sensors: $\psi_{a_n} = \ln\left(z - 1.1e^{i\frac{\pi}{25}n}\right)$, with $n \in \{0 \cdots 49\}$.

sink are close to any of the poles. Hence, when the dipole approaches the centre of the disk, the localization errors increase, as depicted in the Figs. 2.9(a) and 2.9(b). Moreover, when using more analytic sensors the estimation error decreases. This

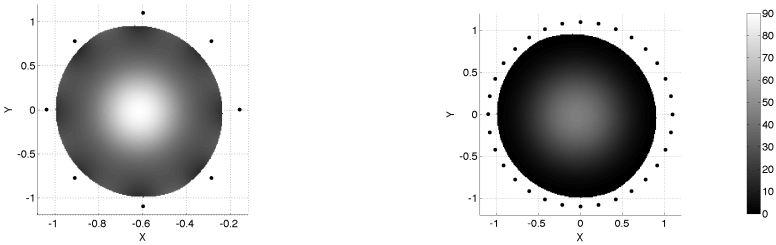

(a) (b)

Figure 2.9: Figures 2.9(a) and 2.9(b) depict the sum of the minimal estimation errors, indicated by the grey-scale intensity, when shifting a eccentric unit dipole through a unit-disk using a squared grid with step 0.01. The noise is Gaussian with expected value 0 and variance 0.06. The analytic sensors are respectively $\psi_{a_n} = \ln\left(z - 1.1 \cdot e^{in\frac{\pi}{4}}\right)$ with $n \in \{0 \cdots 7\}$ and $\psi'_{a_n} = \ln\left(z - 1.1 \cdot e^{in\frac{\pi}{16}}\right)$ with $n \in \{0 \cdots 31\}$.

is indicated by the fact that figure 2.9(b) is darker than figure 2.9(a).

Chapter 3

Extension to 3D

3.1 Summary

In the previous chapter we showed how to reconstruct the source ρ from the generated boundary potential in 2D. Here, we extend these techniques to 3D. In such, we obtain a direct algorithm to recover the generating source distribution from its induced boundary potential in a 3D setting.

We observe that the reconstruction technique obtained in the chapter 2 yields orthographic projections of the generating source ρ. We introduce a coordinate transform to obtain different projections of ρ on pre-defined planes. These projections are not properly partitioned which hinders the retrieval of the full 3D information. Hence, we devise a partitioning algorithm which is based on "Tomasi and Kanade's rank principle". Once the projections are properly partitioned we retrieve the 3D locations and moments of ρ in a classical way.

3.2 Motivation

The algorithm developed in chapter 2 uses an FRI framework which is a priori 2D. In such we cannot reconstruct the full 3D source distribution. However, most real-life problems that could benefit from analytic sensing are 3D problems, e.g., EEG or non-destructive testing applications such as crack detection [43, 51].

In this chapter we propose an extension of the reconstruction process described in chapter 2 to a 3D setting. We will show that we retrieve the orthographic projection of ρ. Hence, we introduce coordinate transforms which yield different projections of ρ from which the full 3D source distribution can be reconstructed.

The 2D projections of the locations $\mathbf{x}_m$ are the roots of a polynomial as described in chapter 2. Thus, the projections are not properly ordered. For example, if the first root of R represents the projection of $\mathbf{x}_1$ on the XY-plane then the first root of that same reconstruction process applied to the XZ-plane may be the projection of $\mathbf{x}_j$ for $j \neq 1$ and $M > 1$. The reconstruction algorithm described in [47] suffers from a similar problem. We develop a partitioning strategy based on Tomasi-Kanade's rank principle [54] that solves this problem and from which the full 3D source distribution can be reconstructed.

3.3 Sensing Principle in 3D

Let us start by writing out the generalized samples (2.2):

$$\langle \psi, \rho \rangle = -\int_{\partial\Omega} \sigma V \nabla \psi \cdot \mathbf{e}_\Omega \, \mathrm{d}s. \tag{3.1}$$

In a 3D setting, Ω represents a volume and $\partial\Omega$ the bounding surface. The computation of the generalized samples remain formally the same in a 3D setting, i.e., the RHS of (3.1) is a surface integral and not a line integral as stated in chapter 2. Figures 3.1(a) and 3.1(b) depict $||\nabla \ln{(z-a)}\,||$ for $a = 1.01$ and $a = 1.5$ on the unit sphere. We see that $||\nabla \ln{(z-a)}\,||$ is "well-localized" around a_n, which suggests that it is conceivable to compute an approximation of the integral 3.1 with only potential measures that are close to a_n.

3.4 Obtaining projections of the source distribution

Writing out $\langle \psi_{a_n}, \rho \rangle$ analytically yields

$$\langle \psi_{a_n}, \rho \rangle = \sum_{m=1}^{M} \frac{p_{x_m} + i p_{y_m}}{x_m + i y_m - a_n}.$$

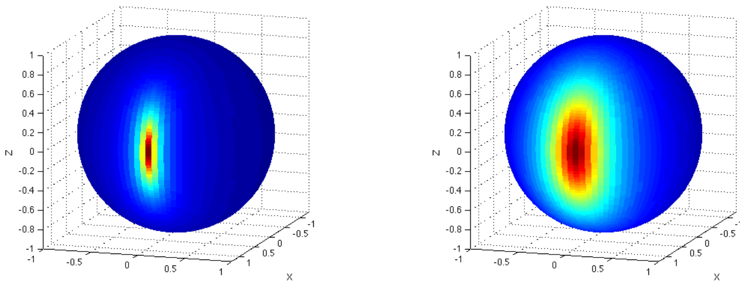

(a) (b)

Figure 3.1: Figure 3.1(a) and 3.1(b) depict $||\nabla \ln(x+iy-a)||$ on the unit sphere $\mathcal{S}$ for $a = 1.05$ and $a = 1.2$. Red indicates a high value of $||\nabla \ln(x+iy-a)||$ whereas blue indicates a relative small value.

A set of such generalized samples allows for the retrieval of $\{(x_m, y_m, p_{y_m}, p_{y_m})\}_{m=1\cdots M}$ as described in chapter 2. We observe that, $\{(x_m, y_m, p_{y_m}, p_{x_m})\}_{m=1\cdots M}$ characterizes the projection of ρ on the XY-plane. If we could obtain a projection of ρ on a different plane, say the XZ-plane, then we could fancy recovering the full 3D source distribution.

Consider the following coordinate transform:

$$\begin{bmatrix} x' \\ y' \\ z' \end{bmatrix} = \mathbf{R} \begin{bmatrix} x \\ y \\ z \end{bmatrix}, \tag{3.2}$$

with $\mathbf{R}$ some rotation matrix. If we apply the Sensing Principle with the proposed coordinate transform, then we obtain the generalized samples

$$\langle \psi_{a_n}, \rho \rangle = \sum_{m=1}^{M} \frac{p'_{x_m} + i p'_{y_m}}{x'_m + i y'_m - a_n}, \tag{3.3}$$

with

$$\begin{bmatrix} p'_{x_m} \\ p'_{y_m} \end{bmatrix} = \begin{bmatrix} 1 & 0 & 0 \\ 0 & 1 & 0 \end{bmatrix} \mathbf{R}\mathbf{p}_m,$$

and

$$\begin{bmatrix} x'_m \\ y'_m \end{bmatrix} = \begin{bmatrix} 1 & 0 & 0 \\ 0 & 1 & 0 \end{bmatrix} \mathbf{R}\mathbf{x}_m.$$

Applying the reconstruction algorithm proposed in chapter 2 on the generalized samples (3.3) yields $\{(x'_m, y'_m, p'_{x_m}, p'_{y_m})\}_{m=1\cdots M}$ which represents a projection of ρ on a plane specified by the rotation matrix $\mathbf{R}$. Figure 3.2 depicts this schematically. For example, if

$$\mathbf{R} = \begin{bmatrix} 1 & 0 & 0 \\ 0 & 0 & 1 \\ 0 & -1 & 0 \end{bmatrix},$$

then $\{(x'_m, y'_m, p'_{x_m}, p'_{y_m})\}_{m=1\cdots M} \Leftrightarrow \{(x_m, z_m, p_{x_m}, p_{z_m})\}_{m=1\cdots M}$ is a projection of ρ on the XZ-plane. Using multiple rotation matrices $\mathbf{R}_j$, $j = 1\cdots P$, in combination with the Sensing Principle and the proposed 2D reconstruction algorithm yields P projections of the M generating dipoles on different planes.

3.5 Partitioning problem

Consider a setting with 2 generating dipoles, $\rho = \sum_{m=1}^{2} \mathbf{p}_m \cdot \nabla\delta(\mathbf{x} - \mathbf{x}_m)$ and 3 rotation matrices, $\{\mathbf{R}_j\}_{j=1\cdots 3}$ that lead to 3 projection planes. Moreover, we are interested in the reconstruction of the location parameters $\mathbf{x}_m$ only (so we ignore the projections of the moments). In order to retrieve the 3D locations, we apply the reconstruction algorithm, depicted in figure 3.2 for each rotation matrix $\mathbf{R}_j$. This yields the projections:

Rotation matrix	*Obtained projections*
$\mathbf{R}^{(1)}$	$\left(x_1^{(1)}, y_1^{(1)}\right)$ and $\left(x_2^{(1)}, y_2^{(1)}\right)$
$\mathbf{R}^{(2)}$	$\left(x_2^{(2)}, y_2^{(2)}\right)$ and $\left(x_1^{(2)}, y_1^{(2)}\right)$
$\mathbf{R}^{(3)}$	$\left(x_2^{(3)}, y_2^{(3)}\right)$ and $\left(x_1^{(3)}, y_1^{(3)}\right)$

. (3.4)

We observe that we obtained first the projection of $\mathbf{x}_1$ and then the projection $\mathbf{x}_2$ for $\mathbf{R}^{(1)}$. However, for $\mathbf{R}^{(2)}$ and $\mathbf{R}^{(3)}$, we obtained first the projection of $\mathbf{x}_2$ and then the projection of $\mathbf{x}_1$. Hence, if we want to reconstruct the full 3D source information from the obtained projections, then we need an algorithm that decides

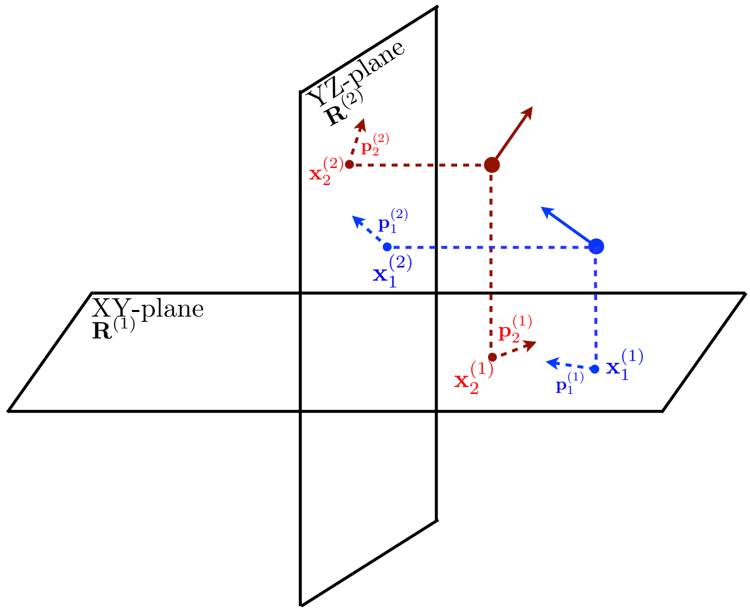

Figure 3.2: The orthographic projections (the projection lines are orthogonal to the planes on which the dipoles are projected) of 2 dipoles, $\mathbf{x}_1$ and $\mathbf{p}_1$ depicted by a blue dot and blue arrow and $\mathbf{x}_2$ and $\mathbf{p}_2$ indicated by a red dot and red arrow, on the XY-plane, specified by the rotation matrix $\mathbf{R}^{(1)}$ and the YZ-plane, specified by $\mathbf{R}^{(2)}$. The obtained projections are $\left[\mathbf{x}_1^{(1)}, \mathbf{p}_1^{(1)}\right]$ and $\left[\mathbf{x}_2^{(1)}, \mathbf{p}_2^{(1)}\right]$ on the XY-plane and $\left[\mathbf{x}_1^{(2)}, \mathbf{p}_1^{(2)}\right]$ and $\left[\mathbf{x}_2^{(2)}, \mathbf{p}_2^{(2)}\right]$ on the YZ-plane.

which projections belong to which dipole. Note that, if the projections are exact, then it is easy to decide which projections stem from the same dipole since $\mathbf{R}^{(j)}$ is known. However, in general, the projections can be distorted due to the influence of noise; e.g., the measurement noise at the electrode sites, which implies the need for an algorithm to establish the correspondence between the projections of different $\mathbf{R}^{(j)}$.

Let us start by writing the obtained projections in a matrix $\mathbf{L}$, called the observation matrix. Ideally $\mathbf{L}$ reads as follows:

$$\mathbf{L} = \begin{bmatrix} x_1^{(1)} & y_1^{(1)} & \cdots & x_1^{(P)} & y_1^{(P)} \\ x_2^{(1)} & y_2^{(1)} & \cdots & x_2^{(P)} & y_2^{(P)} \\ & & \vdots & & \\ x_M^{(1)} & y_M^{(1)} & \cdots & x_M^{(P)} & y_M^{(P)} \end{bmatrix} . \tag{3.5}$$

Theorem 3. *The rank of the observation matrix* $\mathbf{L}$*, as defined in (3.5), is at most* 3.

Proof. Consider the rotation matrix $\mathbf{R}^{(j)}$. We have that:

$$\begin{bmatrix} x_m^{(j)} \\ y_m^{(j)} \\ z_m^{(j)} \end{bmatrix} = \mathbf{R}^{(j)}\mathbf{x}_m,$$

for $j = 1 \cdots P$ and $m = 1 \cdots M$. Moreover, we define $\mathbf{x}^{(l)}, \mathbf{y}^{(l)}, \mathbf{z}^{(l)}$ as follows:

$$\begin{aligned} \mathbf{x}^{(l)} &= \left[x_1^{(l)} x_2^{(l)} \cdots x_M^{(l)}\right]^T \\ \mathbf{y}^{(l)} &= \left[y_1^{(l)} y_2^{(l)} \cdots y_M^{(l)}\right]^T \\ \mathbf{z}^{(l)} &= \left[z_1^{(l)} z_2^{(l)} \cdots z_M^{(l)}\right]^T \end{aligned} .$$

Since $\mathbf{R}_l$ is a rotation matrix, and hence unitary, we have that

$$\mathbf{A} = \mathbf{x}^{(l)}\mathbf{x}^{(l)^T} + \mathbf{y}^{(l)}\mathbf{y}^{(l)^T} + \mathbf{z}^{(l)}\mathbf{z}^{(l)^T} \tag{3.6}$$

is invariant for $l \in \{1 \cdots P\}$.Moreover, for any non-zero vector $\mathbf{u}$, $\mathrm{Rank}\left(\mathbf{u}\mathbf{u}^T\right) = 1$ holds and hence we have that

$$\mathrm{Rank}\left(\mathbf{A}\right) \leq 3. \tag{3.7}$$

By definition equation (3.7) states that any column of $\mathbf{A}$ can be written as a linear combination of 3 vectors $\mathbf{u}_1, \mathbf{u}_2$ and $\mathbf{u}_3$. Equation (3.6) states that the columns of $\mathbf{A}$ are linear combinations of $\mathbf{x}^{(l)}, \mathbf{y}^{(l)}$ and $\mathbf{z}^{(l)}$ for $l \in \{1 \cdots P\}$. Hence, $\mathbf{x}^{(l)}, \mathbf{y}^{(l)}$ and $\mathbf{z}^{(l)}$ can be written as linear combinations of $\mathbf{u}_1, \mathbf{u}_2$ and $\mathbf{u}_3$ for any $l \in \{1 \cdots P\}$ and hence we have that

$$\text{Rank}\,(\mathbf{L}) \leq 3,$$

with $\mathbf{L} = \left[\mathbf{x}^{(1)}\mathbf{y}^{(1)} \cdots \mathbf{x}^{(P)}\mathbf{y}^{(P)}\right]$, which concludes this proof. $\square$

This important property, theorem 3, is also known in computer vision as Tomasi and Kanade's rank principle [54]. However, if ρ consists of few dipoles, $M < 3$, then we clearly have that $\text{Rank}\,(L) < 3$. To guarantee that $\text{Rank}\,(L) = 3$, we add 3 distinct self-chosen points, called reference points, $\mathbf{r}, \mathbf{s}$ and $\mathbf{t}$:

$$\begin{aligned} \mathbf{r} &= [r_x\ r_y\ r_z]^T \\ \mathbf{s} &= [s_x\ s_y\ s_z]^T\ , \\ \mathbf{t} &= [t_x\ t_y\ t_z]^T \end{aligned}$$

which yields the observation matrix

$$\mathbf{L} = \begin{bmatrix} r_x^{(1)} & r_y^{(1)} & \cdots & r_x^{(P)} & r_y^{(P)} \\ s_x^{(1)} & s_y^{(1)} & \cdots & s_x^{(P)} & s_y^{(P)} \\ t_x^{(1)} & t_y^{(1)} & \cdots & t_x^{(P)} & t_y^{(P)} \\ x_1^{(1)} & y_1^{(1)} & \cdots & x_1^{(P)} & y_1^{(P)} \\ x_2^{(1)} & y_2^{(1)} & \cdots & x_2^{(P)} & y_2^{(P)} \\ & & \vdots & & \\ x_M^{(1)} & y_M^{(1)} & \cdots & x_M^{(P)} & y_M^{(P)} \end{bmatrix} \tag{3.8}$$

with $\text{Rank}\,(\mathbf{L}) = 3$.

Let us write the observation matrix, $\mathbf{L}'$, that corresponds to projections obtained in (3.4):

$$\mathbf{L}' = \begin{bmatrix} r_x^{(1)} & r_y^{(1)} & r_x^{(2)} & r_y^{(2)} & r_x^{(3)} & r_y^{(3)} \\ s_x^{(1)} & s_y^{(1)} & s_x^{(2)} & s_y^{(2)} & s_x^{(3)} & s_y^{(3)} \\ t_x^{(1)} & t_y^{(1)} & t_x^{(2)} & t_y^{(2)} & t_x^{(3)} & t_y^{(3)} \\ x_1^{(1)} & y_1^{(1)} & x_2^{(2)} & y_2^{(2)} & x_2^{(3))} & y_2^{(3)} \\ x_2^{(1)} & y_2^{(1)} & x_1^{(2)} & y_1^{(2)} & x_1^{(3))} & y_1^{(3)} \end{bmatrix}.$$

This matrix is of full rank, $\text{Rank}\,(\mathbf{L}') = 5$, since, e.g., $\left[(l')_{4,1}\,(l')_{4,2}\right]$ does not correspond to the projection of $\mathbf{x}_2$. Swapping $(l')_{4,1}$ and $(l')_{4,2}$ with $(l')_{5,1}$ and $(l')_{5,2}$ re-establishes the proper correspondence between the obtained projections and as a consequence the corresponding observation matrix has rank 3.

Generally speaking, if we do not have the proper correspondence between the obtained projections, then the observation matrix $\mathbf{L}'$ has full rank, $\text{Rank}\,(\mathbf{L}') = \min\,(3 + M, 2P)$. A brute force approach to establishing the correspondence between the projections consists of permuting the elements in a column until the resulting observation matrix has rank 3. The first 3 lines remain unaltered since the correspondence between the projections of the reference points is known since we chose them ourselves. The permutation that yields $\mathbf{L}$ such that $\text{Rank}\,(L) = 3$ yields the correct correspondence between the obtained projections. Note, that the number of possible observation matrices, $\mathcal{O}$, grows extremely rapidly in M and P, i.e., $\mathcal{O} = (M!)^{P-1}$.

3.5.1 Influence of noise

In reality, the projections $x_m^{(i)}$ are subject to noise, i.e., instead of $x_m^{(i)}$ we obtain $\tilde{x}_m^{(i)} = x_m^{(i)} + \varepsilon$ and hence the *ideal* realistic observation matrix $\tilde{\mathbf{L}}$ is

$$\tilde{\mathbf{L}} = \begin{bmatrix} r_x^{(1)} & r_y^{(1)} & \cdots & r_x^{(P)} & r_y^{(P)} \\ s_x^{(1)} & s_y^{(1)} & \cdots & s_x^{(P)} & s_y^{(P)} \\ t_x^{(1)} & t_y^{(1)} & \cdots & t_x^{(P)} & t_y^{(P)} \\ \tilde{x}_1^{(1)} & \tilde{y}_1^{(1)} & \cdots & \tilde{x}_1^{(P)} & \tilde{y}_1^{(P)} \\ \tilde{x}_2^{(1)} & \tilde{y}_2^{(1)} & \cdots & \tilde{x}_2^{(P)} & \tilde{y}_2^{(P)} \\ & & \vdots & & \\ \tilde{x}_M^{(1)} & \tilde{y}_M^{(1)} & \cdots & \tilde{x}_M^{(P)} & \tilde{y}_M^{(P)} \end{bmatrix}.$$

Due to the noise, $\tilde{\mathbf{L}}$ has full rank. However, for any possible observation matrix $\tilde{\mathbf{L}}'$ we have that $\tilde{\sigma}'_4 > \tilde{\sigma}_4$ with $\tilde{\sigma}'_4$ and $\tilde{\sigma}_4$ the 4^{th} singular values of $\tilde{\mathbf{L}}'$ and $\tilde{\mathbf{L}}$. As a consequence, establishing the correspondence between the obtained distorted projections boils down to finding that observation matrix $\tilde{\mathbf{L}}'$ which has the smallest $\tilde{\sigma}'_{4,4}$.

3.6 Recovering the full 3D information

Assume that we know the proper correspondence between the obtained projections; if we do not know the proper correspondence then we apply the algorithm described above to obtain the observation matrix

$$\mathbf{L} = \begin{bmatrix} \mathbf{v}_x^{(1)} & \mathbf{v}_y^{(1)} & \cdots & \mathbf{v}_x^{(P)} & \mathbf{v}_y^{(P)} \\ \mathbf{x}^{(1)} & \mathbf{y}^{(1)} & \cdots & \mathbf{x}^{(P)} & \mathbf{y}^{(P)} \end{bmatrix}, \tag{3.9}$$

where $\mathbf{v}_x^{(l)} = \left[r_x^{(l)} \; s_x^{(l)} \; t_x^{(l)} \right]^T$ and $\mathbf{v}_y^{(l)} = \left[r_y^{(l)} \; s_y^{(l)} \; t_y^{(l)} \right]^T$. This is the same matrix as in (3.8) but with a more concise notation. The singular value decomposition of $\mathbf{L}$ can be written as

$$\begin{aligned} \mathbf{L} &= \mathbf{USV}^T \\ &= [\mathbf{U}' \; \mathbf{U}_0] \begin{bmatrix} \mathbf{S}' \\ \mathbf{0} \end{bmatrix} \mathbf{V}^T \; . \end{aligned} \tag{3.10}$$

Since Rank $(\mathbf{L}) = 3$, $\mathbf{L}$ has only 3 non-zero singular values which are grouped in the block $\mathbf{S}'$. So $\mathbf{U}_0$ are the left singular vectors corresponding to the singular values $\sigma_i = 0$ of $\mathbf{L}$. In such we have that

$$\mathbf{U}_0^T L = 0. \tag{3.11}$$

Let us write down $\mathbf{U}_0$ as a block matrix where the first 3 lines are grouped in $\mathbf{u}_0$ and the remaining M lines in $\mathbf{u}_0'$:

$$\mathbf{U}_0 = \begin{bmatrix} \mathbf{u}_0 \\ \mathbf{u}_0' \end{bmatrix}, \tag{3.12}$$

If we use the expressions (3.9) for $\mathbf{L}$ and (3.12) for $\mathbf{u}_0$ in (3.11), then we obtain

$$\begin{bmatrix} \mathbf{u}_0^T \mathbf{v}_x^{(1)} + \mathbf{u}_0' \mathbf{x}^{(1)} & \mathbf{u}_0^T \mathbf{v}_y^{(1)} + \mathbf{u}_0' \mathbf{y}^{(1)} & \cdots & \mathbf{u}_0^T \mathbf{v}_y^{(P)} + \mathbf{u}_0' \mathbf{y}^{(P)} \end{bmatrix} = \mathbf{0},$$

from which

$$\begin{aligned} \mathbf{x}^{(l)} &= -\left(\mathbf{u}_0'\right)^{-1} \left(\mathbf{u}_0^T \mathbf{v}_x^{(l)} \right) \\ \mathbf{y}^{(l)} &= -\left(\mathbf{u}_0'\right)^{-1} \left(\mathbf{u}_0^T \mathbf{v}_y^{(l)} \right) \end{aligned} \; .$$

Furthermore, because of the invariance (3.6), we have that

$$\begin{array}{rcl} \mathbf{x} & = & [r_x\ s_x\ t_x\ x_1\ \cdots\ x_M]^T \\ \mathbf{y} & = & [r_y\ s_y\ t_y\ y_1\ \cdots\ y_M]^T \\ \mathbf{z} & = & [r_z\ s_z\ t_z\ z_1\ \cdots\ z_M]^T \end{array} ,$$

belong to the same space spanned by the columns of $\mathbf{L}$. As a consequence, when adding $\mathbf{x}, \mathbf{y}$ and $\mathbf{z}$ as columns to $\mathbf{L}$ the matrix $\mathbf{U}$ in the singular value decomposition (3.10) remains the same and as a consequence we have that

$$\begin{array}{rcl} [x_1\ \cdots\ x_M]^T & = & -(\mathbf{u}_0')^{-1}\left(\mathbf{u}_0^T\,[r_x\ s_x\ t_x]^T\right) \\ [y_1\ \cdots\ y_M]^T & = & -(\mathbf{u}_0')^{-1}\left(\mathbf{u}_0^T\,[r_y\ s_y\ t_y]^T\right) \\ [z_1\ \cdots\ z_M]^T & = & -(\mathbf{u}_0')^{-1}\left(\mathbf{u}_0^T\,[r_z\ s_z\ t_z]^T\right) \end{array} ,$$

which define the full 3D locations $\mathbf{x}_m$. Note that theoretically only 2 projections of $\mathbf{x}_m$ suffice to reconstruct the full 3D source distribution. In the presence of noise more projections of $\mathbf{x}_m$ allow for a more "proper" estimation of $\mathbf{U}$.

Exactly the same reasoning can be adopted to obtain the dipoles' moments $\mathbf{p}_m$. However, the generated boundary potential depends linearly on the moments (a direct consequence of the governing equation 1.1). Hence, if we know the dipoles' locations then we can infer the dipoles' moments directly from the measurements by solving a linear system of equations.

3.6.1 Alternative analytic sensor for 3D reconstruction

In [43] it has been noted that if ψ is a valid test function, in their case a polynomial of $x + iy$, then the test function $z\psi$ is a good candidate to reconstruct 3D sources. In our case ψ is the analytic sensor $\ln(x + iy - a)$ and since $\psi_a' = z \ln(x + iy - a)$ is a valid analytic sensor as well it might be fruitful to attempt a 3D reconstruction. Indeed, we have

$$\begin{array}{rcl} \mu_n' & = & < \psi_a', \rho > \\ & = & \sum_{m=1}^{M} \frac{(p_{x_m} + i p_{y_m}) z_m + \ln(x_m + i y_m - a_n) p_{z_m}}{x_m + i y_m - a_n} \end{array} . \tag{3.13}$$

Since we can obtain x_m and y_m (and p_{x_m} and p_{y_m}) by the method explained above, we can reconstruct z_m and p_{z_m} by solving (3.13), which is a linear system of equations in the unknown components z_m and p_{z_m} for $m = 1 \cdots M$. However, $|\nabla \psi'_a|$ is not localized around a and hence, the computation of μ'_a according to (2.2) might be imprecise; especially in applications where only a finite set of measures is taken on the boundary $\partial\Omega$ (as is the case in EEG).

3.6.2 Comparison with the state-of-the-art

We describe briefly how the method developed in [47] handles 3D settings. This method uses meromorphic approximations to deduce the generating sources' locations. A meromorphic function is intrinsically 2D (it is defined in the complex plane). To extend this method to 3D the method is applied iteratively on the intersections of Ω with parallel planes at different z-coordinates. At each iteration only a 2D boundary is considered, as depicted in figure 3.3, so the full 3D configuration of the measures is not exploited. The source projections with highest eccentricity in the plane determine the z-components.

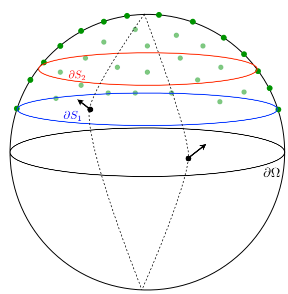

Figure 3.3: A spherical domain with boundary $\partial\Omega$ and three generating dipoles, depicted by the 3 arrows. The green dots on the surface represent the measure sites. The reconstruction method described in [47] uses 2D boundaries such as ∂S_1 and ∂S_2 to retrieve ρ.

Chapter 4

Intermediate Recapitulation and Outlook

4.1 Recapitulation

The inverse EEG problem, $\mathcal{P}$,tries to reconstruct the source distribution, ρ, responsible for the measured potential differences, V_i. A set of electrodes are placed on the scalp that measure the potential field generated by ρ. Unfortunately, there is no unique solution to $\mathcal{P}$; which is why $\mathcal{P}$ is ill-posed. To render the solution to $\mathcal{P}$ unique we parameterized ρ; i.e., we assumed that ρ is a superposition of M dipoles

$$\rho = \sum_{m=1}^{M} \mathbf{p}_m \cdot \nabla\delta\left(\mathbf{x} - \mathbf{x}_m\right)$$

In such, the boundary potential $V\big|_{\partial\Omega}$ uniquely defines $\{\mathbf{x}_m, \mathbf{p}_m\}_{m=1\cdots M}$.

We introduced the sensing principle in chapter 2. This is a method to obtain a measure on ρ, knowing only the boundary potential $V\big|_{\partial\Omega}$. These measures, called generalized samples, are obtained by applying the sensing principle with well-chosen test functions, ψ for which

$$\operatorname{div}\left(\sigma\nabla\psi\right) = 0$$

holds. In that case the generalized samples are

$$\langle \psi, \rho \rangle = \oint_{\partial\Omega} V \nabla \psi \cdot \mathbf{e}_{\Omega} ds.$$

In order to select a favourable test function or device a reconstruction algorithm we need supplementary restrictions on σ. We assumed

$$\begin{array}{rcll} \sigma(x, y, z) & = & \text{constant} & \text{for } (x, y, z) \in \Omega \\ \sigma(x, y, z) & = & 0 & \text{for } (x, y, z) \notin \Omega \end{array}.$$

Because of this assumption, any valid test function is Ω-harmonic

$$\Delta\psi\big|_{\Omega} = 0.$$

A large subset of such Ω-harmonic functions are analytic in Ω. We have called such viable analytic test function “analytic sensors”.

Among all analytic sensors we have chosen

$$\psi_a \quad = \quad \ln(x + iy - a) \quad \text{with } a \notin \Omega \ ,$$

since it allows for a direct and analytic reconstruction algorithm (this algorithm is inspired from the FRI setting and is devised in chapter 2). We chose a set of such analytic sensors $\{\psi_{a_n}\}_{n=0\cdots N-1}$ such that the corresponding generalized samples, $\{\mu_n\}_{n=0\cdots N-1}$, have a particular structure common to FRI-problems. That is, the x- and y-coordinates of the generating sources are obtained as the roots of a polynomial R which is unknown. However, the special choice of the singularities a_n allow for the construction of a filter h such that

$$h \star (\mu_n \mathrm{R}) = 0;$$

h is called an annihilating filter. We showed that this is in fact a linear system of equations in the unknown coefficients r_k of R.

This reconstruction algorithm is intrinsically 2D. Since real-life applications are usually 3D, such as EEG, we needed to extend this reconstruction scheme to 3D. The sensing principle extends readably to 3D, i.e., formally nothing changes, the 2D domain becomes a 3D volume with bounding surface $\partial\Omega$ in which ρ lies. Hence, the sensing principle now requires the computation of a 3D surface integral instead of a 2D contour integral. Next, we observed that we reconstruct an orthographic projection of ρ. By introducing various coordinate transforms we obtained different 2D projections of ρ from which we reconstructed te full 3D source distribution. Chapter 3 unravels the technical difficulties involved; e.g., since the projections are roots of a polynomial R they are not ordered and hence we need a way to order the obtained projection (this is done using Tomasi and Kanade's rank principle).

Figure 4.1 depicts a flowchart of the reconstruction scheme we have.

4.2 Outlook

Although the bulk of the reconstruction algorithm has been developed we still need to fill in some blanks.

If we want our reconstruction algorithm to be applicable in real-life applications, then we need it to be able to cope with non-homogeneous conductor models. For example, in EEG the human head is often modeled as a 3-sphere conductor model where the layers represent the brain, skull and scalp. Each layer has its own characteristic, and often isotropic, conductivity. In that case σ is a piecewise constant function of $r = \sqrt{x^2 + y^2 + z^2}$. Another example is the earth, which is often modelled as a 5-sphere conductor model (the layers represent the earth's inner core, outer core, mantle, upper mantle and crust). A change of σ only influences the construction of the analytic sensor ψ_a. In the next chapter (chapter 5) we construct such an analytic sensor, ψ_a, for varying σ, with a particular interest in piecewise constant conductor profiles.

As depicted in figure 4.1 the reconstruction process needs to compute integrals of the form $\mu = \oint_{\partial\Omega} V \nabla \psi_a \cdot \mathbf{e}_\Omega ds$, with ψ_a some viable analytic sensor. In practice V is not continuously known on the boundary; i.e., V is measured at 32,64,128 or 204 electrode sites on the surface. In order to apply the sensing principle we need to construct a continuous representation of $V\big|_{\partial\Omega}$ from a discrete set of measures. In this manuscript we work with spherical conductor models (although the proposed framework is not restricted to spherical models) and hence spherical harmonics are a viable option to interpolate/approximate the measured data. Moreover, spherical harmonics facilitate the computation of the generalized samples considerably. This interpolation/approximation scheme is explained in chapter 6.

Note that, the model for ρ is an approximation of what happens in reality. In such we need a model matching algorithm that matches the data to our model. That is, we need an algorithm that makes minimal changes to the computed generalized measures such that the constructed filter h annihilates μR. For this, we adapt Cadzow's iterative denoising algorithm. This iterative scheme is a sequence of a subspace decomposition followed by a dimensionality reduction and a subspace projection iterated until the filter h can annihilate the generalized samples. This denoising method is elaborated in chapter 6.

In chapter 7, we investigate the precision, resolution and noise robustness of the proposed reconstruction algorithm by means of simulations. Finally, we treat real data of a visual evoked potential and compare our results to the results of LAURA.

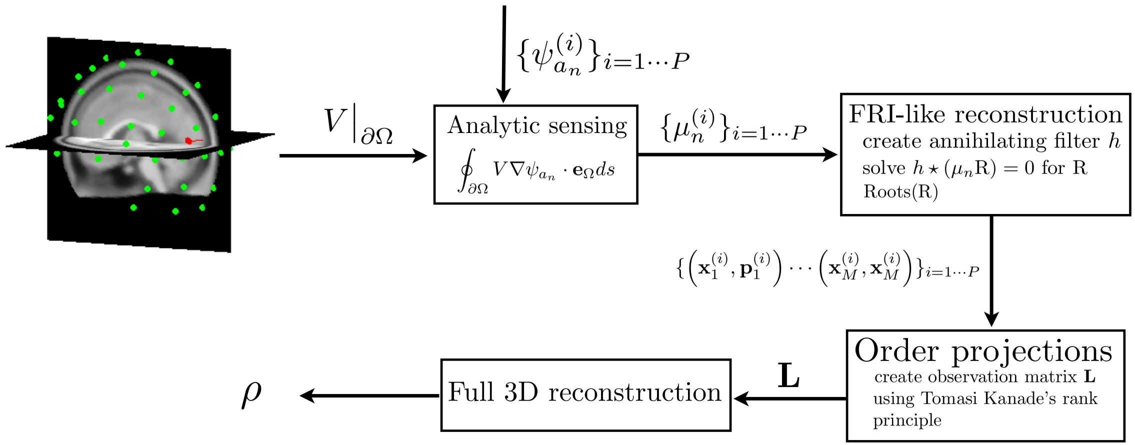

Figure 4.1: Here we see a flowchart of the proposed reconstruction scheme. Each block corresponds to an important part described above. First we see an IRM image of the human brain with a generating dipole; the green dots represent the electrode sites (EEG setting and background on the generated signal are described in chapter 1). The next functional block represents the sensing principle, which transforms the boundary potential in a set of generalized measurements (presented in chapter 2). Then, we see the reconstruction algorithm, that applies a FRI-like scheme to obtain projections of generating sources (described in chapter 2 and chapter 3). Then we see how these projections are ordered using Tomasi and Kanade's rank principle (demonstrated in chapter 3). This produces an observation matrix $\mathbf{L}$. Finally the obtained observation matrix is used to reconstruct the 3D source distribution ρ (explained in chapter 3).

Chapter 5

Multi-Layer Spherical Conductivity Models

This chapter is largely based on the article entitled "*Analytic Sensing for Multi-Layer Spherical Models with Application to Source Imaging*, submitted to *Inverse Problems.*

5.1 Summary

Until now we assumed that Ω is a homogeneous conductor model. This severely hinders the practical use of our reconstruction algorithm.

In this chapter we show how to construct analytic sensors that go with inhomogeneous conductor models. The derivation assumes that σ is a scalar function of $r = \sqrt{x^2 + y^2 + z^2}$. Constructing such test functions boils down to solving a set of 3D differential equations. In particular, we show how to solve these differential equations in the case of layered spherical conductor models by creating explicitly an analytic sensor for the 3-sphere conductor model.

5.2 Motivation

Analytic sensing takes advantage of Green's (also called the divergence) theorem to compute the scalar products $\langle\psi,\rho\rangle$, knowing only $V\big|_{\partial\Omega}$. These scalar products μ can be seen as "generalized samples" of the unknown distribution, which serve to reconstruct ρ, and are computed using the following boundary integral:

$$\langle\psi,\rho\rangle = -\oint_{\partial\Omega} \sigma V \nabla\psi \cdot \mathbf{e}_{\Omega} ds. \tag{5.1}$$

These analytic sensors ψ satisfy the key property:

$$\mathrm{div}(\sigma\nabla\psi) = 0, \tag{5.2}$$

which ensures that the generalized samples can be computed as stated in (5.1).

Previously (in chapter 2), the conductor model was supposed to be homogeneous: σ was a constant and (5.2) reverts to the Laplace equation, $\Delta\psi = 0$, which is satisfied by analytic functions of the variable $\zeta = x + iy$[1]. In many application, including EEG, spherical multi-layer conductor models are often useful [52]. Moreover, the changes in conductivity of the outer layers can highly impact the localization error [55, 56]. Therefore, the assumption of homogeneity hinders the practical use of the original approach of analytic sensing. We extend the original framework such that it can cope with a N-sphere conductor model. Figures 5.1(a) and 5.1(b) depict a 3-sphere conductor model with isotropic (scalar) conductivities.

There are 2 ways to overcome the limitations imposed by a homogeneous conductor model:

- We propagate the measured boundary potential inward, that is, down to the boundary of the inner compartment [57]. Although this propagation takes into account the inhomogeneity of the conductor model, it propagates the noisy measures. More precisely, propagating the noisy boundary measurements inward amplifies the noise and consequently the propagated boundary potential is likely to be of low quality.
- We construct new analytic sensors that propagate outward up to the outer boundary of the conductor model. Since the analytic sensor is known analyti-

[1] To avoid any confusion in this chapter, we denote the complex unit by ζ, $\zeta = x + iy$

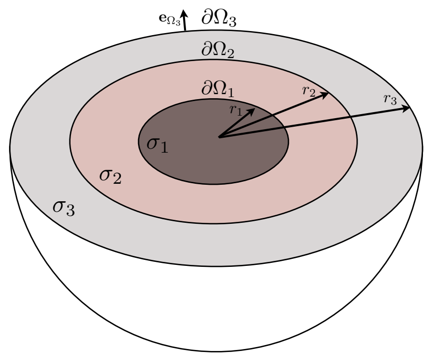

(a)

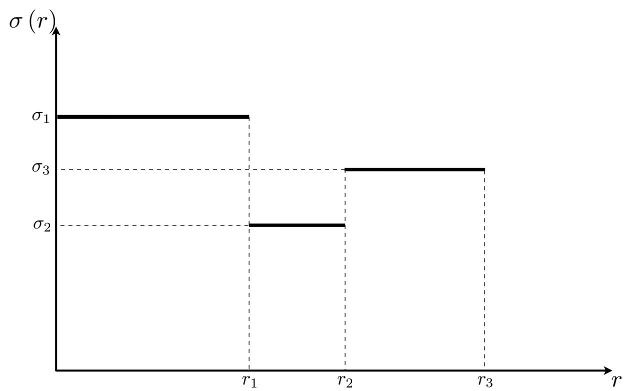

(b)

Figure 5.1: Figure 5.1(a) depicts a 3-sphere conductor model. Each compartment, Ω_i, has its own characteristic conductivity, σ_i for $i \in \{1, \cdots, 3\}$. Figure 5.1(b) depicts the corresponding conductivity profile as a function of r (which is in this case a piecewise constant). Each discontinuity represents a boundary $\partial\Omega_1$, $\partial\Omega_2$ or $\partial\Omega_3$.

cally, this propagation is exact and not sensitive to noisy boundary measures. This is the approach that we will pursue here.

Constructing such test functions boils down to solving a set of 3D differential equations, that express the physical constraints of the conductor model. We show how these equations can be solved using a particular separation of variables, hence, creating a new set of analytic sensors that account for layers of different constant conductivity (e.g., the skull is often modeled as a spherical layer of low conductivity between two or more spherical layers of high conductivity). We show, explicitly, how to construct analytic sensors for the 3-sphere model. These analytic sensors enable the usage of the reconstruction algorithm in combination with the 3-sphere conductor model as such.

5.3 Extending the sensing principle for spherical head models

5.3.1 Particular solutions of the continuity equation with radial conductivity

The desired form of the analytic sensor in the inner compartment Ω_1, where the sources are located, is a desired function of ζ that allows to retrieve the sources subsequently. We will show that, because σ varies radially, a separation of variables in ζ and r reduces (5.2) to solving two decoupled differential equations.

Lemma 2. *If we assume that σ varies radially and is $\mathcal{C}^1$ in some ring, then all analytic sensors ψ that satisfy*

$$\operatorname{div}(\sigma \nabla \psi) = 0$$

in that ring, and that can be put under the separable form

$$\psi(x, y, z) = \psi_0(\zeta)\psi_1(r),$$

where $\zeta = x + iy$ and $r = \sqrt{x^2 + y^2 + z^2}$, are solutions of the differential equations:

$$\zeta \psi_0'(\zeta) - n\psi_0(\zeta) = 0, \tag{5.3}$$

$$r\psi_1''(r) + \left(2(n+1) + \frac{r\sigma'}{\sigma}\right)\psi_1(r) + n\frac{\sigma'}{\sigma}\psi_1(r) = 0, \tag{5.4}$$

where n is some scalar.

Proof. We look for a special solution taking the separable form:

$$\psi(x,y,z) = \psi_0(\zeta)\psi_1(r),$$

with $\zeta = x + iy$ and $\Delta\psi_0 = 0$.

Then, (5.2) takes the form:

$$\sigma' \mathbf{u}_r^T \nabla\psi + \sigma\Delta\psi = 0, \tag{5.5}$$

where $\mathbf{u}_r$ is the vector defined as

$$\mathbf{u}_r = \frac{1}{r}\begin{pmatrix} x \\ y \\ z \end{pmatrix}^T.$$

The first term of (5.5) can be further rewritten as:

$$\begin{aligned} \mathbf{u}_r^T \nabla\psi &= \psi_1 \mathbf{u}_r^T \nabla\psi_0 \mathbf{u}_r^T \nabla\psi_1 \\ &= \psi_1(r)\psi_0'(\zeta)\frac{\zeta}{r} + \psi_0(\zeta)\psi_1'(r), \end{aligned}$$

and second term as:

$$\begin{aligned} \Delta\psi &= \psi_0(\zeta)\Delta\psi_1(r) + 2\nabla\psi_0(\zeta)^T\nabla\psi_1(r) + \psi_1\Delta\psi_0(\zeta) \\ &= \psi_0(\zeta)\frac{r\psi_1''(r) + 2\psi_1'(r)}{r} + 2\psi_0'(\zeta)\psi_1'(r)\frac{\zeta}{r}. \end{aligned}$$

Consequently (5.5) becomes

$$\underbrace{\sigma'(r)\psi_1(r)\psi_0(\zeta)\frac{\zeta}{r} + \sigma'(r)\psi_0(\zeta)\psi_1'(rs)}_{\sigma' \mathbf{u}_r^T \nabla\psi} + \underbrace{\sigma(r)\psi_0(\zeta)\frac{r\psi_1''(r) + 2\psi_1'(r)}{r} + 2\sigma(r)\psi_0'\psi_1'(r)\frac{\zeta}{r}}_{\sigma\Delta\psi} = 0,$$

which can be separated into two parts, one that depends only on ζ, and another that depends only on r:

$$\frac{\zeta\psi_0'(\zeta)}{\psi_0(\zeta)} = -\frac{r\sigma'(r)\psi_1'(r) + \sigma(r)\left(r\psi_1''(r) + 2\psi_1'(r)\right)}{\sigma'(r)\psi_1(r) + 2\sigma(r)\psi_1'(r)}. \tag{5.6}$$

The left-hand side (lhs) of (5.6) is a function of ζ whereas the right-hand side (rhs) is a function of r. These variables are independent which implies that lhs = rhs = Constant. This results into two decoupled differential equations:

$$\zeta\psi_0'(\zeta) - n\psi_0(\zeta) = 0,$$
$$r\psi_1''(r) + \left(2(n+1) + \frac{r\sigma'}{\sigma}\right)\psi_1'(r) + n\frac{\sigma'}{\sigma}\psi_1(r) = 0,$$

which concludes the proof. □

The solution of (5.3) is $\psi_0 = \text{Constant}\times\zeta^n$ which is discontinuous or multivalued if $n \notin \mathbb{N}$. Hence we require n to be some integer. Thus, if ψ_1 is a function for which

$$r\psi_1''(r) + \left(2(n+1) + \frac{r\sigma'}{\sigma}\right)\psi_1'(r) + n\frac{\sigma'}{\sigma}\psi_1(r) = 0, \tag{5.7}$$

holds, then

$$\psi(x,y,z) = (x+iy)^n\psi_1(r), \quad n \in \mathbb{N}$$

is a valid test function.

Taking into account the N-sphere conductivity model, we have that in each region with constant σ

$$\psi(x,y,z) = C(x+iy)^n + C'\frac{(x+iy)^n}{r^{2n+1}},$$

with C and C' arbitrary constants. This means that, due to the linearity of the operator $\operatorname{div}(\sigma\nabla\cdot)$, any valid analytic sensor ψ, in a region where σ = Constant, must be of the form

$$\psi(x,y,z) = \varphi(x+iy) + \frac{1}{r}\Phi\left(\frac{x+iy}{r^2}\right),$$

where φ and Φ are entire functions. In order to fully characterize the analytic sensors that go with an N-sphere conductivity model, we need to describe the behavior (or rather change) of ψ at a boundary $\partial\Omega_i$.

Proposition 1. *If we know φ and Φ in a ring $\Omega_j = \{\mathbf{x} \in \mathbb{R}^3,\ s.t.\ r_{j-1} \leq \|\mathbf{x}\| \leq r_j\}$ of an N-sphere $(j = 1, 2, \dots N)$ conductivity model*

$$\begin{aligned} \varphi &= \varphi_j \quad \textit{in } \Omega_j \\ \Phi &= \Phi_j \quad \textit{in } \Omega_j \\ \sigma &= \sigma_j \quad \textit{in } \Omega_j \end{aligned}$$

then we can propagate φ_j and Φ_j through $\partial\Omega_j = \Omega_j \cap \Omega_{j+1}$, by solving the following two differential equations:

$$\frac{2\zeta}{r_j^3}\Phi'_{j+1}\left(\frac{\zeta}{r_j^2}\right) + \frac{1}{r_j}\Phi_{j+1}\left(\frac{\zeta}{r_j^2}\right) = -g_j(\zeta) + \zeta f'_j(\zeta), \tag{5.8}$$

$$\varphi_{j+1} = f_j(\zeta) - \frac{1}{r_j}\Phi_{j+1}\left(\frac{\zeta}{r_j^2}\right), \tag{5.9}$$

where

$$f_j(\zeta) = \varphi_j(\zeta) + \frac{1}{r_j}\Phi_j\left(\frac{\zeta}{r_j^2}\right), \tag{5.10}$$

$$g_j(\zeta) = \frac{\sigma_j}{\sigma_{j+1}}\left(\zeta\varphi'_j(\zeta) - \frac{1}{r_j}\Phi_j\left(\frac{\zeta}{r_j^2}\right) - \frac{\zeta}{r_j^3}\Phi'_j\left(\frac{\zeta}{r_j^2}\right)\right). \tag{5.11}$$

Proof. Using standard arguments frequent in electromagnetic physics, or using distribution theory, it is possible to show that, if σ and ψ are piecewise $\mathcal{C}^1$ satisfying $\operatorname{div}(\sigma\nabla\psi) = 0$ separately in the interiors of Ω_j and Ω_{j+1}, then

$$\left.\begin{array}{r} \psi \\ \sigma\mathbf{x}^T\nabla\psi \end{array}\right\} \text{are continuous across } \partial\Omega_j \quad \Longrightarrow \quad \operatorname{div}(\sigma\nabla\psi) = 0 \text{ in } \Omega_j \cup \Omega_{j+1}$$

- for the continuity of ψ at $\partial\Omega_j$

$$\varphi_j(\zeta) + \frac{1}{r_j}\Phi_j\left(\frac{\zeta}{r_j^2}\right) = \varphi_{j+1}(\zeta) + \frac{1}{r_j}\Phi_{j+1}\left(\frac{\zeta}{r_j^2}\right); \tag{5.12}$$

- for the continuity of $\sigma \mathbf{x}^T \nabla \psi$ at $\partial\Omega_j$

$$\begin{aligned} \sigma_j \quad & \left((\zeta)\varphi_j'(\zeta) - \frac{1}{r_j}\Phi_j\left(\frac{\zeta}{r_j^2}\right) - \frac{\zeta}{r_j^3}\Phi_j'\left(\frac{\zeta}{r_j^2}\right)\right) = \\ & \sigma_{j+1}\left((\zeta)\varphi_{j+1}'(\zeta) - \frac{1}{r_j}\Phi_{j+1}\left(\frac{\zeta}{r_j^2}\right) - \frac{\zeta}{r_j^3}\Phi_{j+1}'\left(\frac{\zeta}{r_j^2}\right)\right), \end{aligned} \tag{5.13}$$

for any ζ such that $||\zeta|| \leq r_j$. These two differential equations, (5.12) and (5.13), describe how a test function ψ changes (or rather propagates) over such a boundary $\partial\Omega_j$. In what follows we show how to find φ_{j+1} and Φ_{j+1} from φ_j and Φ_j. This describes explicitly how the test function ψ propagates over a discontinuity of σ.

Let us define $f_j(\zeta)$ and $g_j(\zeta)$ to be:

$$f_j(\zeta) = \varphi_j(\zeta) + \frac{1}{r_j}\Phi_j\left(\frac{\zeta}{r_j^2}\right),$$

$$g_j(\zeta) = \frac{\sigma_j}{\sigma_{j+1}}\left(\zeta\varphi_j'(\zeta) - \frac{1}{r_j}\Phi_j\left(\frac{\zeta}{r_j^2}(\right) - \frac{\zeta}{r_j^3}\Phi_{j-1}'\left(\frac{\zeta}{r_j^2}\right)\right),$$

then the equations (5.12) and (5.13) read:

$$\begin{cases} \varphi_{j+1}(\zeta) + \dfrac{1}{r_j}\Phi_{j+1}\left(\dfrac{\zeta}{r_j^2}\right) = f_j(\zeta), \\ \zeta\varphi_{j+1}' - \dfrac{1}{r_j}\Phi_{j+1}\left(\dfrac{\zeta}{r_j^2}\right) - \dfrac{\zeta}{r_j^3}\Phi_{j+1}'\left(\dfrac{\zeta}{r_j^2}\right) = g_j(\zeta). \end{cases} \tag{5.14}$$

By elimination of φ_{j+1} in (5.14), we obtain an ordinary differential equation (ODE) for Φ_{j+1}:

$$\frac{2\zeta}{r_j^3}\Phi_{j+1}'\left(\frac{\zeta}{r_j^2}\right) + \frac{1}{r_j}\Phi_{j+1}\left(\frac{\zeta}{r_j^2}\right) = -g_j(\zeta) + \zeta f_j'(\zeta).$$

Once the above ODE is solved, and thus Φ_{j+1} is known, we can find φ_{j+1} by solving the first equation of (5.14) for φ_{j+1}:

$$\varphi_{j+1} = f_j(\zeta) - \frac{1}{r_j}\Phi_{j+1}\left(\frac{\zeta}{r_j^2}\right),$$

which concludes this proof. □

So, if we choose φ_0 and Φ_0, we can construct $\psi\big|_{\partial\Omega}$ by (repeated) propagation of φ_j and Φ_j through the boundaries $\partial\Omega_j$ until we reach the outer boundary. Note that the ODE that defines Φ_{j+1} can be integrated exactly.

5.3.2 Example: spherical head model with multiple layers

An important head model in EEG applications is the 3-sphere conductor model $\mathcal{S}$ depicted in figure 5.1. Each compartment Ω_1, Ω_2 and Ω_3, with their respective conductivities σ_1, σ_2 and σ_3, represents a specific tissue class. In the case of the 2-layered sphere the compartments represent the brain, skull and scalp, respectively. It is generally accepted that the brain and scalp tissue have a comparable conductivity ($\sigma_1 = \sigma_3$), whereas the skull has a much lower conductivity (e.g., $\frac{\sigma_1}{\sigma_2} = 80$). Such a compartment with low conductivity attenuates and smooths the generated boundary potential $V\big|_{\partial\Omega}$. Figure 5.2 demonstrates this attenuation and blurring due to the layer Ω_2 with low conductivity.

If ρ is a superposition of dipoles, then reconstructing ρ from the measured EEG, using the reconstruction algorithm described in the previous chapters, requires new analytic sensors ψ that behave as $\log(\zeta - a)$ in Ω_1, with $a \notin \mathcal{S}$, and that take into account the conductivity profile of $\mathcal{S}$. Hence, we need to propagate $\ln(\zeta - a)$ through the outer boundaries $\partial\Omega_1$, $\partial\Omega_2$ of the compartments Ω_1 and Ω_2. Appendices A.1 and A.2 show the propagations of $\ln(\zeta - a)$ through $\partial\Omega_1$ and $\partial\Omega_2$ which yield the required analytic sensors ψ_a.

5.4 Demonstration

We want to show the importance and the feasibility of the analytic sensors that take into account the conductivity profile of the conductor model.

We computed the potential generated by 100 unit dipoles (with outward moment), located in the XY-plane, in 204 electrodes on the "spherical model with anatomic constrains" (SMAC) head model. The SMAC model is a way to combine the computational ease of spherical conductor models, i.e., a 3-sphere conductor model (which is currently used in the hospital of Geneva), with the precision of realistic head models [52].

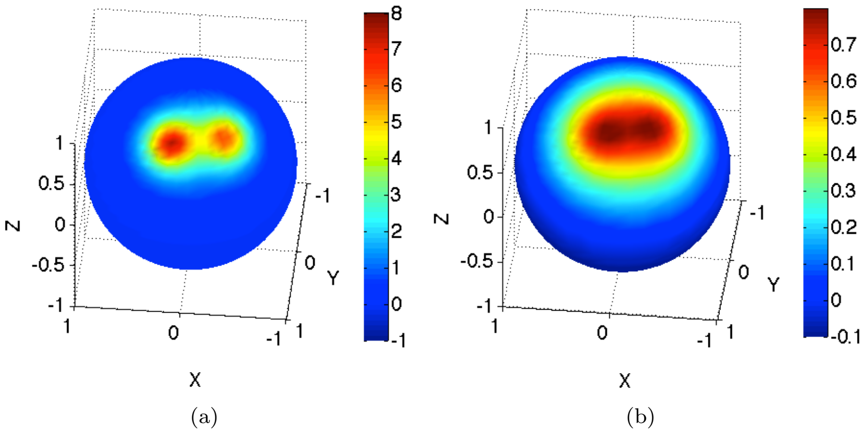

Figure 5.2: Figure 5.2(a) shows $V\big|_{\partial\Omega}$ generated by a source distribution ρ in a homogeneous ($\sigma = 1$) sphere whereas figure 5.2(b) shows $V\big|_{\partial\Omega_3}$ generated by the same source distribution in a 3-sphere conductor model. The compartments represent the brain (characterized by a radius $r_1 = 0.86$ and a conductivity $\sigma_1 = 1$), the skull ($r_2 = 0.92$ and $\sigma_2 = 0.0125$) and the scalp ($r_3 = 1$ and $\sigma_3 = 1$). The source distribution is a sum of 2 dipoles located at $\mathbf{x_1} = [0.1\ 0.5\ 0.6]^T$, $\mathbf{x_2} = [-0.3\ 0.4\ 0.6]^T$ and with moments $\mathbf{p_1} = \frac{\mathbf{x_1}}{||\mathbf{x_1}||}$ and $\mathbf{p_2} = \frac{\mathbf{x_2}}{||\mathbf{x_2}||}$.

For the conductor model, a 3-sphere conductor model, we have $r_1 = 0.86, r_2 = 0.92, r_3 = 1$ and $\sigma_1 = 1, \sigma_2 = 0.0125, \sigma_3 = 1$, which are common in an EEG setting. We used 32 analytic sensors $\{\psi_{a_n}\}_{n=0\cdots 31}$ with singularities $a_n = 1.1\exp(i\frac{2\pi}{32}n)$. This setting, the SMAC conductor model, the electrode configuration and the singularities are depicted in figure 5.4. The analytic sensors use the correct boundary radii, $r_1 = 0.86, r_2 = 0.92$ and conductivities $\sigma_1 = 1$ and $\sigma_3 = 1$. We varied the conductivity σ_2 taken into account by the analytic sensors. For each variation of σ_2 we computed $\langle\psi_{a_n}, \rho\rangle$ and performed a localization using the FRI-approach described above.

Varying σ_2 in the analytic sensors introduces a model mismatch between the

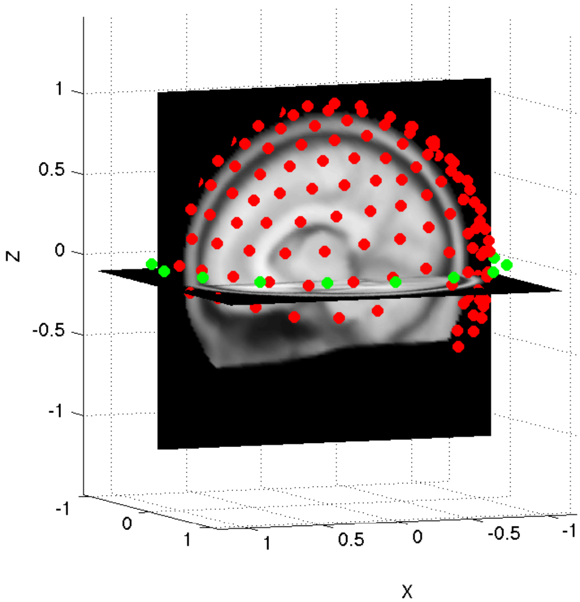

Figure 5.3: The setting used to perform the simulations. Here we see the SMAC head model, which is a 3-sphere conductor model fitted to an averaged head. The red dots represent the electrodes and the green dots represent the singularities of the analytic sensors.

conductivity profile used to generate the boundary potential and the conductivity profile taken into account by the analytic sensors which in turn influences the localization error. Figures 5.4(a) and 5.4(b) depict the effect of a varying σ_2, taken into account by the analytic sensors, on the localization error. We see that the localization error is minimal if there is no model mismatch between the conductivity profile used to generate the boundary potential and the conductivity profile taken into account by the analytic sensors. Hence, in our case, the localization error is minimal if we construct ψ_{a_n} such that it accounts for $\sigma_1 = 1, \sigma_2 = 0.0125$ and $\sigma_3 = 1$.

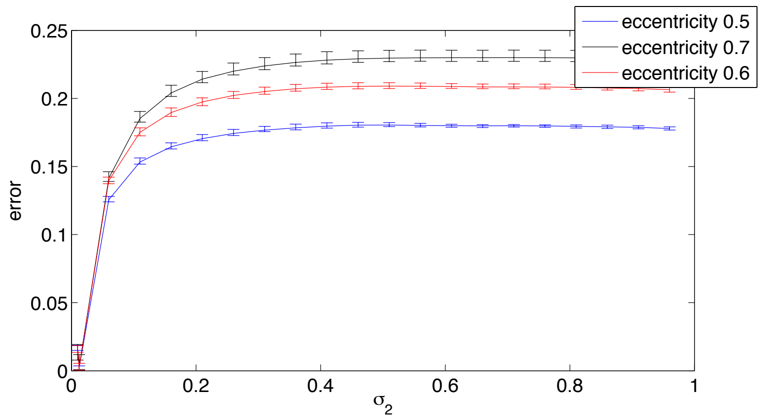

(a)

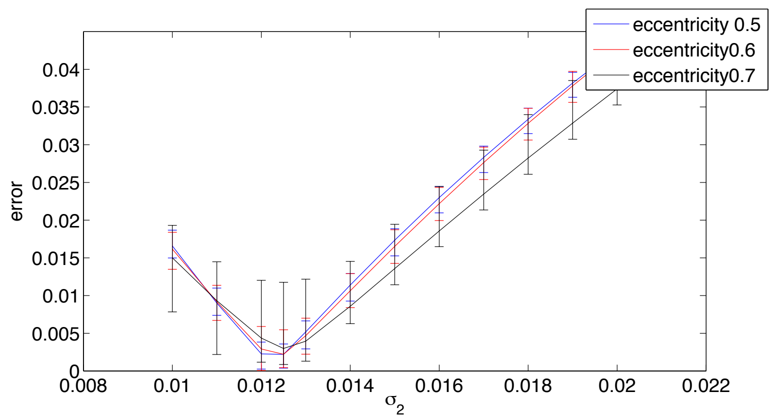

(b)

Figure 5.4: Figures 5.4(a) and 5.4(b) show the mean localization error in function of the model mismatch between the conductivity profile taken into account by the analytic sensors and the conductivity profile used to generate the boundary potential. Furthermore, the maximum and minimum localization error is depicted by means of error bars. The boundary potential is generated by unit dipoles at different eccentricities (indicated by the colours of the curves) with outward moments and measured in 204 electrodes on $\partial\Omega_3$.

Chapter 6

Approximation Error and Model Mismatch

6.1 Summary

The computation of the generalized samples requires a continuous representation of $V\big|_{\partial\Omega}$. However, in practice we only have access to a finite number of noisy measurements on the boundary, $\tilde{V}_i$.

In this chapter we devise an approximation scheme based on spherical harmonics to obtain such a continuous domain presentation of V on the boundary, $\tilde{V}\big|_{\partial\Omega}$. Moreover, this interpolation scheme allows for a fast computation of the corresponding generalized measures $\tilde{\mu}$.

These generalized samples are noisy because of the approximation error and the noisy potential measurements. To compensate for the erroneous generalized samples, we adapt Cadzow's iterative denoising scheme [58, 49]. In such we end up with a model matching algorithm that adjusts the generalized samples such that they serve to reconstruct the source distribution ρ according to the reconstruction procedure described in chapter 2.

6.2 Motivation

Until now we assumed that $V\big|_{\partial\Omega}$ is continuously known on the boundary. However, in practice the $V\big|_{\partial\Omega}$ is sampled in a finite number of points; e.g., in EEG the generated boundary potential is measured in, typically, 32, 64 up to 204 electrodes.

The sensing principle requires a continuous representation of the boundary potential, $V\big|_{\partial\Omega}$, to obtain a measure μ_n of the source distribution. In such we need an approximation of $V\big|_{\partial\Omega}$ based on the noisy measured potentials $\tilde{V}_i$. Moreover, the proposed approximation should allow for an efficient computation of the corresponding generalized samples $\tilde{\mu}_n$.

Since the generated boundary potential, $V\big|_{\partial\Omega}$, is square integrable we opt for spherical harmonics to approximate $V\big|_{\partial\Omega}$. Furthermore, we see that this yields an efficient way to compute the generalized samples. The obtained generalized samples $\tilde{\mu}_n$ are obviously noisy (since we cannot recover $V\big|_{\partial\Omega}$ perfectly) and hence, we cannot apply the reconstruction algorithm described in chapter 2 as such (since $\tilde{\mu}_n \neq \mu_n$). In other words, the computed generalized samples cannot be annihilated by a filter h. We adapt Cadzow's iterative denoising algorithm [58, 49] to fit the computed generalized samples to the annihilation scheme; i.e., $\tilde{\mu}_n$ is altered with the smallest value possible such that (2.19) has a non-trivial solution. Note that, this *denoising* scheme is in fact a model matching technique.

6.3 A continuous representation of the boundary potential

Let us first consider the noiseless case; i.e., the boundary measurements, V_i with $i = 1 \cdots N$, are supposed to be ideal. In practice we often have 32, 64 or 128 boundary measures. Although, in EEG, high-density electrode caps that yield 204 measures exist. As stated in chapter 5, spherical conductor models are often used to represent the human head, and we will continue to do so as well. We assume a spherical conductor model with radius R=1.

Since $V\big|_{\partial\Omega}$ is square integrable; i.e., $\int\limits_{\partial\Omega} |V(\mathbf{x})|^2 d\mathbf{x} < \infty$, $V\big|_{\partial\Omega}$ can be written as a sum of spherical harmonics

$$V\big|_{\partial\Omega}(\theta,\phi) = \sum_{l=-\infty}^{+\infty} \sum_{m=-l}^{+l} c_{l,m} Y_l^m(\theta,\phi), \tag{6.1}$$

with Y_l^m a spherical harmonic of degree l and order m

$$\begin{cases} Y_l^m(\theta,\phi) &= P_l^m(\cos(\theta))\exp(jm\phi) \quad \text{for} \quad m \geq 0, \\ Y_l^m(\theta,\phi) &= (-1)^m \left(Y_l^{|m|}(\theta,\phi)\right)^\star \quad \text{for} \quad m < 0, \end{cases}$$

where $\star$ indicates the complex conjugation, P_l^m the normalized associated Legendre polynomial of degree l and order m and θ and ϕ are the elevation and azimuth angles of any point on the surface of the sphere. An approximation of the boundary potential, $\tilde{V}\big|_{\partial\Omega}$, is obtained by truncating the expansion (6.1)

$$\tilde{V}\big|_{\partial\Omega}(\theta,\phi) = \sum_{l=0}^{L} \sum_{m=-l}^{l} c_{l,m} Y_l^m(\theta,\phi). \tag{6.2}$$

Let us first illustrate what can go wrong when fitting N boundary measurements on the upper hemisphere with N spherical harmonics. For example, assume N=64 and a boundary potential generated by one radial unit dipole located at $\mathbf{x}_1 = [0\ 0\ 0.7]$ (as depicted in figure 6.3). Intuitively we want to construct an approximation $\tilde{V}\big|_{\partial\Omega}$ using 64 basis functions, i.e., we choose L=7 in (6.2) and solve the linear system of equations

$$\sum_{l=0}^{7} \sum_{m=-l}^{l} c_{l,m} Y_l^m(\theta_i,\phi_i) = V_i,$$

for the unknown coefficients $c_{l,m}$ with V_i the i^{th} measurement and $i = 1 \cdots 64$. Figure 6.2(a) plots $\tilde{V}\big|_{\partial\Omega}$ on the boundary of the conductor model. We see that $\tilde{V}\big|_{\partial\Omega}$ is not a good approximation of $V\big|_{\partial\Omega}$ because $\tilde{V}\big|_{\partial\Omega}$ has a huge energy in the lower hemisphere where we do not have any potential measures. Figure 6.3 depicts this phenomena. Generally speaking, if potential measures on the entire boundary are available, then the truncated expansion (6.2) properly represents $V\big|_{\partial\Omega}$. However, if the measures do not cover the entire boundary $\partial\Omega$, as is often

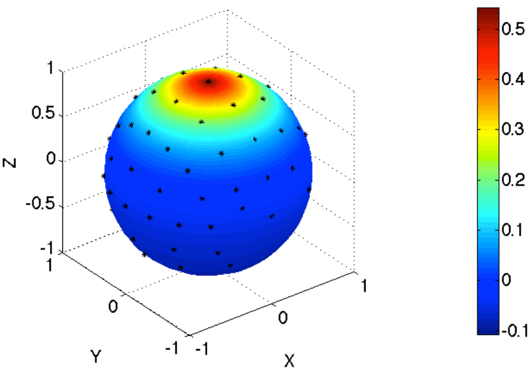

Figure 6.1: A unit sphere with the boundary potential generated by a radial unit dipole located at $\mathbf{x}_1 = [0\ 0\ 0.7]^T$. Red depicts a high value of $V\big|_{\partial\Omega}$ whereas blue depicts a relative low value. The boundary potential is measured in 64 points depicted by black stars.

the case, then a direct fit of (6.2) to the measurements yields a bad approximation.

In order to overcome this shortcoming we "pretend" to have full coverage of the boundary. The expansion (6.2) is chosen such there is a basis function per measure. For example, if we have only measures available on the upper hemisphere then we choose L in (6.2) such that there are roughly twice as much basis functions then available boundary measures. The coefficients $c_{l,m}$ are then obtained trough the minimization

$$\min_{\mathbf{C}} ||\mathbf{\Delta C}||^2 \quad \text{subject to} \quad ||\mathbf{SC} - \mathbf{V}||^2 \le \sigma, \tag{6.3}$$

with $\mathbf{C}$ a vector containing the coefficients $c_{l,m}$, $\mathbf{\Delta}$ a matrix representing some regularization criterion, $\mathbf{S}$ the system matrix relating the spherical harmonics to the measurements $\mathbf{V}$

$$\mathbf{S} = \begin{bmatrix} Y_0^0(\theta_1, \phi_1) & \cdots & Y_L^L(\theta_1, \phi_1) \\ & \vdots & \\ Y_0^0(\theta_N, \phi_N) & \cdots & Y_L^L(\theta_N, \phi_N) \end{bmatrix}$$

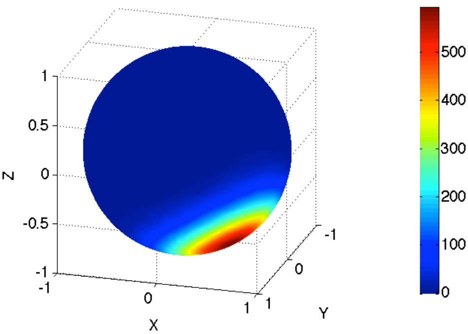

(a)

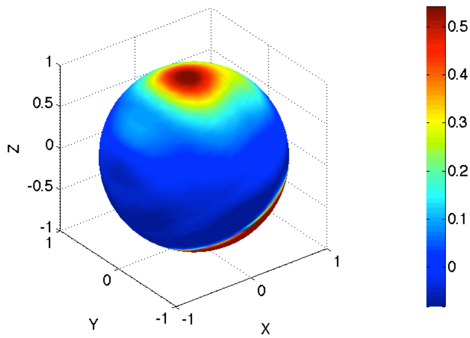

(b)

Figure 6.2: 6.2(a) The reconstructed boundary potential, $\tilde{V}\big|_{\partial\Omega}$, if spherical harmonics are used to directly fit the measured boundary potential (L=7). 6.2(b) The same reconstructed boundary potential but the area where no measures are available is clipped (the part colored in brown). We see that the expansion (6.2) is a reasonable approximating of $V\big|_{\partial\Omega}$ where we have potential measurements.

and σ a value that is determined by the noise level. Often the boundary potential, as is the case in EEG, varies slowly and hence we want to penalize high frequency components in the construction of (6.2); i.e., the coefficients $c_{l,m}$ corresponding to high values of l and m should be penalized. In such we opted for the following regularization:

$$\mathbf{\Delta} = \begin{bmatrix} 0 & & & & \\ & \ddots & & & \\ & & l^2 + m^2 & & \\ & & & \ddots & \\ & & & & L^2 + L^2 \end{bmatrix}. \tag{6.4}$$

Let us revisit the example given above (the setting depicted in figure 6.3) with the method proposed in 6.3 and regularization criterion 6.4. Since there is no noise on the potential measures we look for an interpolating solution ($\sigma = 0$). As stated

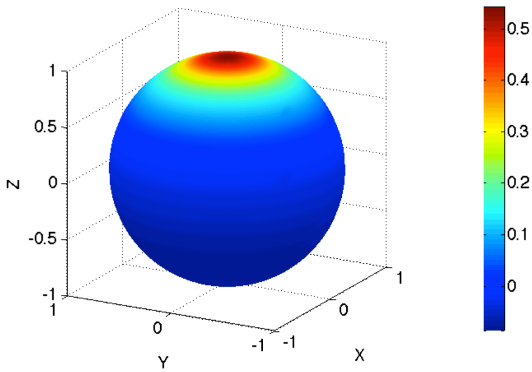

Figure 6.3: The reconstructed boundary potential using the minimization stated in (6.3) and the regularization criterion (6.4).

before we need to choose L in 6.2 such that we have, say, roughly twice as much basis functions as potential measures. We choose $L = 10$. Figure 6.3 shows the obtained approximation, which is obviously a better approximation of $V\big|_{\partial\Omega}$ than the approximation depicted in figure 6.3.

Note that, many other interpolation or approximation techniques for data measured on a sphere exist. For an extensive overview on interpolation or approximation techniques on the sphere we refer to [59]. Contrary to spherical harmonics, most other interpolation or approximation techniques; e.g., thin plate smoothing splines, do not allow for an efficient computation of the corresponding generalized samples. However, these methods often can handle the presence of noise better than the technique described in (6.3). In such we could denoise the noisy potential measures first; e.g., using a variational approach [60] or a state-of-the-art technique such as "SURE-LET" [61], and subsequently interpolate the denoised measures using the scheme described above.

6.3.1 A note on the computation of the generalized samples

One advantage of approximating $V\big|_{\partial\Omega}$ with spherical harmonics is the computational ease of the corresponding generalized samples $\tilde{\mu}$

$$\tilde{\mu} = -\sigma_3 \int_{\theta=0}^{\pi} \int_{\phi=0}^{2\pi} \underbrace{\sum_{l=0}^{L} \sum_{m=-l}^{l} c_{l,m} Y_l^m(\theta,\phi)}_{\tilde{V}\big|_{\partial\Omega}} \frac{\partial}{\partial r}\psi_a \sin(\theta)\ d\theta d\phi, \tag{6.5}$$

with ψ_a the analytic sensor corresponding to a 3-sphere conductor model with outer radius $R = 1$. This analytic sensor can be expressed as a power series in $\zeta = r\sin\theta \exp(j\phi)$ (as shown in appendix A.2). Deriving this power series with respect to r yields

$$\frac{\partial}{\partial r}\psi_a\big|_{r=R} = \sum_{k\geq 1} b_k \left(\sin(\theta)\exp(j\phi)\right)^k, \tag{6.6}$$

If we plug the expression (6.6) in (6.5) and apply Cauchy's integral theorem, then we deduce

$$\begin{aligned}
\tilde{\mu} &= -\sigma_3 \sum_{k\geq 1} b_k \sum_{l=0}^{L}\sum_{m=-l}^{l} c_{l,m} \int_0^{\pi} P_l^m(\cos(\theta))\sin^{k+1}(\theta)\ d\theta \int_0^{2\pi} \exp(j(k+m)\phi)\ d\phi, \\
&= -\sigma_3 \sum_{k\geq 1} b_k \sum_{l=0}^{L}\sum_{m=-l}^{l} c_{l,m} \left(\int_0^{\pi} P_l^m(\cos(\theta))\sin^{k+1}(\theta)\ d\theta\right) 2\pi\delta[m+k],
\end{aligned}$$

which after some simplification yields

$$\tilde{\mu} = -2\pi\sigma_3 \sum_{k=1}^{L} b_k \sum_{l=1}^{L}\sum_{m=-l}^{-1} c_{l,m} \int_0^{\pi} P_l^m(\cos(\theta))\sin^{k+1}(\theta)\ d\theta. \tag{6.7}$$

The integral in the RHS of (6.7) can be computed off-line and stored in a table. In such, the computation of the generalized samples (6.7) boils down to a sum of precomputed coefficients which is extremely fast.

6.4 Noise issues and model mismatch

A well-known problem in EEG is the low quality of the measured signal, i.e., the potential measures are corrupted by noise such that the measured signal is of low SNR. A second problem is that the dipolar model is an oversimplification of the true underlying source distribution. That is, although there are only M predominant dipoles; e.g., in special cases of epilepsy, there are a lot of other dipoles, albeit with low intensities, that contribute to the measured signal. This implies that we need to compensate for two sources of imprecision, **measurement noise** and **model mismatch**, which both contribute to the total "noise".

As we have seen in chapters 2 and 3, the 2D projections of the 3D locations $\mathbf{x}_m$ are the roots of some polynomial R. Since the roots of a polynomial depend in a non-linear way on its coefficients, obtaining the 2D projections of $\mathbf{x}_m$ may become unreliable in the presence of noise and hence, it is advisable to apply a robust denoising scheme. As shown in chapter 2, the coefficients of R are found by solving the linear system of equations

$$\underbrace{\mathbf{H_0}\tilde{\boldsymbol{\mu}}\mathbf{a}}_{\tilde{\mathbf{A}}} R = 0, \tag{6.8}$$

where $\mathbf{H_0}$ is a known $(N-M)\times N$ convolution matrix, $\tilde{\boldsymbol{\mu}}$ is a $N \times N$ diagonal matrix containing the computed generalized samples, $\mathbf{a}$ is a $N \times (M+1)$ Vandermonde matrix depending on the singularities a_n of the analytic sensors ψ_{a_n} and R is a vector representing the coefficients of the polynomial R(x) whose roots are 2D projections of $\mathbf{x}_m$. Note that, the matrix $\tilde{\mathbf{A}}$ might be ill-conditioned if the angular distance θ between the singularities $a_n = \alpha_n e^{in\theta}$ is small. Manipulating $\tilde{\mathbf{A}}$ as such might cause problems. In such, we replace $\mathbf{a}$ by a unitary matrix $\mathbf{a_0}$ obtained through the SVD of $\mathbf{a}$, $\mathbf{a} = \mathbf{a_0}\mathbf{S}\mathbf{V}^{\star}$. The resulting system matrix $\tilde{\mathbf{A}}$ that we will use for denoising is

$$\tilde{\mathbf{A}} = \mathbf{H_0}\tilde{\boldsymbol{\mu}}\mathbf{a_0}.$$

A fundamental observation is that in an ideal setting for any $L > M$ the resulting matrix $\mathbf{A}$ remains of rank M, which implies that the last $L - M$ singular values of $\mathbf{A}$ should be zero. However, if $\boldsymbol{\mu}$ is distorted, due to noise and model mismatch, then the corresponding matrix $\tilde{\mathbf{A}}$ is of full-rank. In such, $R = \mathbf{0}$ is the only viable solution, which is not satisfactory.

We adapt an iterative scheme, studied in [49], to denoise the generalized measures in a consistent way.The idea consists in performing a Singular Value Decomposition (SVD) of $\tilde{\mathbf{A}}$, $\tilde{\mathbf{A}} = \mathbf{U}\mathbf{S}\mathbf{V}^\star$, and forcing to zero the $L-M$ smallest diagonal elements of $\mathbf{S}$ to yield $\mathbf{S}'$. Such an operation is also called dimensionality reduction. Next, we perform a subspace projection by reconstructing a matrix $\mathbf{A}' = \mathbf{U}\mathbf{S}'\mathbf{V}^\star$. However, this matrix cannot be factorized as $\mathbf{A}' = \mathbf{H_0}\tilde{\boldsymbol{\mu}}\mathbf{a_0}$ but

$$\tilde{\boldsymbol{\mu}} = \underset{\boldsymbol{\mu}}{\operatorname{argmin}} ||\mathbf{H_0}\boldsymbol{\mu}\mathbf{a_0} - \boldsymbol{A'}||_{\mathrm{F}}, \tag{6.9}$$

yields the new measurement matrix $\tilde{\boldsymbol{\mu}}$ such that $\mathbf{H_0}\tilde{\boldsymbol{\mu}}\mathbf{a_0}$ is close to $\mathbf{A}'$ (with respect to the Frobenius norm, $||\cdot||_{\mathrm{F}}$). The minimization (6.9) is solved using a least squares fit. We iterate the scheme described above until we obtain a $\tilde{\boldsymbol{\mu}}$ such that the last $L-M$ singular values of $\mathbf{H_0}\tilde{\boldsymbol{\mu}}\mathbf{a_0}$ are smaller than a given threshold τ; e.g., $\tau = 10^{-5}$. Finally, the coefficients R are obtained by solving (6.8) using the denoised measurement matrix $\tilde{\mu}$. Figure 6.4 depicts this iterative denoising algorithm schematically.

To illustrate the effectiveness of the denoising scheme we consider a 2D setting with a unit radial dipole located at $\mathbf{x}_1 = [-0.5\ 0.7]^T$ and a set of analytic sensors with singularities $a_n = 1.01 \exp\left(in\frac{\pi}{64}\right)$ and $n = 32 \cdots 64$. Next, we added Gaussian noise to the generalized samples and performed a localization with analytic sensing. Figure 6.4 plots the localization error in function of the noise level using Cadzow's denoising scheme (solid red line) and without denoising (solid green line). We observe a smaller localization error when using the denoising scheme described above.

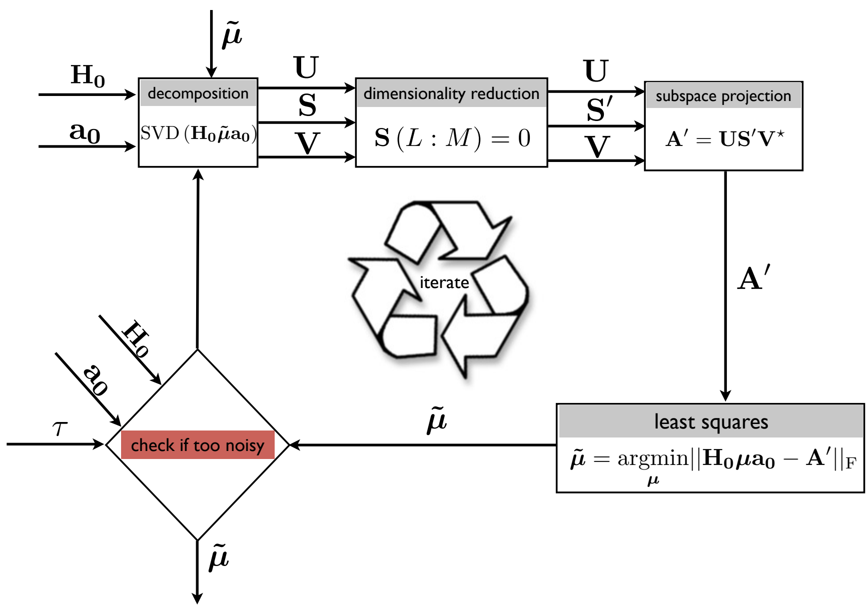

Figure 6.4: Cadzow's denoising algorithm adapted to our dipole localization problem. The threshold τ determines to what extent the generalized measures, $\tilde{\boldsymbol{\mu}}$, are denoised.

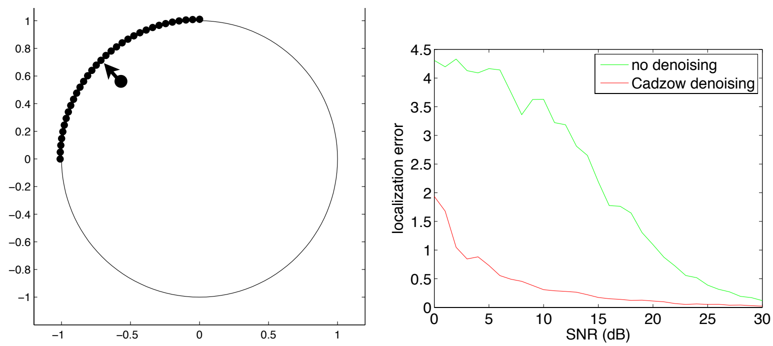

Figure 6.5: 6.5(a) The setting used to test the denoising scheme. 6.5(b) The localization error in function of the noise level using Cadzow's denoising (solid red line) and without any denoising (solid green line).

Chapter 7

Experimental Data

7.1 Summary

In this chapter we perform tests to evaluate the performance of the proposed framework; i.e., we compare the obtained localizations with theoretical lower bounds for the localization errors. We show to what extent analytic sensing can be spatially selective; i.e., we show if we can reconstruct the generating dipoles locally, one by one. Finally we treat a visual evoked potential (VEP) measured from a healthy subject to demonstrate the feasibility of our approach in a real EEG setting.

7.2 Motivation

We want to investigate how well the proposed algorithm behaves, theoretically and for real data. We want to evaluate the resolution, i.e., to quantify the influence of the distance between 2 generating dipoles on the localization error. In some sense we built a car without knowing how good it will drive. In this chapter we shall do a test-drive and look at the performance.

Analytic sensing is a non-linear source imaging technique in such we might expect a non-graceful degradation of the reconstruction quality as a function of the noise. Therefore we first compare the retrieval accuracy against the theoretical lower error bounds. We show the influence of a second, parasitic, source on the localization of the generating source. This reveals the spatial selectiveness of analytic sensing.

Finally, we treat an averaged 0.9s duration EEG recording stemming from a visual evoked potential and compare the obtained inverse solution to the result obtained by another state-of-the-art reconstruction algorithm, LAURA. In metaphorical terms, we shall take our new car for a spin and compare its performances with the Ferrari Testarossa of the field.

7.3 Accuracy of the retrieval

To evaluate the performance of the proposed algorithm in the presence of noise, we compute the CRLBs for the setting with the additive white Gaussian noise hypothesis [53]. Given noisy potential measures, these bounds establish the minimal covariance matrix of any *unbiased* estimate of the position and moment parameters. In other words, given the source configuration ρ (characterized by its positions and moments) and a noise model (e.g., additive white Gaussian noise) we can establish lower bounds on the mean error made by any unbiased estimator when estimating the underlying source model's parameters.

The signal model describing the noisy potential measures, $\tilde{v}\left(\mathbf{x};\mathbf{e}_n\right)$, is the following:

$$\tilde{v}\left(\boldsymbol{\theta};\mathbf{e}_n\right) = v\left(\boldsymbol{\theta};\mathbf{e}_n\right) + \varepsilon_n, \tag{7.1}$$

where $v\left(\boldsymbol{\theta};\mathbf{e}_n\right)$ is the ideally generated potential [62], measured at electrode $\mathbf{e}_n$,$\boldsymbol{\theta} = [\mathbf{x}_1, \mathbf{p}_1, \cdots, \mathbf{x}_M, \mathbf{p}_M]$ the source model's parameters and ε_n a normally distributed random variable with expected value 0 and variance σ^2 (the SNR of the measured signal is in direct relation to σ).

In order to compute these lower bounds, we determine the Fisher information matrix, $\mathbf{J} = [J_{k,l}]_{k,l\in\{1,\cdots,6M\}}$, corresponding to (7.1), which reads as follows:

$$J_{k,l} = \frac{1}{\sigma^2}\sum_{n=1}^{P}\frac{\partial}{\partial\boldsymbol{\theta}_k}v\left(\boldsymbol{\theta};\mathbf{e}_n\right)\frac{\partial}{\partial\boldsymbol{\theta}_l}v\left(\boldsymbol{\theta};\mathbf{e}_n\right), \tag{7.2}$$

with P the number of electrodes. The Cramér-Rao bounds are the diagonal elements of $\mathbf{J}^{-1}$.

The most important aspect when performing source localization is the reconstruction of the location parameters $\mathbf{x}_m$. Hence, when simulating we only consider the estimation of the location parameters.

7.3.1 Localizing one radial dipole

Figure 7.1(a) depicts the setup, i.e., the SMAC head model, the locations of the electrodes and the generating dipole whereas figure 7.1(b) depicts the corresponding ideal boundary potential and the positions of the singularities a_n of the analytic sensors. Using the setup of figures 7.1(a) and 7.1(b) we added noise to the potential measures and plotted the CRLBs and obtained localization errors, in X, Y and Z against the corresponding noise level in figures 7.2(a), 7.2(b) and 7.2(c). We see that up to a certain level of noise (±13dB) the CRLBs yield a good estimation of the performance of the localization. Further increasing the noise increases

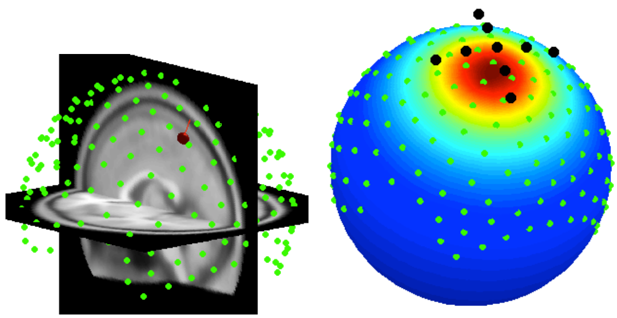

(a) (b)

Figure 7.1: Figures 7.1(a) and 7.1(b) depict the SMAC head model, which is a 3-sphere conductor model (the compartments represent the brain, skull and scalp), the generating radial unit dipole located at $\mathbf{x}_1 = [-0.4\ 0.2\ 0.6]$ (the red dot represents its location and the red line its moment, $\mathbf{p}_1 = \frac{\mathbf{x}_1}{||\mathbf{x}_1||}$) and singularities of the analytic sensors indicated by the black dots ($|a_n| = 1.01$). The green dots represent the electrodes' locations (this is a high density electrode configuration used at the University Hospital of Geneva).

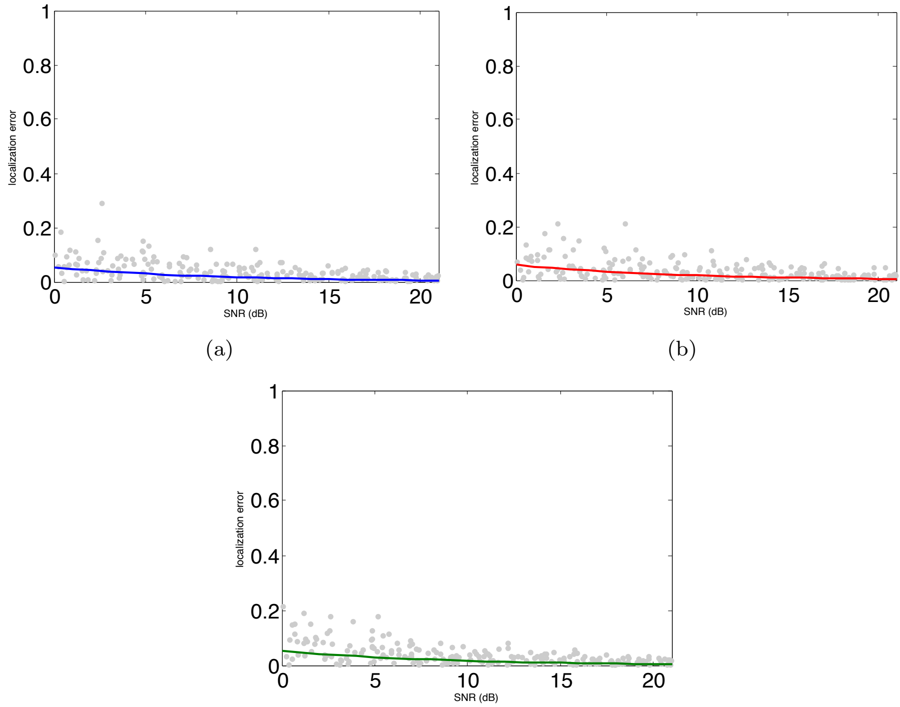

(c)

Figure 7.2: Figures 7.2(a), 7.2(b) and 7.2(c) depict the theoretical lower bounds on the localization errors of x_1, y_1 and z_1 (represented by the blue, red and green line) against the noise level (assuming additive white Gaussian noise). Moreover, we plotted the estimations of our method at different noise levels for different noise realizations (indicated by the gray dots).

7.3.2 A note on locally sensing a source

Note the placements of the poles a_n of the analytic sensors in figure 7.1(b); i.e., they are located above a zone that has a big activation. If we look at the amplitude of the potential measures, then we clearly see an area with high amplitude. Since the noise is additive Gaussian noise and hence not signal dependent, the measured signal quality in that area on the boundary is higher than elsewhere on the boundary. The generalized samples are computed via the boundary integral (3.1)

$$\langle \psi, \rho \rangle = -\int_{\partial\Omega} \sigma V \nabla \psi \cdot \mathbf{e}_\Omega \, \mathrm{d}s.$$

Since the analytic sensors are localized around a_n; i.e., $|\psi_{a_n}|$ is large close to a_n and relatively small elsewhere, they are spatially selective. It is advantageous to place the analytic sensors over an area with high signal quality to obtain high quality generalized measures. The areas that are highly corrupted by noise are “ignored” in such. Since mainly the potential measures close to a_n contribute to the generalized samples, we could try to reconstruct the generating sources locally, one by one. This concept is called local analytic sensing and is depicted in figure 7.3.

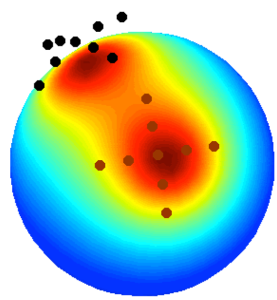

Figure 7.3: A setup with 2 generating dipoles and 2 sets of analytic sensors. Their respective singularities, a_n, are characterized by the black and brown dots. One set of analytic sensors (characterized by the black dots) will be used to reconstruct the upper dipole whereas the other set of analytic sensors (characterized by the brown dots) will be used to reconstruct the lower dipole. This way of reconstructing the dipoles locally, one by one is called “local analytic sensing”.

The governing equation (1.1) is linear; i.e., if a source distribution ρ_1 induces a potential V_1 and ρ_2 induces V_2, then $\rho = \rho_1 + \rho_2$ induces $V = V_1 + V_2$ and hence, when reconstructing a generating dipole locally the generalized samples will contain a contribution due to any other generating dipole in the conductor volume. This parasitic contribution depends on the strength and location of any other generating dipole. This bias introduces an error in the localization, as depicted in figures 7.4(a) and 7.4(b).

We see that the localization error grows if the distance between the 2 generating dipoles, $r = ||\mathbf{x}_1 - \mathbf{x}_2||$, increases. Moreover, we see that the impact of second dipole on the localization error is small if it has low intensity (because its manifestation on the boundary is dominated by the manifestation of the first dipole, with big intensity). An interesting observation is that the localization error decreases if the distance between the 2 dipoles is smaller than ± 0.4. By increasing the intensity of the first dipole it can compensate for the potential variation induced by the second dipole. In the extreme case where $\mathbf{x}_1 = \mathbf{x}_2$, the boundary potential can be explained by a dipole located at the position of the first dipole but with higher the intensity.

7.3.3 Localizing two radial dipoles

Figure 7.5(a) depicts the setup, i.e., the SMAC head model, the locations of the electrodes and the 2 generating dipoles whereas figure 7.5(b) depicts the corresponding ideal boundary potential and the positions of the singularities a_n of the analytic sensors. Using the setting of figures 7.5(a) and 7.5(b) we added noise to the potential measures and plotted the CRLBs on the localization errors and obtained localization errors against the corresponding noise level in figures 7.6(a) and 7.6(b). We see that up to a certain level of noise ($\pm$13dB) the CRLBs yield a good estimation of the performance of the localization. Further increasing the noise increases drastically the localization errors. This clearly demonstrates the non-linear behavior of the localization error; i.e, we do not observe a graceful performance degradation for smaller SNRs but rather a sudden performance degradation.

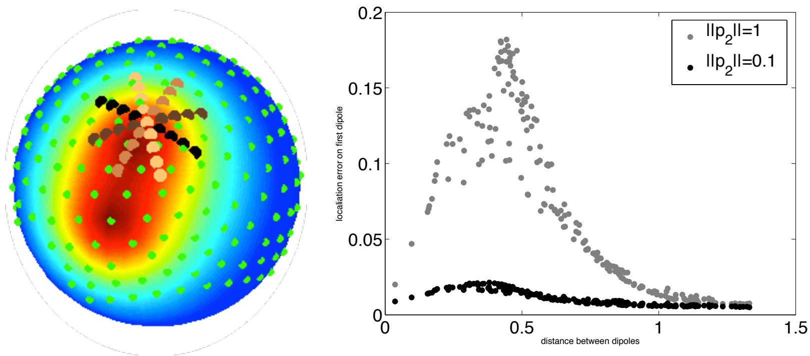

(a) (b)

Figure 7.4: Figure 7.4(a) shows the setting; i.e, we see 2 generating radial dipoles, located at $\mathbf{x}_1$ and $\mathbf{x}_2$, but the analytic sensors are set to detect only 1 dipole locally. Figure 7.4(b) shows the influence of the second dipole's proximity on the localization error of the first dipole. The black dots represent the localization error on the first dipole when the second dipole has an intensity $||\mathbf{p}_2|| = 0.1$ whereas the gray dots represent the localization error on the first dipole when the second dipole has a unit intensity $||\mathbf{p}_2|| = 1$. Note that, the second "parasitic" dipole always had the same distance from the origin as the first dipole, $\mathbf{x}_1 = \mathbf{x}_2$.

7.4 Experimental data: an averaged visual evoked potential

7.4.1 General description

An evoked potential (EP) is the characteristic electrical potential recorded over a typically $0.9 - 1s$ time window by the EEG following the presentation of a stimulus. For example, if the stimulus is a flash, then the induced characteristic potential is a visual evoked potential.

The regions of the brain responsible for the processing of such stimuli are often

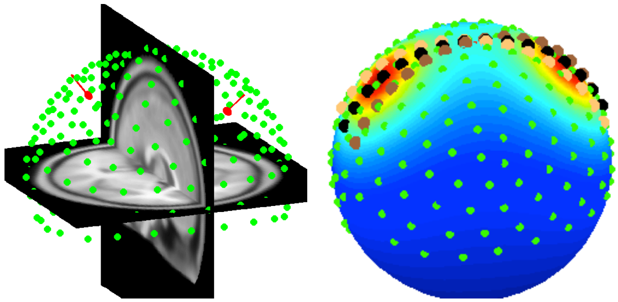

(a) (b)

Figure 7.5: Figures 7.5(a) and 7.5(b) depict the SMAC head model, which is a 3-sphere conductor model (the compartments represent the brain, skull and scalp), the generating radial unit dipoles located at $\mathbf{x}_1 = [0.4\ 0.4\ 0.6]$ and $\mathbf{x}_1 = [-0.4\ \ -0.4\ 0.6]$ (the red dots represent the locations and the red lines their moments) and singularities of the analytic sensors indicated by the black dots ($|a_n| = 1.01$). The green dots represent the electrodes' locations (this is a high density electrode configuration used at the University Hospital of Geneva).

well-localized. For example, when a flash to the right eye is processed by the brain, the visual cortex will be stimulated first. It is reasonable to assume that the dipole model is valid at certain time points during the EP [63], especially in the early stages of the EP. However, the amplitudes of EPs tend to be low, ranging from less than a microvolt to several microvolts, compared to tens of microvolts for spontaneous EEG recordings. To resolve these low-amplitude potentials against the background of ongoing electrical brain activity and measurement noise, signal averaging is required [64]; i.e., the signal is time-locked to the stimulus and averaged over repeated EPs.

The EP that we analyze is acquired by Michael A. Pitts and used in a binocular rivalry experiment. In what follows we describe which subjects were used, what stimuli were presented, the EEG system used to acquire the data and how the raw data was processed. These specifications are taken from [65, 66]. The authorization

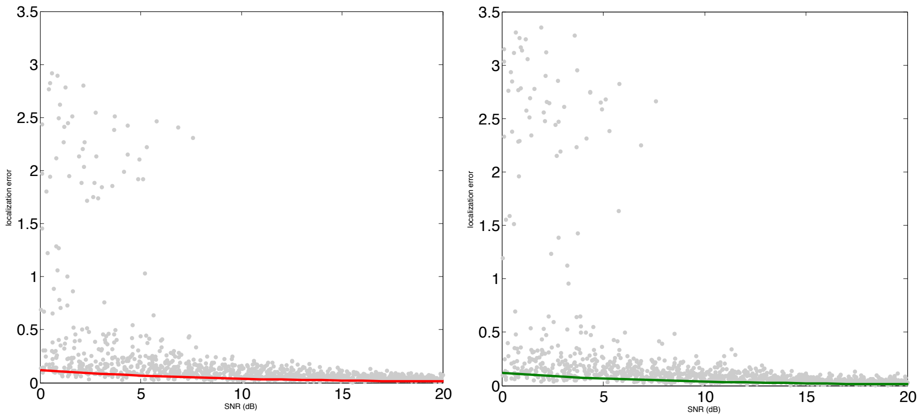

(a) (b)

Figure 7.6: Figures 7.6(a) and 7.6(b) depict the obtained localization errors (gray dots) in function of the noise level. Moreover, we plotted the statistical lower bound on the localization error for the first dipole (solid red line) and for the second dipole (solid green line).

to use this data in this dissertation has explicitly been requested and granted.

7.4.2 Participants

Fourteen healthy adults, 8 females and 6 males aged between 18 and 23 years, participated in the experiment. One subject was excluded from the analyses due to substantial contamination by artifacts. The data of the remaining 13 subjects was submitted to subsequent analyses. All had normal or corrected-to normal visual acuity and no history of psychiatric or neurological impairments. All participants were recruited as volunteers and gave informed consent.

7.4.3 Stimuli and procedure

The stimuli were square-shaped sinusoidal gratings that subtend 6° visual angle in diameter and differed in color (green versus red), orientation (45° versus 135°) and spatial frequency (1 cycle per degree versus 5 cycles per degree). The stimuli were presented during 600ms on a black background and were centered horizontally within the left and right halves of a CRT computer screen with a 60Hz refresh rate. Following the stimulus was a 500-700ms blank screen during which the subject had to indicate the stimulus he or she saw. Figure 7.4.3 shows a sequence where first a green high frequency is presented to the right eye followed by a red low frequency to the left eye.

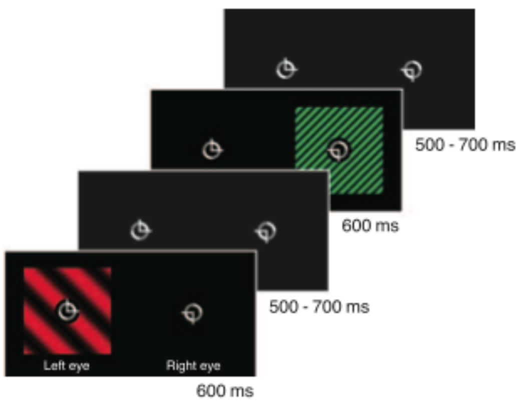

Figure 7.7: The stimuli presented to the subject. This figure is taken from [66].

Here, we only consider the EPs elicited in the high spatial frequency condition, collapsed across color and orientation. The reason for this is that the primary visual cortex is highly sensitive to the processing of spatial frequencies, and high spatial frequency stimuli elicit relatively large components in early visual areas. Each condition comprised 1200 trials and roughly 10% of the trials were omitted because the measured signal contained artifacts or to much measurement noise. The averaged EP that we analyzed is the average of all the retained EPs over all 13 subjects corresponding to the high frequency stimuli. Note that, this is an average over a huge number of trials which ensures that the treated EP is of high quality; i.e., the SNR of such an averaged signal is considerably higher then the SNR of a single trial measurement. Note that, it makes sense to assume that the remaining noise is normally (or Gaussian) distributed due to the "central limit theorem".

7.4.4 EEG acquisition and data processing

The generated scalp potential was measured in 64 tin electrodes mounted in an elastic cap, band-pass filtered between 0.1 and 80Hz and sampled at 250Hz. Horizontal and vertical eye movements, which corrupt the EP, were monitored. The measured EEG was recomputed offline to the common average reference. Before selecting the relevant time windows (called epochs in EEG terminology), the DC component was removed and then band-pass filtered between 1 and 30Hz. The resulting averaged EP is depicted in figure 7.8.

7.4.5 Source analysis

During the time span of the averaged EP there are those characteristic components at which time the generating source distribution is "well-understood" (read "well-localized"). For example, the boundary potential that pops up at ±100ms after the stimulus is called the C1 component and stems from the primary visual cortex. The N1 component, seen at ±180ms after the stimulus, stems from 2 focal brain areas. These components appear during the early stages of the averaged EP and are linked to the physical stimulus. On the other hand, the P2 component stems from a distributed source distribution. Figure 7.9 shows the number of dipoles that explain well the measured EEG through the VEP. Figure 7.10 depicts the C1,N1 and P2 components in time and the corresponding potential maps[1].

We compare the inverse solution of from LAURA with the inverse solution yielded by analytic sensing. We are well-aware that we compare the solution of a distributed model with the solution of a dipole model. However, if we plot an ellipsoid corresponding to the uncertainty (computed using the CRLBs) of the reconstructed location(s), then we hope to see some overlap between the inverse solution from LAURA and our inverse solution. This only makes sense if the unexplained

[1]We used the interpolation scheme described in the chapter 6 with $L = 11$ and $\sigma = 0$ to generate these potential maps.

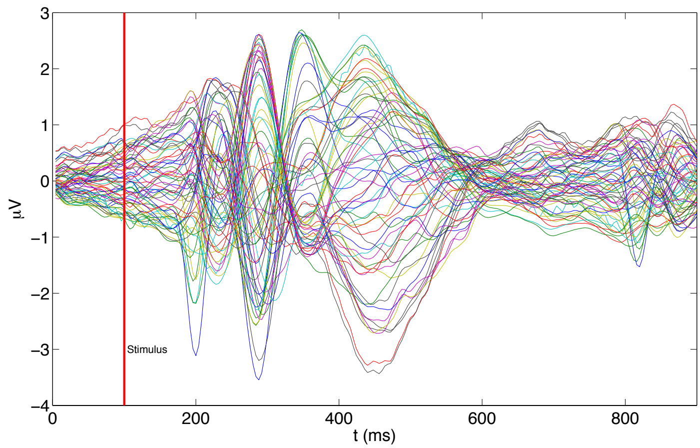

Figure 7.8: The averaged visual EP corresponding to the high frquency sinusoid (measured in μV over 0.9s). Each line represents the potential measured by the corresponding electrode over a 0.9s time frame. The red line represents the moment that the stimulus was presented.

data is distributed normally, since the CRLBs assume additive noise that is normally distributed. We performed a statistical test that indicates to what extent the unexplained data is normally distributed. This is quantified by the p-value, which is the probability of erroneously rejecting the hypothesis that the unexplained data is normally distributed. If the p-value is smaller then 10% then we do not suppose that the unexplained data is normally distributed. In that case, we fit more dipoles to the measured data (until the remaining unexplained data is normally distributed). However, if we see that the proportion of explained data does not increase, or it cannot be assumed that the unexplained data is normally distributed, then the underlying source distribution is likely not dipolar.

The first component, depicted in figure 7.10(b), stems from the primary visual cortex (also known as striate cortex or V1) which is located in both hemispheres. Figure 7.11 shows the inverse solutions obtained by LAURA and our method when

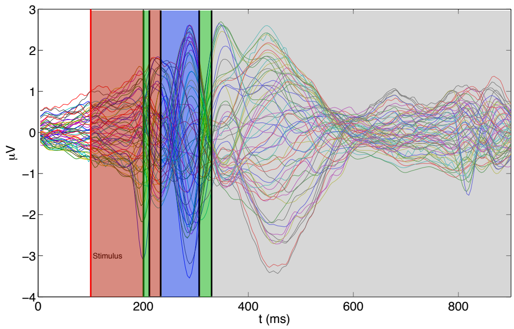

Figure 7.9: The visual evoked potential with the number of dipoles that properly explain the measurements as colored rectangles (red indicates 1 dipole, green 3 dipoles and blue 2 dipoles). The gray area is known to be generated by a distributed source model.

fitting 1 dipole to the measured boundary potential. We see that the solution points with maximum intensity coincide with the dipole's location found through analytic sensing and those happen to be located in V1. If we look at the uncertainty of the reconstructed location then we see that the reconstructed dipole resides in either left or right hemisphere, which makes sense since the visual primary cortex resides in both hemispheres. Moreover, the p-value is rather high (p-value≈ 0.206) which indicates that the unexplained signal is likely normally distributed. If we fit 2 dipoles to the C1 component then we obtain a dipole in the center of the brain in addition to the dipole localized in V1, as depicted in figure 7.12. The corresponding p-value is a bit smaller (p-value≈ 0.15) but still high enough to assume that the unexplained signal is normally distributed. On the other hand, 82% of the signal is explained by these two dipoles against the previously 62%. Anatomically speaking, the second dipole covers part of the human visual system (HVS) so reconstructing a dipole over there might be plausible. Moreover, if we look at the solution given by LAURA, then we see that the solution points in that area have a rather high intensity.

It is generally accepted that the second component, depicted in figure 7.10(c), is

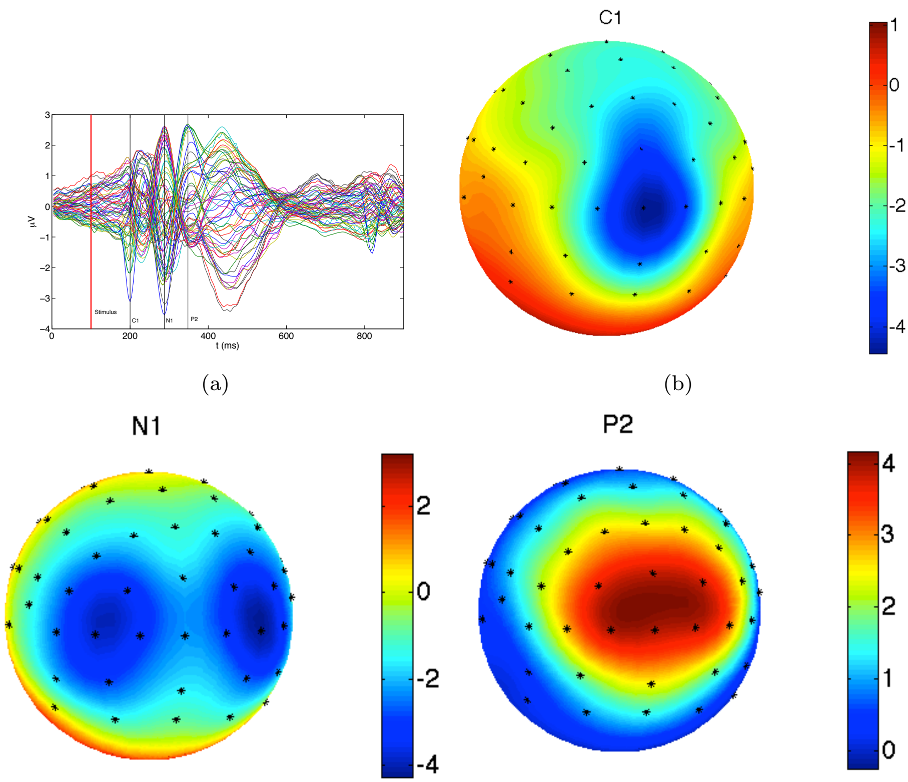

(a) (b) (c) (d)

Figure 7.10: 7.10(a) The averaged EP and the C1, N1 and P2 components in time (seen from the back of the head). 7.10(b) The potential map of the C1 component. 7.10(c) The potential map of the N1 component. 7.10(d) The potential map of the P2 component. The unit corresponding to the colorbars is μV

best explained by 2 dipoles. In our case, assuming 2 generating dipoles explains the measured signal up to $\approx 98\%$ and the non-explained signal is distributed normally with a high probability (p-value$\approx 0.64\%$). We observe that our algorithm obtains 2 dipoles that are less lateral than the solution proposed by LAURA. Unfortunately these dipoles are located in the white matter. It is known that no EEG generators are located in the white matter. On the other hand it has to be noted that the measured data can be explained extremely well with the 2 obtained dipoles.

Finally, we took a look at the P2 component. It is generally accepted that this component already stems from a distributed source distribution. Nonetheless, we tried to fit a dipolar model to the measured data with analytic sensing. If we fit 2 dipoles then we explain $\approx$78% of the measured data. However, the probability that the non-explained portion of the data is normally distributed is rather small (p-value ≈ 0.05), which means that the unexplained data is probably not just noise. If we fit 3 dipoles to the measured signal, then we explain $\approx 90\%$ of the measured data and we have a p-value of ≈ 0.34 which indicates that the unexplained data is probably normally distributed. In such we might say that these 3 dipoles explain sufficiently the measured data. However, we should be cautious when interpreting the result since the sparse a priori, on which our model is based, might not be valid.

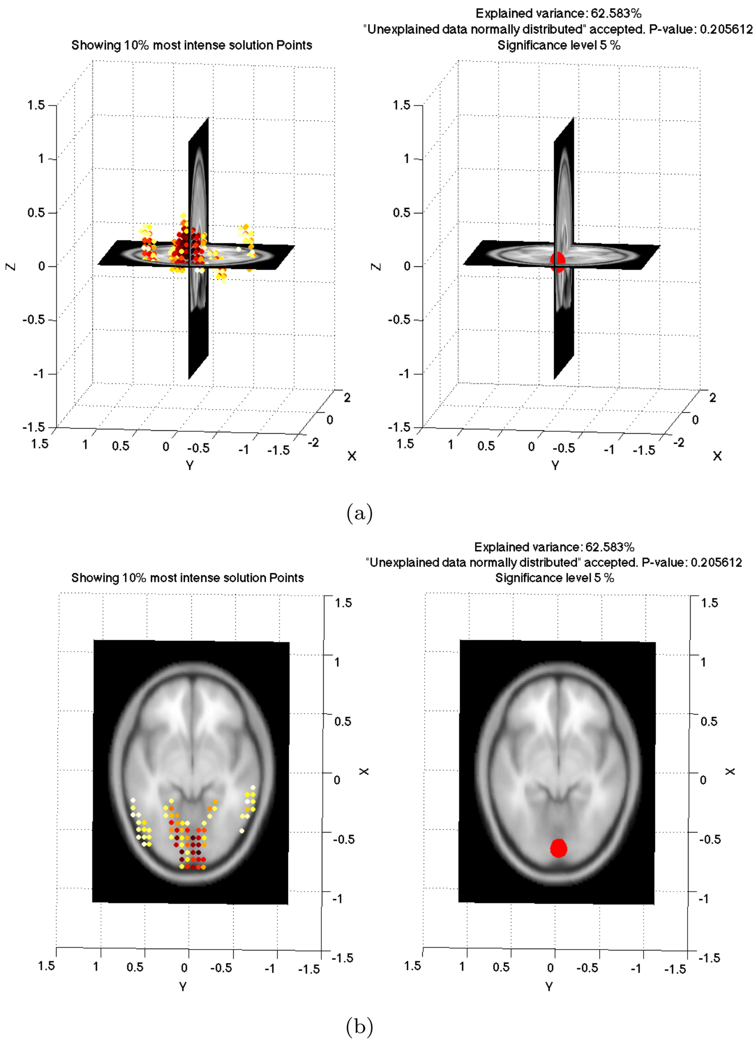

Figure 7.11: The inverse solution obtained by LAURA versus the inverse solution obtained by analytic sensing for the C1 component. For LAURA we only show the solution points with high intensity (10% of the total number of solution points). Note that, the nose of the subject points towards the positive X-axis. 7.11(b) The same inverse solution but seen from above.

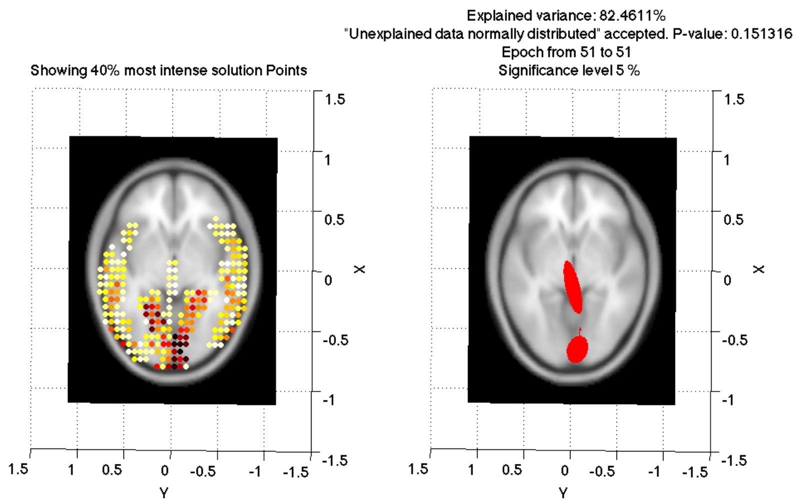

Figure 7.12: The inverse solution obtained by LAURA versus the inverse solution obtained by analytic sensing, when fitting 2 dipoles to the C1 component. For LAURA we only show the solution points with high intensity (40% of the total number of solution points). Note that, the nose of the subject points towards the positive X-axis.

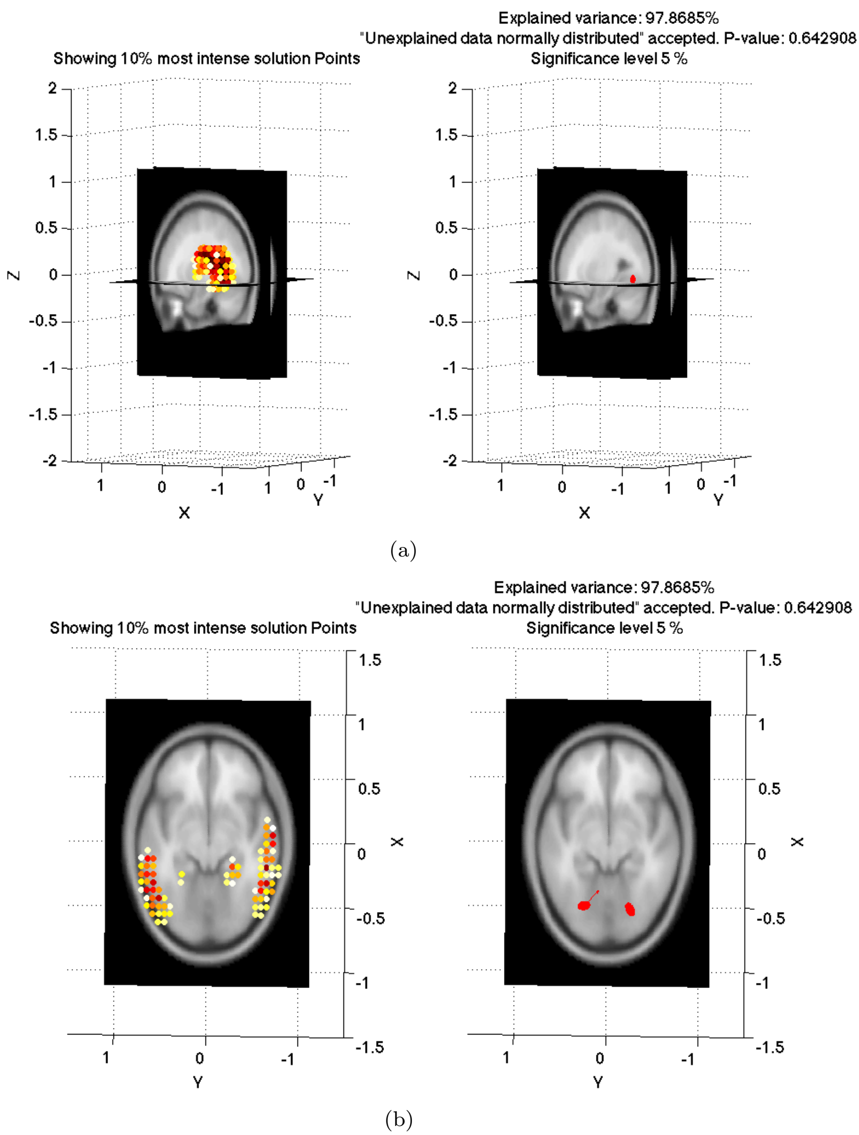

Figure 7.13: The inverse solution obtained by LAURA versus the inverse solution obtained by analytic sensing for the N1 component. For LAURA we only show the solution points with high intensity (10% of the total number of solution points). Note that, the nose of the subject points towards the positive X-axis. 7.13(b) The same inverse solution but seen from the left.

Chapter 8

Conclusion

In this thesis we have developed a new framework called "analytic sensing" to reconstruct dipoles from boundary measurements that stem from Poisson's equation with a particular focus on the inverse problem that occurs in EEG source imaging. More specifically, we have devised a direct, non-iterative estimation technique to reconstruct the dipoles responsible for the measured EEG. Moreover, validation shows that results from analytic sensing reach the Cramér-Rao bounds up to certain level of noise. The main findings and results are summarized in the next section.

8.1 Summary of findings and results

- **Ill-posed versus well-posed inverse EEG problem**
  We have shown that the inverse EEG problem is ill-posed; e.g., multiple source distributions can generate the same boundary potential. To render the problem well-posed we imposed a sparsity constraint. More specifically, we assumed that the generating source distribution is a sum of M dipoles. The corresponding, well-posed, inverse problem consists of finding the locations and moments of the generating source distribution.

- **Sampling a 2D source distribution with analytic test functions**
  We have applied Green's theorem in combination with a well-chosen test functions to obtain measures of the generating source distribution knowing

only the induced boundary potential. These measures, called generalized samples, are in fact the scalar products between the source distribution and those test functions. We have identified a class of such analytic test functions, called "analytic sensors", that allow for an efficient reconstruction algorithm.

- **An FRI approach to reconstruct the generating 2D dipoles**
  We have shown that these generalized samples are conform with a FRI setup. That is, we can construct a filter that annihilates these generalized samples multiplied with some unknown polynomial whose roots are the generating dipoles' locations. This convolution can be rewritten as a linear system of equations in the unknown coefficients of that polynomial. However, localization through root finding is prone to noise; we adapted Cadzow's iterative denoising scheme for added robustness. Once the locations of the dipoles are known, it is easy to obtain the dipoles' moments since the generalized samples depend linearly on the moments. Note, the non-linear estimation of the locations is decoupled from the linear estimation of the moments.

- **Extension to 3D**
  First, we have extended the computation of the generalized samples to a 3D setting. Formally nothing changes; i.e., the line integral involved becomes a surface integral in 3D. Second, we noted that the FRI-like reconstruction technique yields orthographic projections of the dipoles' locations and moments. We introduced a coordinate transform to obtain different 2D projections of the 3D locations and moments. Eventually we adapted "Tomasi and Kanade's rank principle" to reconstruct the full 3D source distribution from the unordered 2D projections.

- **Non-homogeneous conductor models**
  The knowledge on the conductor model is contained in the analytic sensors. We have explicitly constructed analytic sensors that go with spherical models. In particular, we show how to analytically construct the analytic sensors that go with N-sphere head models. Such head models play an important role in EEG source imaging; e.g., the SMAC head model is essentially a 3-sphere head model. Moreover, we have shown the effect of incorporating the conductivity profile on the localization error.

8.2 Outlook

Although the framework seems to perform rather well with real EEG data, there are a couple of features that might make this algorithm even more attractive to use in EEG applications:

- **Realistic head models**
  We have used spherical models, more specifically layered spheres, to model the human head. Unfortunately the human head is anything but a sphere. However, if we use realistic head models, then we do not have an analytic expression for the analytic sensors nor for the generated boundary potential [67]. As a consequence we would need numerical techniques, such as boundary element or finite element methods, to propagate the analytic sensor through the conductor model to the outer surface. Note that, in such realistic head models, the conductivity can no longer be assumed to be isotropic but rather a direction-dependent tensor [68].

- **Denoising**
  Although we have incorporated Cadzow's iterative denoising scheme we could still do a bit more. We could try and denoise the matrix, $\mathbf{L}$, that contains the 2D projections of the dipoles because we have quite some unused information; i.e., $\text{rank}(\mathbf{L}) = 3$ and the x- and y-components of the 2D projections lie, ideally, on a sinusoidal curve.

- **Spatial extent of the sources**
  It is rare that the source distribution is really well-modeled by a point source (read a dipole). Often the generating sources have a spatial extent. In such, it would make sense to use different parameterizations for the source distribution; e.g., a 3D Gaussian or a 3D box spline. In that case we could try to adapt the FRI-like localization to estimate the characterizing parameters of the source distribution.

- **Non-localized analytic sensors for 3D**
  We could introduce a second set of analytic sensors, $z \ln(x + iy - a)$, to reconstruct the z-components of the generating dipoles' locations and moments. The corresponding generalized samples depend linearly on z_m and p_{z_m} and hence, since $x_m + iy_m$ and $p_{x_m} + ip_{y_m}$ are known using the "classic" analytic

sensor, the z_m and pz_m could be obtained by solving a linear system of equations. However, these analytic sensors are less (not to say not) localized which is a severe hindrance in the case of EEG since the signal quality is extremely low in the areas where there's no activation (not to mention the part where we do not have any measures). This approach might be useful in applications with better signal quality (and coverage).

- **Governing equation**
  In this manuscript we have considered only Poisson's equation as the governing equation. However, analytic sensing can be extended to cope with Helmholtz's equation as a governing equation. This partial differential equation often arises in the field of physics. It might hence be fruitful to extend analytic sensing for Helmholtz's equation. For this we need to construct a test function, ψ, that allows for an FRI-lime reconstruction whilst satisfying

  $$\Delta\psi + k^2\psi = 0.$$

  For example, if the activation can be modeled through a superposition of diracs, then

  $$\psi_{a_n}(x, y, z) = \frac{e^{ikz}}{x + iy - a_n}$$

  is a valid analytic sensor.

- **Brain computer interfaces**
  Brain computer interfaces (BCIs) try to operate a machine (e.g., a wheelchair or a prosthetic arm) by mere "thought". Basically, some electrodes are stuck the subjects head and the measured EEG holds information to automatically decipher the subjects intention. The, say, wheelchair then acts accordingly; e.g., if the subject wants to go left, then the wheelchair should decide to go left (solely by processing the measured EEG). The configuration of the generating dipoles might have enough discriminating power to be used as a feature for classifiers in the decision taking. In other words, the reconstructed dipoles can help to decipher the subject's intention. It would be interesting to see to what extent analytic sensing is capable to perform in such settings.

8.3 Concluding remarks

Finally, we would like to give some concluding remarks with respect to analytic sensing in an EEG setting.

- **Validity of the model**
  Analytic sensing uses a strong sparsity constraint; i.e., we assume that the potential is generated by a superposition of M dipoles. In such, before trying to give any biological or neurophysiological interpretation to the obtained results we should verify that the potential measures indeed stem from a multi-dipole source distribution. If not, we should be cautious when interpreting the obtained result. We could, for example, simulate a Gaussian distribution and try to fit dipoles to the measured boundary potential. It would be interesting to see if analytic sensing yields dipoles located at the center of the Gaussian. In that case the multi-dipole fit would be a good competitor against the distributed source model.

- **Occam's razor**
  Occam's razor, also known as law of sparsity or law of succinctness, recommends selecting the competing hypothesis that makes the fewest new assumptions, when the hypotheses are equal in other respects. This belief, or rather philosophy, is widespread among engineers. If we interpret the law of sparsity with respect to the work done in this manuscript, then it states that the model that explains the measured data up to the level of noise with the fewest dipoles is accepted as the best one.

- **Quality of EEG measurements**
  First we would like to point out that the generally accepted boundary condition is not entirely correct; i.e., the head is not a closed volume and hence some current does leave the conductor model. Second, the quality of the measured signal is rather bad (especially in non-averaged EEG). However, the signal-to-noise ratio may be acceptable in those areas where there is focused activation; e.g., the part of the scalp just above the primary visual cortex when presented with a visual stimulus. This is a good opportunity to apply local analytic sensing. Another potential application is partial epilepsy where the early onset might be focused an appropriate to be fitted with our model.

Appendix A

Appendices

A.1 Propagation of $\ln(\zeta - a)$ through $\partial\Omega_1$

Consider the functions φ_1 and Φ_1 which are defined from the center up to the boundary $\partial\Omega_1$ of the 3-sphere conductor model $\mathcal{S}$ (depicted in figure 5.1):

$$\begin{aligned} \varphi_1(\zeta) &= \ln(\zeta - a), \\ \Phi_1(\frac{\zeta}{r^2}) &= 0, \end{aligned}$$

with $a \notin \mathcal{S}$. Next, we define the functions f_1 and g_1 as stated in equations (5.10) and (5.11):

$$\begin{aligned} f_1(\zeta) &= \ln(\zeta - a), \\ g_1(\zeta) &= \frac{\sigma_1}{\sigma_2}\frac{\zeta}{\zeta - a}. \end{aligned}$$

In order to propagate Φ_1 trough the boundary Ω_1, which yield Φ_2, we need to solve the ODE (5.8) for $j = 1$:

$$\frac{2\zeta}{r_1^3}\Phi_2'\left(\frac{\zeta}{r_1^2}\right) + \frac{1}{r_1}\Phi_2\left(\frac{\zeta}{r_1^2}\right) = -g_1(\zeta) + \zeta f_1'(\zeta). \tag{A.1}$$

Since Φ_2 is an entire function, we can write:

$$\Phi_2\left(\frac{\zeta}{r_1^2}\right) = \sum_{k\geq 0} c_k \left(\frac{\zeta}{r_1^2}\right)^k . \tag{A.2}$$

For the RHS of the ODE (A.1), we have:

$$\begin{aligned} -g_1(\zeta) + \zeta f_1'(\zeta) &= \left(1 - \frac{\sigma_1}{\sigma_2}\right)\frac{\zeta}{\zeta - a}, \\ &= \left(\frac{\sigma_1}{\sigma_2} - 1\right)\sum_{k\geq 0}\left(\frac{\zeta}{a}\right)^{k+1} . \end{aligned} \tag{A.3}$$

If we substitute the expressions (A.2) and (A.3) in the ODE (A.1), then we obtain:

$$\sum_{k\geq 0} c_k \frac{2k+1}{r_1^{2k+1}}\zeta^k = \left(\frac{\sigma_1}{\sigma_2} - 1\right)\sum_{k\geq 0}\left(\frac{\zeta}{a}\right)^{k+1},$$

from which we infer the coefficients c_k:

$$\begin{aligned} c_0 &= 0, \\ c_k &= \left(\frac{\sigma_1}{\sigma_2} - 1\right)\frac{r_1^{2k+1}}{(2k+1)a^k}, \quad \text{for } k \geq 1. \end{aligned}$$

This yields the following expression for Φ_2:

$$\Phi_2\left(\frac{\zeta}{r^2}\right) = \left(\frac{\sigma_1}{\sigma 2} - 1\right)\sum_{k\geq 1}\frac{r_1^{2k+1}}{(2k+1)a^k}\left(\frac{\zeta}{r^2}\right)^k .$$

If we set $j = 1$ in equation (5.9), then we obtain an expression for φ_2:

$$\begin{aligned} \varphi_2(\zeta) &= f_1(\zeta) - \frac{1}{r_1}\Phi_2\left(\frac{\zeta}{r_1^2}\right), \\ &= \ln(\zeta - a) - \left(\tfrac{\sigma_1}{\sigma 2} - 1\right)\textstyle\sum_{k\geq 1}\dfrac{\zeta^k}{(2k+1)a^k}. \end{aligned}$$

A.2 Propagation of φ_2 through $\partial\Omega_2$

Consider the functions φ_2 and Φ_2 (as constructed in the previous appendix) which are defined from the center up to the boundary $\partial\Omega_2$ of the 3-sphere conductor model$\mathcal{S}$ (depicted in figure 5.1):

$$\begin{aligned}\varphi_2(\zeta) &= \log(\zeta - a) - \left(\tfrac{\sigma_1}{\sigma 2} - 1\right) \textstyle\sum_{k\geq 1} \dfrac{\zeta^k}{(2k+1)a^k} \\ \Phi_2\left(\tfrac{\zeta}{r^2}\right) &= \left(\tfrac{\sigma_1}{\sigma 2} - 1\right) \textstyle\sum_{k\geq 1} \dfrac{r_1^{2k+1}}{(2k+1)a^k} \left(\dfrac{\zeta}{r^2}\right)^k,\end{aligned}$$

with $a \notin \mathcal{S}$. Next, we define the functions f_2 and g_2 as stated in equations (5.10) and (5.11):

$$\begin{aligned}f_2(\zeta) &= \log(\zeta - a) - \left(\frac{\sigma_0}{\sigma_1} - 1\right) \textstyle\sum_{k\geq 1} \left(1 - \dfrac{r_1^{2k+1}}{r_2^{2k+1}}\right) \dfrac{1}{(2k+1)a^k}\zeta^k \\ g_2(\zeta) &= -\frac{\sigma_2}{\sigma_3} \sum_{k\geq 1} \left(\frac{1}{a^k} + \left(\frac{\sigma_1}{\sigma_2} - 1\right) \frac{k}{(2k+1)a^k} + \left(\frac{\sigma_1}{\sigma_2} - 1\right) \frac{(k+1)r_1^{2k+1}}{(2k+1)a^k r_2^{2k+1}} \right) \zeta^k\end{aligned}$$

In order to propagate Φ_2 trough the boundary Ω_2, which yield Φ_3, we need to solve the ODE (5.8) for $j = 2$:

$$\frac{2\zeta}{r_2^3}\Phi_3'\left(\frac{\zeta}{r_2^2}\right) + \frac{1}{r_2}\Phi_3\left(\frac{\zeta}{r_2^2}\right) = -g_2(\zeta) + \zeta f_2'(\zeta). \tag{A.4}$$

Since Φ_3 is an entire function, we can write:

$$\Phi_3\left(\frac{\zeta}{r_2^2}\right) = \sum_{k\geq 0} c_k \left(\frac{\zeta}{r_2^2}\right)^k. \tag{A.5}$$

For the RHS of the ODE (A.4), we have:

$$\begin{aligned}-g_2(\zeta) + \zeta f_2'(\zeta) = &\left(\tfrac{\sigma_2}{\sigma_3} - 1\right) \textstyle\sum_{k\geq 1} \dfrac{\zeta^k}{a^k} + \\ &\left(\tfrac{\sigma_1}{\sigma_2} - 1\right)\left(\tfrac{\sigma_2}{\sigma_3} - 1\right) \textstyle\sum_{k\geq 1} \dfrac{k}{2k+1}\left(\dfrac{\zeta}{a}\right)^k + \\ &\left(\tfrac{\sigma_1}{\sigma_2} - 1\right) \textstyle\sum_{k\geq 1} \dfrac{\left(\frac{\sigma_2}{\sigma_3}(k+1) + k\right) r_1^{2k+1}}{(2k+1)r_2^{2k+1}} \left(\dfrac{\zeta}{a}\right)^k.\end{aligned} \tag{A.6}$$

If we substitute the expressions (A.5) and (A.6) in the ODE (A.4), then we obtain:

$$\begin{aligned}
\textstyle\sum_{k\geq 0} c_k \frac{2k+1}{r_2^{2k+1}}\zeta^k &= \left(\tfrac{\sigma_2}{\sigma_3}-1\right)\textstyle\sum_{k\geq 1}\frac{\zeta^k}{a^k}+ \\
&\left(\tfrac{\sigma_1}{\sigma_2}-1\right)\left(\tfrac{\sigma_2}{\sigma_3}-1\right)\textstyle\sum_{k\geq 1}\frac{k}{2k+1}\left(\frac{\zeta}{a}\right)^k+ \\
&\left(\tfrac{\sigma_1}{\sigma_2}-1\right)\textstyle\sum_{k\geq 1}\frac{\left(\frac{\sigma_2}{\sigma_3}(k+1)+k\right)r_1^{2k+1}}{(2k+1)r_2^{2k+1}}\left(\frac{\zeta}{a}\right)^k,
\end{aligned}$$

from which we infer the coefficients c_k:

$$\begin{aligned}
c_0 &= 0, \\
c_k &= \left(\frac{\sigma_2}{\sigma_3}-1\right)\frac{r_2^{2k+1}}{(2k+1)a^k}+\left(\frac{\sigma_1}{\sigma_2}-1\right)\left(\frac{\sigma_2}{\sigma_3}-1\right)\frac{kr_2^{2k+1}}{(2k+1)^2a^k}+ \\
&\left(\frac{\sigma_1}{\sigma_2}-1\right)\frac{\left(\frac{\sigma_2}{\sigma_3}(k+1)+k\right)r_1^{2k+1}}{(2k+1)^2a^k}, \quad \text{for } k\geq 0.
\end{aligned}$$

This yields the following expression for Φ_3:

$$\begin{aligned}
\Phi_3\left(\tfrac{\zeta}{r^2}\right) &= \left(\tfrac{\sigma_2}{\sigma_3}-1\right)\sum_{k\geq 1}\frac{r_2^{2k+1}}{(2k+1)a^k}\left(\frac{\zeta}{r^2}\right)^k+ \\
&\left(\tfrac{\sigma_1}{\sigma_2}-1\right)\left(\tfrac{\sigma_2}{\sigma_3}-1\right)\sum_{k\geq 1}\frac{kr_2^{2k+1}}{(2k+1)^2a^k}\left(\frac{\zeta}{r^2}\right)^k+ \\
&\left(\tfrac{\sigma_1}{\sigma_2}-1\right)\sum_{k\geq 1}\frac{\left(\frac{\sigma_2}{\sigma_3}(k+1)+k\right)r_1^{2k+1}}{(2k+1)^2a^k}\left(\frac{\zeta}{r^2}\right)^k
\end{aligned}$$

If we set $j = 2$ in equation (5.9), then we obtain an expression for φ_3:

$$\begin{aligned}
\varphi_3(\zeta) &= f_2(\zeta) - \frac{1}{r_2}\Phi_3\left(\frac{\zeta}{r_2^2}\right), \\
&= \log(\zeta - a) - \left(\tfrac{\sigma_1}{\sigma_2} - 1\right)\sum_{k\geq 1}\left(1 - \left(\frac{r_1}{r_2}\right)^{2k+1}\right)\frac{\zeta^k}{(2k+1)a^k} - \\
&\quad \left(\tfrac{\sigma_2}{\sigma_3} - 1\right)\sum_{k\geq 1}\frac{\zeta^k}{(2k+1)a^k} - \left(\frac{\sigma_1}{\sigma_2} - 1\right)\left(\frac{\sigma_2}{\sigma_3} - 1\right)\sum_{k\geq 1}\frac{k\zeta^k}{(2k+1)^2 a^k} - \\
&\quad \left(\tfrac{\sigma_1}{\sigma_2} - 1\right)\sum_{k\geq 1}\frac{\left(\tfrac{\sigma_2}{\sigma_3}(k+1) + k\right) r_1^{2k+1}}{(2k+1)^2 a^k r_2^{2k+1}}\zeta^k,
\end{aligned}$$

which yields an expression for $\psi_a(\zeta, r) = \varphi_3(\zeta) + \frac{1}{r}\Phi_3\left(\frac{\zeta}{r^2}\right)$.

Figure A.2 depicts a vector-field representation of $\psi_a(\zeta, r) = \varphi_3(\zeta) + \frac{1}{r}\Phi_3\left(\frac{\zeta}{r^2}\right)$ with $r_1 = 0.86$, $r_2 = 0.92$ and r_3=1. The conductivities are $\sigma_1 = 1$, $\sigma_2 = 0.0125$ and $\sigma_3 = 1$. The singularity was chosen on the x-axis, $a = 1.5$.

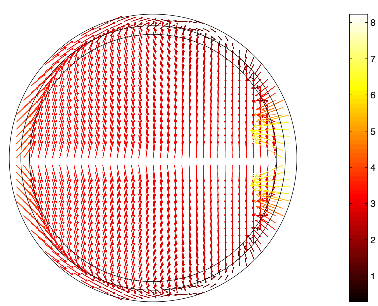

Figure A.1: Vector-field representation of the analytic sensor, $\psi_a(\zeta, r) = \varphi_3(\zeta) + \frac{1}{r}\Phi_3\left(\frac{\zeta}{r^2}\right)$. The color indicates the magnitude of the analytic sensor in the considered point.

Bibliography

[1] J.K. Mai, J. Assheuer, and G. Panixos, *Atlas of the Human Brain*, Academic Press, 1998.

[2] R.M. Gulrajni, *Bioelectricity and Biomagnetism*, John Wiley & Sons, 1998.

[3] D. Johnston and S. M.-S. Wu, *Foundations of Cellular Neurophysiology*, the MIT Press, 1998.

[4] E. Niedermeyer and F. Lopez Da Silva, *Electroencephalography: Basic Principles, Clinical Applications, and Related Fields*, Lippincott Williams and Wilkins, 2004.

[5] S. Baillet, J.C. Mosher, and R.M. Leahy, "Electromagnetic brain mapping," *IEEE Signal Processing Magazine*, , no. 7, pp. 14–30, November 2001.

[6] H. Berger, "´Uber das Elektroenkephalogramm des Menschen," *Arch. Psychiatr. Nervenkr.*, vol. 87, pp. 527–570, 1929.

[7] P.L. Nunez and R. Srinivasan, *Electric Fields of the Brain*, Oxford University Press, 2006.

[8] J. Hadamard, "Sur les problèmes aux dérivées partielles et leur signification physique," *Princeton University Bulletin*, pp. 49–52, 1902.

[9] A. El Badia and T. Ha-Duong, "An inverse source problem in potential analysis," *Inverse Problems*, vol. 16, pp. 651–663, 2000.

[10] R. Plonsey and D.B. Heppner, "Considerations of quasistationarity in electrophysiological systems," *Bulletin of Mathematical Biophysics*, vol. 29, no. 4, pp. 657–664, 1967.

[11] J. Hara, T. Musha, and W.R. Shankle, "Approximating dipoles from human EEG activity: The effect of dipole source configuation on dipolarity using single dipole models," *IEEE Transactions on Biomedical Engineering*, vol. 46, no. 2, pp. 125–129, 1999.

[12] J.C. De Munck, B.W. Van Dijk, and H. Spekreijse, "Mathematical dipoles are adequate to describe realistic generators of human brain activity," *IEEE Transactions on Biomedical Engineering*, vol. 35, no. 11, pp. 960–966, 1988.

[13] H.L.F. Helmholtz, "Ueber einige gesetze der vertheilung elektrischer ströme in köperlichen leitern mit anwendung aud die thierisch-elektrischen versuche," *Ann Physik und Chemie*, vol. 9, pp. 211–233, 1853.

[14] C.M. Michel, M.M. Murray, G. Lantz, S. Gonzalez, L. Spinelli, and R. Grave de Peltra, "EEG source imaging," *Clinical Neurophysiology*, vol. 115, pp. 2195–2222, 2004.

[15] M.S. Hämäläinen and R.J. Ilmoniemi, "Interptreting measured magnetic fields of the brain: estimates of current distributions.," Tech. Rep., Helsinki University of Technology, 1984.

[16] C. Silva, J.C. Maltez, E. Trindade, A. Arriaga, and E. Ducia-Soares, "Evaluation of l1 and l2 minimum norm performances on EEG localizations," *Clinical Neurophysiology*, vol. 115, pp. 1657–1668, 2004.

[17] C.L. Lawson and R.J. Hanson, *Solving least squares problems*, NJ: Prentice Hall, 1974.

[18] I.F. Gorodnitsky, J.S. George, and B.D. Rao, "Neuromagnetic source imaging with FOCUSS: a recursive weighted minimum norm algorithm," *Electroencephalogr Clin Neurophysiol*, vol. 95, pp. 231–251, 1995.

[19] R. Grave de Peralta Menendez and S.L. Gonzalez Andino, "A critical analysis of tlinear inverse solutions," *IEEE Trans Biomed Eng*, vol. 45, pp. 440–448, 1998.

[20] R.D. Pasucal-Marqui, "Standardized low resoluiton brain electromagnetic tomography (sLORETA): technical details," *Methods Findings Exp Clin Pharmacol*, vol. 24D, pp. 5–12, 2002.

[21] M. Fuchs, H.A. Wischmann, and M. Wagner, "Generalized minimum norm least squares reconstruction algorithms," *ISBET newsletter*, vol. 5, pp. 8–11, 2002.

[22] M. Hämäläinen, "Discrete and distributed source estimates," *ISBET newsletter*, vol. 6, pp. 9–12, 1995.

[23] M. Fuchs, M. Wagner, T. Kohler, and H.A. Wischmann, "Linear and nonlinear current density reconstructions (review)," *J Clin Neurophysiol*, vol. 16, pp. 267–95, 1999.

[24] R. Grave de Peralta Menendez and S.L. Gonzalez, "Discussing the capabilities of laplacian minimization," *Brain Topography*, vol. 13, pp. 97–104, 2000.

[25] R. Grave de Peralta, S. Gonzalez, G. Lantz, C.M. Michel, and T. Landis, "Noninvasive localization of electromagnetic epileptic activity," *Brain Topography*, vol. 14, pp. 131–137, 2001.

[26] R. Grave de Peralta, M.M. Murray, C.M. Michel, R. Martuzzi, and S. Gonzalez Andino, "Electrical neuroimaging based on biophysical constraints," *NeuroImage*, vol. 21, pp. 527–539, 2004.

[27] G. Lantz, R. Grave de Peralta, L. Spinelli, M. Seeck, and Michel C.M., "Epileptic source localization with high density EEG: how many electrodes are needed?," *Clin Neurophysiol*, vol. 114, pp. 63–69, 2003.

[28] G. Lantz, L. Spinelli, M. Seeck, R. Grave de Peralta Menendez, C. Sottas, and C.M. Michel, "Propagation of interictal epileptiform activity can lead to erroneous source localizations: a 128 channel EEG mapping study," *J Clin Neurophysiol*, vol. 20, pp. 311–319, 2003.

[29] C.M. Michel, G. Lantz, L. Spinelli, R. Grave de Peralta, T. Landis, and M. Seeck, "128-channel EEG source imaging in epilepsy: clinical yield and localization precision," *J Clin Neurophysiol*, vol. 21, pp. 71–83, 2004.

[30] O. Steinsträter, S. Sillekens, M. Junghoefer, M. Burger, and C.H. Wolters, "Sensitivity of beamformer source analysis to deficiencies in forward modeling," *Human Brain Mapping*, vol. 31, no. 12, pp. 1907–1927, 2010.

[31] G.R. Barnes and A. Hillebrand, "Statistical flattening of MEG beamformer images," *Hum Brain Mapp*, vol. 18, pp. 1–12, 2003.

[32] M. Taniguchi, A. Kato, N. Fujita, M. Hirata, H. Tanaka, T. Kihara, H. Ninomiya, N. Hirabuki, H. Nakamura, S.E. Robinson, D. Cheyne, and T. Yoshimine, "Movement-related desynchronization of the cerebral cortex studied with spatially filtered magnetoencephalography," *Neuroimage*, vol. 12, pp. 298–306, 2000.

[33] D.P. Wipf, J.P. Owena, H.T. Attiasb, K. Sekiharac, and S.S. Nagarajana, "Robust bayesian estimation of the location, orientation, and time course of multiple correlated neural sources using MEG," *NeuroImage*, vol. 49, no. 1, pp. 641–655, 2010.

[34] D.M. Schmidt, J.S. George, and C.C. Wood, "Bayesian inference applied to the electromagnetic inverse problem," *Human Brain Mapping*, vol. 7, pp. 195–212, 1999.

[35] J.W. Phillips, R.M. Leahy, and J.C. Mosher, "MEG-based imaging of focal neuronal current sources," *IEEE Trans Med Imaging*, vol. 16, pp. 338–348, 1997.

[36] S. Baillet and L. A. Garnero, "Bayesian approach to introducing anatomo-functional priors in the EEG/MEG inverse problem," *IEEE Trans Biomed Eng*, vol. 44, pp. 374–385, 1997.

[37] K. Uutela, M. Hämäläinen, and R. Salmelin, "Global optimization in the localization of neuromagnetic sources," *IEEE Trans Biomed Eng*, vol. 45, pp. 716–723, 1998.

[38] R. Grave de Peralta and S.L. Gonzalez, "Single dipole localization: Some numerical aspects and a practical rejection criterion for the fitted parameters," *Brain Topogr*, vol. 6, pp. 277–282, 1994.

[39] M. Scherg and D. Von Cramon, "Evoked dipole source potentials of the human auditory cortex," *Electroencephalogr Clin Neurophysiol*, vol. 65, pp. 344–360, 1986.

[40] M. Scherg, T. Bast, and P. Berg, "Multiple source analysis of interictal spikes: goals, requirements, and clinical value (review)," *J Clin Neurophysiol*, vol. 16, pp. 214–224, 1999.

[41] J.C. Mosher and R.M. Leahy, "Recursive MUSIC: a framework for EEG and MEG source localization," *IEEE Trans Biomed Eng*, vol. 45, pp. 1342–1354, 1998.

[42] J.J. Foxe, M.E. McCourt, and D.C. Javitt, "Right hemisphere control of visuospatial attention: line-bisection judgments evaluated with high-density elec- trical mapping and source analysis," *Neuroimage*, vol. 19, pp. 710–726, 2003.

[43] S. Andrieux and A. Ben Abda, "Identification of planar cracks by complete overdetermined data: inversion formulae," *Inverse Problems*, vol. 12, pp. 553–564, 1996.

[44] M. Chafik, A. El Badia, and T. Ha-Duong, "On some inverse EEG problems. inverse problems," *Eng. Mech. II*, pp. 537–544, 2000.

[45] L. Baratchart, A. Ben Abda, F. Ben Hassen, and J. Leblond, "Recovery of pointwise sources or small inclusions in 2d domains and rational approximation," *Inverse Problems*, vol. 21, pp. 51–74, 2005.

[46] L. Baratchart, J. Leblond, F. Mandréa, and E.B. Saff, "How can the meromorphic approximation help to solve some 2d inverse problems for the laplacian?," *Inverse Problems*, vol. 15, pp. 79–90, 1999.

[47] L. Baratchart, J. Leblond, and J.-P. Marmorat, "Inverse sources problem in a 3d ball from best meromorphic approximation on 2d slices," *Inverse Problems*, vol. 25, pp. 41–53, 2006.

[48] P.L. Dragotti, M. Vetterli, and T. Blu, "Sampling moments and reconstructing signals of finite rate of innovation: Shannon meets Strang-Fix," *IEEE Transactions on Signal Processing*, vol. 55, no. 5, pp. 1741–1757, 2007.

[49] T. Blu, P.-L. Dragotti, M. Vetterli, P. Marziliano, and L. Coulot, "Sparse sampling of signal innovations," *IEEE Signal Processing Magazine*, vol. 25, no. 2, pp. 31–40, 2008.

[50] R. Prony, "Essai expérimental et analytique," *Ann. École Polytechnique*, vol. 1, no. 2, pp. 24, 1795.

[51] S. Andrieux, A. Ben Abda, and J. Mohamed, "On the inverse emergent plane crack problem," *Mathematical Methods in the Applied Sciences*, vol. 21, no. 10, pp. 895–906, 1998.

[52] L. Spinelli, S.G. Andino, G. Lantz, M. Seeck, and C.M. Michel, "Electromagnetic inverse solutions in anatomically constrained spherical head models," *Brain Topogr*, vol. 13, pp. 115–125, 2000.

[53] K. Fukunaga, *Introduction to statistical pattern recognition*, Academic Press, 1972.

[54] C. Tomasi and T. Kanade, "Shape and motion from image streams under orthography: a factorization method," *International Journal of Computer Vision*, vol. 9, no. 2, pp. 137–154, 1992.

[55] Z. Zhang and D.L. Jewett, "Insidious errors in dipole localization parameters at a single time-point due to model misspecification of number of shells," *Electroencephalogr Clin Neurophysiol*, vol. 88, pp. 1–11, 1993.

[56] R. Pohlmeier, H. Buchner, G. Knoll, A. Rien´acker, R. Beckmann, and J. Pesch, "The influence of skull-conductivity misspecification on inverse source localization in realistically shaped finite element head models," *Brain Topogr*, vol. 9, no. 3, pp. 157–162, 1997.

[57] M. Clerc and J. Kybic, "Cortical mapping by Laplace-Cauchy transmission using a boundary element method," *Inverse Problems*, vol. 23, pp. 2589–2601, 2007.

[58] J.A. Cadzow, "Signal enhancementa composite property mapping algorithm," *IEEE Trans. Aucoust., Speech, Signal Processing*, vol. 36, pp. 49–62, 1988.

[59] G.E. Fasshauerand and L.L. Schumaker, *Scattered Data Fitting on the Sphere, Mathematical Methods for Curves and Surfaces II*, Vanderbilt University Press, 1998.

[60] J. Kybic, T. Blu, and M. Unser, "Generalized sampling: A variational approach—Part II: Applications," *IEEE Transactions on Signal Processing*, vol. 50, no. 8, pp. 1977–1985, 2002.

[61] T. Blu and F. Luisier, "The SURE-LET approach to image denoising," *IEEE Transactions on Image Processing*, vol. 16, no. 11, pp. 2778–2786, 2007.

[62] M. Sun, "An efficient algorithm for computing multishell spherical volume conductor models in EEG dipole source localization," *IEEE Trans. Biomed. Eng.*, vol. 44, no. 12, pp. 1243–1252, 1997.

[63] V.P. Clark, C. Fan, and S.A. Hillyard, "Identification of early visual evoked potential generators by retinotopic and topographic analyses," *Human Brain Mapping*, vol. 2, no. 3, pp. 170–187, 1994.

[64] R. Spehlmann, *Spehlmann's evoked potential primer*, Butterworth-Heinemann, 2001.

[65] J. Britz, M.A. Pitts, and C.M. Michel, "Right paretal brain activity precedes perceptual alternation during binocular rivalry," *Human Brain Mapping*, vol. 19, no. 1, pp. 55–65, 2010.

[66] M.A. Pitts, A. Martínez, and S.A. Hillyard, "When and where is binocular rivalry resolved in the visual cortex?," *Journal of Vision*, vol. 10, no. 25, pp. 1–11, 2010.

[67] J. Kybic, M. Clerc, O. Faugeras, R. Keriven, and T. Papadopoulo, "Generalized head models for MEG/EEG: boundary element method beyond nested volumes," *Physics in Medicine and Biology*, vol. 51, no. 5, pp. 1333–1346, 2006.

[68] H. Hallez, B. Vanrumste, P. Van Hese, Y. D'Asseler, I. Lemahieu, and R. Van de Walle, "A finite difference method with reciprocity used to incorporate anisotropy in electroencephalogram dipole source localization," *Physics in Medicine and Biology*, vol. 50, no. 16, pp. 3787–3806, 2005.

Curriculum Vitæ

Informations personnelles

Nom / Prénom	KANDASWAMY, Djano
Nationalité	Belge
Date de naissance	07 septembre 1982
Adresse	Rue de Condémines 22 1950 Sion
Courriel	djano.kandaswamy@epfl.ch

Formation

2007-2011	**Doctorant** au Medical Image Processing Laboratory : *Localization of sparse sources using an extension of Prony's method for Poisson's equation*	EPFL - Suisse
2006	**Développeur de logiciel** à SmartGene	PSE - Suisse
2004-2006	**Master 2** *Sciences de l'ingénieur, option Informatique*	UGent - Belgique
2002-2004	**Master 1** *Master en Informatique, option Mathématique Numérique*	UGent - Belgique
2000	**Baccalauréat** Scientifique	Gent - Belgique

Enseignement

2007 jusqu'à présent — **Assistant** pour le cours *Traitement d'images*, niveau Master, du Prof. Unser. Préparation exercices. Séances d'exercices. — EPFL – Suisse

Proposition et encadrement de projets pour étudiants de master :

- *Estimation non-linéaire paramétrique de sources ponctuelles dirigé par l'équation de Helmholtz*

Recherche

Publications de journal

- D. Kandaswamy, T. Blu, D. Van De Ville, "Analytic sensing : non-iterative retrieval of point sources from boundary measurements," SIAM Journal on Scientific Computing, vol. 31 :(4) pp. 3179-3194.
- D. Kandaswamy, T. Blu, D. Van De Ville, "Analytic Sensing for Multi-Layer Spherical Models with Application to Source Imaging," *Submitted to Inverse Problems*

Publications de conférence

- D. Kandaswamy, T. Blu, D. Van De Ville, "Analytic sensing : direct recovery of point sources from planar Cauchy boundary measurements," Proceedings of the SPIE conference on Mathematical Imaging : Wavelets XII, vol. 6701 pp. 67011Y- 1-67011Y-6.
- D. Kandaswamy, T. Blu, D. Van De Ville, "Analytic sensing : a new approach to source imaging and its application to EEG," SIAM Conference on Imaging Science pp. 68.
- D. Kandaswamy, T. Blu, L. Spinelli, C. Michel, D. Van De Ville, "EEG source localization by multi-planar analytic sensing", Proceedings of the Fifth IEEE International Symposium on Biomedical Imaging : From Nano to Macro ISBI'08
- D. Kandaswamy, T. Blu, L. Spinelli, C. Michel, D. Van De Ville, "Local Multilayer Analytic Sensing for EEG Source Localization : Performance Bounds and Experimental Results," Proceedings of the Eight IEEE International Symposium on Biomedical Imaging : From Nano to Macro (ISBI'11)